

University of Alberta

**Sodium ions in Mercury's exosphere:
particle tracing**

by

Jan Paral



A thesis submitted to the Faculty of Graduate Studies and Research in partial
fulfillment of the requirements for the degree of Master of Science

Department of Physics

Edmonton, Alberta
Fall 2007



Library and
Archives Canada

Bibliothèque et
Archives Canada

Published Heritage
Branch

Direction du
Patrimoine de l'édition

395 Wellington Street
Ottawa ON K1A 0N4
Canada

395, rue Wellington
Ottawa ON K1A 0N4
Canada

Your file *Votre référence*
ISBN: 978-0-494-33322-8
Our file *Notre référence*
ISBN: 978-0-494-33322-8

NOTICE:

The author has granted a non-exclusive license allowing Library and Archives Canada to reproduce, publish, archive, preserve, conserve, communicate to the public by telecommunication or on the Internet, loan, distribute and sell theses worldwide, for commercial or non-commercial purposes, in microform, paper, electronic and/or any other formats.

The author retains copyright ownership and moral rights in this thesis. Neither the thesis nor substantial extracts from it may be printed or otherwise reproduced without the author's permission.

AVIS:

L'auteur a accordé une licence non exclusive permettant à la Bibliothèque et Archives Canada de reproduire, publier, archiver, sauvegarder, conserver, transmettre au public par télécommunication ou par l'Internet, prêter, distribuer et vendre des thèses partout dans le monde, à des fins commerciales ou autres, sur support microforme, papier, électronique et/ou autres formats.

L'auteur conserve la propriété du droit d'auteur et des droits moraux qui protègent cette thèse. Ni la thèse ni des extraits substantiels de celle-ci ne doivent être imprimés ou autrement reproduits sans son autorisation.

In compliance with the Canadian Privacy Act some supporting forms may have been removed from this thesis.

Conformément à la loi canadienne sur la protection de la vie privée, quelques formulaires secondaires ont été enlevés de cette thèse.

While these forms may be included in the document page count, their removal does not represent any loss of content from the thesis.

Bien que ces formulaires aient inclus dans la pagination, il n'y aura aucun contenu manquant.


Canada

To
Earth

Abstract

So far, Mercury is not a well understood planet. The initial interest started with the visit of Mariner 10 in 1974 and 1975 to the vicinity of the planet during three flybys. Two of those approaches revealed a most interesting finding that Mercury possesses its own magnetic field of dipolar character. Recently, two new missions were scheduled to uncover more mysteries of this iron neighbour of the Sun. First, NASA MESSENGER was launched on March 2004 and then the cornerstone mission BepiColombo in a joint collaboration between ESA and JAXA. In the past, several ground-based observations of Mercury were made although measurements are difficult due to its proximity to the Sun. One of these observations [*Potter and Morgan, 1985*] revealed a sodium exosphere generated from the surface of the planet. Among others, one of the goals of missions to Mercury is to study the exosphere of heavy ions. This thesis intends to contribute to the interpretation of data received from MESSENGER and BepiColombo and to suggest possible sources and processes of sodium ions in the exosphere.

Acknowledgements

I acknowledge all people who were helping me and supporting me to finish this thesis. Especially my supervisor Prof. Robert Rankin who supported me all the time even when my results were not convincing, my external adviser Dr. Pavel Travnicek who answered so many questions about hybrid modeling and physics in general - without him I would never go study abroad, and Dr. Konstantin Kabin who provided much appreciated advice on modeling Mercury. They were always there to answer my questions and I would not be able to finish this work without them. I thank them for their patience and discussions not only about my research but about ethical issues as well. Also a big thanks goes to my parents and my friends, especially to Eun Ah Lee, Gyusik Kim, Chokri Dridi and others.

Table of Contents

1	Introduction	1
2	In situ observations	4
2.1	Mariner 10	4
2.1.1	Instrumentation	6
2.1.2	Flybys	7
2.2	MESSENGER	8
2.2.1	Scientific Payload	10
2.3	BepiColombo	12
2.3.1	Scientific Payload	15
3	Remote measurements	18
3.1	Observations	18
3.1.1	Sodium and Potassium	20
4	Exosphere	24
4.1	Introduction	24
4.2	Releasing processes	25
4.2.1	Surface temperature	27
4.2.2	Photon stimulated desorption (PSD)	27
4.2.3	Solar wind sputtering (SWS)	28
4.2.4	Micro-meteoroid vaporization (MMV)	29
4.2.5	Thermal desorption (THD)	30
4.3	Ionization	31
5	Numerical simulations	33
5.1	Hybrid simulations	33
5.1.1	Numerical Scheme	34
5.1.2	Model Scaling	36
5.1.3	Initialization	38
5.1.4	Electric and Magnetic fields	39
5.2	Particle tracing	39
5.2.1	Algorithm	40
5.2.2	Particle loading	42
5.2.3	Output quantities	43

TABLE OF CONTENTS

6 Results	45
6.1 Electric and magnetic drifts	45
6.2 Particle statistics	50
6.3 Single Particle	51
6.4 Surface of the Planet	53
6.5 Bulk velocity	59
6.6 Temperature anisotropy	66
6.7 Number density	69
6.8 Mean energy	69
6.9 Virtual flybys of MESSENGER	74
7 Conclusions	80
Bibliography	82

List of Tables

2.1	Instruments on board of the Mariner 10 measuring field and particle properties. Original table adopted from <i>Wurz and Blomberg</i> [2001].	7
2.2	Approximate timeline for MESSENGER mission.	9
2.3	MESSENGER payload summary.	11
2.4	Spacecraft summary adopted from official BepiColombo website.	14
2.5	BepiColombo payload summary.	14
3.1	Atmospheric abundances for Mercury's mean orbit; quiet Sun	19
3.2	Sodium and Potassium spectral line	21
4.1	Physical Properties of Mercury and the Moon (for comparison)	25
4.2	Atmospheric loss rates for quiet Sun (a,c) and active Sun (b,d) experimentally (a,b) and theoretically (c,d) determined.	32
5.1	Solar wind parameter of the study cases	37
5.2	Conversion of simulation units to SI units for two study cases	38
6.1	Particle statistics. N_{bnd} , N_{pl} and N_{emit} are number of particles which left the simulation box through the boundary, hit back the surface and total number emitted into the system respectively.	51

List of Figures

1.1	Summary of interacting processes. Schematics adopted from [Mitillo <i>et al.</i> , 2005, Figure 1].	2
2.1	Schematic picture of Mariner 10 with labels of its parts.	5
2.2	Schematics adopted from <i>Ness et al.</i> [1975b] showing two flybys of Mariner 10.	6
2.3	Schematic picture of MESSENGER with labels of its parts (courtesy: NASA).	8
2.4	Illustration four parts of BepiColombo. Top to bottom: Mercury Magnetospheric Orbiter (MMO), Sunshield, Mercury Planetary Orbiter (MPO), Mercury Transfer Module. Courtesy ESA. . . .	13
3.1	High latitude enhancements of Na measured by <i>Potter and Morgan</i> [1997b] on July, 1994 for three consequent days 20 - 22 July, indicating rapid changes of distribution in time, in this case on scales of one day. The color bar represents rayleighs intensity. . .	22
3.2	Distribution of potassium measured on December 7, 1990 by <i>Potter and Morgan</i> [1997a, Figure 2] reflected from the surface (left) and Mercury's corona scattered at 7664 Å. The color bar represents rayleighs intensity.	23
4.1	Cartoon representing sources and sinks of atoms in the environment of the Mercury. Adopted from <i>Morgan and Killen</i> [1997, Figure 1].	26
5.1	Example of the proton density output from the 3D hybrid simulation visualized by volume rendering technique. The boundary represents the bow shock of the planet for the fast solar wind ($v_{sw} = 5v_A$).	35
5.2	The radius of the planet Mercury in hybrid units as a function of solar wind density.	37
5.3	Electric field in (from left to right) equatorial, noon-midnight, dawn-dusk plane for slow (upper) and fast (lower) solar wind conditions. Color scale represents magnitude in the units of SW electric field E_{sw} and arrows represents projection of the field in the plane of cut.	40

LIST OF FIGURES

5.4	Magnetic field in (from left to right) equatorial, noon-midnight, dawn-dusk plane for slow (upper) and fast (lower) solar wind conditions. Color scale represents magnitude in the units of SW magnetic field B_{sw} and arrows represents projection of the field in the plane of cut.	41
5.5	Macro-particle flux distribution of sodium neutral atoms from the surface of the planet. On x-axis is longitude and y-axis represents latitude with subsolar point in the center. Three process are presented here from top to bottom: PSD, MMV and SWS.	44
6.1	$\mathbf{E} \times \mathbf{B}$ drift in the vicinity of the planet for slow (top) and fast (bottom) solar wind conditions.	46
6.2	∇B drift in vicinity of the planet. Color represents magnitude with maximum at the bow shock of the planet and arrows represent a direction in given the plane of cut. Top and bottom panel represent slow respective fast solar wind study case. Note, that units are in v_{Asw}/v_{\perp}^2	48
6.3	Curvature drift in vicinity of the planet. Color represents magnitude with maximum at the bow shock of the planet and arrows represent a direction in given the plane of cut. Top and bottom panel represent slow respective fast solar wind study case. Note, that units are in v_{Asw}/v_{\parallel}^2	49
6.4	Projection of a single test particle trajectories released from the latitude of 40°S and for three longitudes: -90 (solid line), -30 (dotted line) and 50° (dashed line), measured from the subsolar point. The initial velocity of test particles is $ \mathbf{u} = 0.01$. In the background is magnitude of magnetic field in units of solar wind magnetic field B_{sw}	52
6.5	A planetary deposit map, under the slow solar wind conditions, of the super-particle flux (color scale) through the surface for three major releasing processes: PSD, SWS and MMV (from top to bottom). On x-axis and y-axis is longitude respectively latitude in Miller cylindrical projection of the surface The subsolar point is in the middle of projection.	54
6.6	Mean energy flux (color scale) of sodium ions through the surface of the planet under the slow solar wind conditions for three major releasing processes: PSD, SWS and MMV (from top to bottom). On x-axis and y-axis is longitude respectively latitude in Miller cylindrical projection of the surface The subsolar point is in the middle of projection.	55
6.7	A planetary deposit map, under the fast solar wind conditions, of the super-particle flux (color scale) through the surface for three major releasing processes: PSD, SWS and MMV (from top to bottom). On x-axis and y-axis is longitude respectively latitude in Miller cylindrical projection of the surface The subsolar point is in the middle of projection.	56

LIST OF FIGURES

6.8 Mean energy flux (color scale) of sodium ions through the surface of the planet under the fast solar wind conditions for three major releasing processes: PSD, SWS and MMV (from top to bottom). On x-axis and y-axis is longitude respectively latitude in Miller cylindrical projection of the surface The subsolar point is in the middle of projection. 57

6.9 Bulk velocity in noon-midnight plane in units of Alfvén speed of solar wind v_{Asw} for slow solar wind $v_{sw} = 3 v_{Asw}$. Three major releasing processes are presented in each column: photon stimulated desorption (PSD), solar wind sputtering (SWS) and micro-meteorite vaporization (MMV). The velocity is transformed into spherical coordinate system: radial direction (top row); longitudinal direction (middle row); and azimuthal direction (bottom row). The black line represents an assessment of magnetopause. 60

6.10 Bulk velocity in noon-midnight plane in units of Alfvén speed of solar wind v_{Asw} for fast solar wind $v_{sw} = 5 v_{Asw}$. Three major releasing processes are presented in each column: photon stimulated desorption (PSD), solar wind sputtering (SWS) and micro-meteorite vaporization (MMV). The velocity is transformed into spherical coordinate system: radial direction (top row); longitudinal direction (middle row); and azimuthal direction (bottom row). The black line represents an assessment of magnetopause. 61

6.11 Bulk velocity, in plane forming an angle 60° with noon-midnight plane, in units of Alfvén speed of solar wind v_{Asw} for slow solar wind $v_{sw} = 3 v_{Asw}$. Three major releasing processes are presented in each column: photon stimulated desorption (PSD), solar wind sputtering (SWS) and micro-meteorite vaporization (MMV). The velocity is transformed into spherical coordinate system: radial direction (top row); longitudinal direction (middle row); and azimuthal direction (bottom row). The black line represents an assessment of magnetopause. 62

6.12 Bulk velocity, in plane forming an angle 60° with noon-midnight plane, in units of Alfvén speed of solar wind v_{Asw} for fast solar wind $v_{sw} = 5 v_{Asw}$. Three major releasing processes are presented in each column: photon stimulated desorption (PSD), solar wind sputtering (SWS) and micro-meteorite vaporization (MMV). The velocity is transformed into spherical coordinate system: radial direction (top row); longitudinal direction (middle row); and azimuthal direction (bottom row). The black line represents an assessment of magnetopause. 63

LIST OF FIGURES

6.13	Bulk velocity in dawn-dusk plane in units of Alfvén speed of solar wind v_{Asw} for slow solar wind $v_{sw} = 3 v_{Asw}$. Three major releasing processes are presented in each column: photon stimulated desorption (PSD), solar wind sputtering (SWS) and micrometeorite vaporization (MMV). The velocity is transformed into spherical coordinate system: radial direction (top row); longitudinal direction (middle row); and azimuthal direction (bottom row). The black line represents an assessment of magnetopause.	64
6.14	Bulk velocity in dawn-dusk plane in units of Alfvén speed of solar wind v_{Asw} for slow solar wind $v_{sw} = 5 v_{Asw}$. Three major releasing processes are presented in each column: photon stimulated desorption (PSD), solar wind sputtering (SWS) and micrometeorite vaporization (MMV). The velocity is transformed into spherical coordinate system: radial direction (top row); longitudinal direction (middle row); and azimuthal direction (bottom row). The black line represents an assessment of magnetopause.	65
6.15	Temperature anisotropy T_{\perp}/T_{\parallel} in slow solar wind case from three major releasing processes: PSD, SWS, MMV (from top to bottom) in three different cuts through the center of the planet: X-Y, X-Z and Y-Z (from left to right).	67
6.16	Temperature anisotropy T_{\perp}/T_{\parallel} in fast solar wind case from three major releasing processes: PSD, SWS, MMV (from top to bottom) in three different cuts through the center of the planet: X-Y, X-Z and Y-Z (from left to right).	68
6.17	Super-particle number density in slow solar wind configuration of EM field of three major releasing processes: PSD, SWS, MMV (from top to bottom) in three different cuts through the center of the planet: X-Y, X-Z and Y-Z (from left to right). The three lines represents flybys of MESSENGER before parking on the orbit as of April 30, 2007.	70
6.18	Super-particle number density in fast solar wind configuration of EM field of three major releasing processes: PSD, SWS, MMV (from top to bottom) in three different cuts through the center of the planet: X-Y, X-Z and Y-Z (from left to right). The three lines represents flybys of MESSENGER before parking on the orbit as of April 30, 2007.	71
6.19	Mean energy of three major releasing processes: PSD, SWS, MMV (from top to bottom) in three different cuts through the center of the planet: X-Y, X-Z and Y-Z (from left to right). The three lines represents flybys of MESSENGER before parking on the orbit as of April 30, 2007.	72
6.20	Mean energy of three major releasing processes: PSD, SWS, MMV (from top to bottom) in three different cuts through the center of the planet: X-Y, X-Z and Y-Z (from left to right). The three lines represents flybys of MESSENGER before parking on the orbit as of April 30, 2007.	73

LIST OF FIGURES

6.21 Virtual flybys of MESSENGER scheduled for 2008/01/14 (solid line) 2008/10/06 (dotted line) and 2009/09/29 (dashed line) on the background of solar wind proton number density for slow (top) and fast (bottom) case of solar wind 75

6.22 Macro-particle number density during three virtual flybys of MESSENGER in the vicinity of the planet for slow (top 3 panels) and fast (bottom 3 panels) solar wind. Solid line, dotted line and dashed line represents PSD, SWS and MMV processes respectively. Time $t = 0$ represents the closest approach. 76

6.23 Sodium mean energy during three virtual flybys of MESSENGER in the vicinity of the planet for slow (top 3 panels) and fast (bottom 3 panels) solar wind. Solid line, dotted line and dashed line represents PSD, SWS and MMV processes respectively. Time $t = 0$ represents the closest approach. 77

Chapter 1

Introduction

Mercury is the first planet in our solar system, with a mean distance of 0.387AU. The trajectory of the orbit is highly eccentric. The eccentricity of Mercury is $e = 0.205$ and its orbital period is 87.969 of terrestrial days. One day in Mercury is 58.785 of the Earth's days. The planet's spin axis is almost perpendicular to the plane of orbit. Because of its proximity to the Sun, the temperature ranges between 700 K at perihelion subsolar point and 90 K at midnight of aphelion. Mercury's radius is approximately $R_M = 2440$ km which is 2.6 times smaller than that of the Earth's and its density is 5.3 g/cm^3 which is comparable to the Earth's density. This is probably due to Mercury's heavy iron-rich core and thin layer of its upper mantle.

The only *in situ* measurements were made by Mariner 10 in 1974-75 during three flybys. The data from this mission showed that Mercury possesses no proper atmosphere and only a thin exosphere [Broadfoot *et al.*, 1976b] which is coupled with the planet. Only six planets have their own magnetic field: Mercury, Earth, Jupiter, Saturn, Uranus, and Neptune. We do not know whether Pluto has a magnetic field but Mars has the weakest one. A major finding was the discovery of Mercury's internal magnetic field [Ness *et al.*, 1974a] with an estimated magnetic dipole of 200-400 nT R_M^3 (Earth's magnetic dipole is 30000 nT R_E^3). A more precise estimate will provide measurements from MESSENGER's mission compared with numerical simulations [Kabin *et al.*, 2007]. The source of the magnetic field is most likely an inner dynamo [Southwood, 1997]. The dipole axis is almost aligned with the spin axis and points approximately 10° from the southern pole. Over the last several years ground-based observations replaced *in situ* measurements. Killen and Ip [1999] assessed Mercury's column density to be $< 10^{12} \text{ cm}^{-2}$ of observed atoms. Because of this relatively low density, we can expect the exosphere to be non-collisional. From the UVS instruments of Mariner 10 and ground-based observations, several species were

confirmed to be present on Mercury, namely H, He, O, Na, K as discussed in *Broadfoot et al.* [1976b]; *Potter and Morgan* [1985, 1986]; *Bida et al.* [2000]. Compared to the situation on Earth, the Hermean magnetosphere possesses a relatively weak magnetic field. Despite this fact, experiments measuring energy on board of Mariner 10 recorded [*Simpson et al.*, 1974b] ions with energies of up to 55 keV and electrons with energies of up to 300 keV. *Eraker and Simpson* [1986] and *Lundin et al.* [1997] discussed various acceleration processes involved in exciting particles to such energy levels.

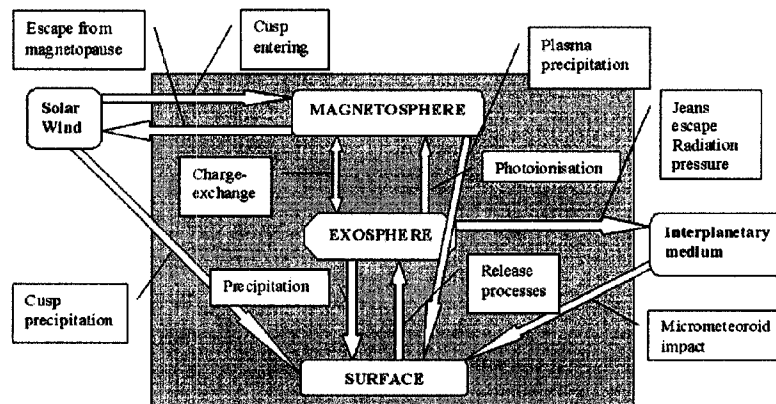


Figure 1.1: Summary of interacting processes. Schematics adopted from [*Milillo et al.*, 2005, Figure 1].

In Figure 1.1, adopted from *Milillo et al.* [2005], you can see the details of the processes coupling the magnetosphere, exosphere, and surface together. Two main sources of particles are filling this coupled system. First, the solar wind is entering through the cusp regions where part of the particles precipitate on the surface. Second, the interplanetary medium in the form of dust and micrometeorite impact on the surface. When particles become part of Mercury's environment, they start to circulate in the system (in case of solar wind) or they can scatter on the surface, which causes a sputtering. Sputtered particles can escape from the surface by any of the releasing processes into the exosphere with energy of few eV from where they can precipitate back to the surface or be ionized by photoionization or charge exchange, and become part of the magnetosphere. From there, particles can precipitate back on the planet or escape via Jeans' escape¹ or by the radiation pressure.

¹The loss of atoms in the high energy tail of the Maxwell-Boltzmann distribution function

The magnetosphere of Mercury is closely connected with the conditions of the solar wind because of three factors: i) Mercury is the closest planet to the Sun and thus solar wind conditions are extreme, ii) the strength of the magnetic dipole allows solar wind pressure to distort the magnetosphere and probably even allow particles to directly access the dayside of the planet as suggested by *Kabin et al.* [1999], and iii) the lack of trapped particles.

The Hermean exosphere is constantly filled by neutral atoms and ions by sputtering mechanisms from the surface (in the case of sodium and potassium) but other sources are also possible. For example, in a recent publication, *Koehn and Sprague* [2007] suggests an important source of oxygen and calcium from the solar wind. The main sputtering mechanisms, by importance, are: photon stimulated desorption, solar wind sputtering, micro-meteoroid vaporization, thermal desorption, and chemical sputtering. We consider only the first three sputtering mechanisms because others are not energetic enough to overcome gravitation and the solar wind radiation pressure forces.

Our goal is then to trace particles in a snapshot of electric and magnetic fields obtained from hybrid simulation performed by [*Trávníček et al.*, 2007]. By using a particle tracing technique we can achieve higher spatial resolution as well as longer time scales. Also, heavy ion number density is small enough to justify the use of the particle tracing technique. Other approaches are also possible, for example using magnetohydrodynamics (MHD) equations or developing an empirical model to obtain an evolved magnetosphere. However, we expect that this would neglect important aspects of physics we would like to take into account.

from the atmosphere. Jeans' escape is important for light atoms at higher altitudes. See *Hunten* [1973] for more information.

Chapter 2

In situ observations

Up to now only one mission visited Mercury. Mariner 10 made 3 flybys in the vicinity of the planet and discovered the presence of an intrinsic magnetic field. Because of many questions, new missions are being planned to visit Mercury. The first one is MESSENGER spacecraft, operated from Johns Hopkins University, Applied Physics Laboratory in Laurel, supposedly to start orbiting Mercury in May, 2011 and BepiColombo a cornerstone mission of ESA/JAXA consisting of two spacecrafts, Mercury Planetary Orbiter and Mercury Magnetospheric Orbiter. In this chapter we summarize the payload and objectives of each mission.

2.1 Mariner 10

Mariner 10 was a Mercury/Venus mission launched on 3 November 1973 at 05:45:00 UTC from Cape Canaveral, United States. That was already the seventh successful mission of the Mariner series. But it was the first mission visiting two planets (Venus and Mercury) and using the gravitational pull of one planet (Venus) to reach another (Mercury). The spacecraft was equipped with camera, magnetometer and particle detectors. The scientific objectives of the mission were to study environment, atmosphere, magnetosphere and body characteristics of the planets Mercury and Venus.

Mercury has been visited in 1974 and 1975 by the Mariner 10 spacecraft (Fig. 2.2), during which time the internal magnetic field of the planet was discovered [Ness *et al.*, 1974b] and later confirmed by Ness *et al.* [1975b]. From the measurements, estimations for the various parameters of the internal field

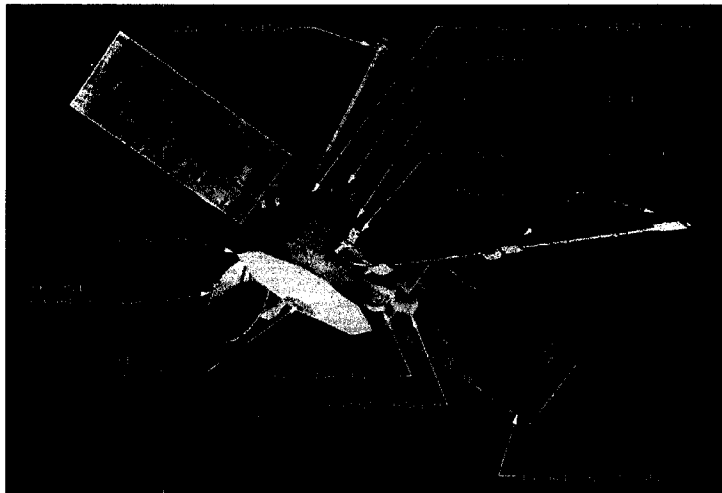


Figure 2.1: Schematic picture of Mariner 10 with labels of its parts.

of Mercury, based on the very limited measurements of Mariner 10, vary somewhat [e.g. *Connerney and Ness*, 1988], but the dipole component of the field is generally believed to be about $350 \text{ nT } R_M^3$ [*Ness et al.*, 1975a]. Measurements of thermal plasma, electron [*Ogilvie et al.*, 1977] and energetic particles [*Simpson et al.*, 1974b] were also taken by Mariner 10, but unfortunately interpretation of these data is far from unambiguous. A review by *Slavin* [2004] describes the current understanding of the Hermean magnetosphere. The only *in situ* measurements of the neutral exosphere of Mercury came from Mariner 10 spacecraft which used UV observations of airglow to identify neutral helium and hydrogen with concentrations of approximately 600 cm^{-3} and 8 cm^{-3} , respectively [*Broadfoot et al.*, 1976a]. Despite the small size and relatively weak magnetic field of the Hermean magnetosphere ions with energies of up to 550 keV and electrons with energies of up to 300 keV were detected by the energetic particle experiment on board Mariner 10 [*Simpson et al.*, 1974b]. The exact interpretation of these data is, however, somewhat ambiguous, as discussed, for example by *Armstrong et al.* [1975]; *Criston et al.* [1979]; *McKenna-Lawlor* [1997]. Possible particle acceleration mechanisms in the Hermean magnetosphere are discussed by *Eraker and Simpson* [1986] and *Lundin et al.* [1997].

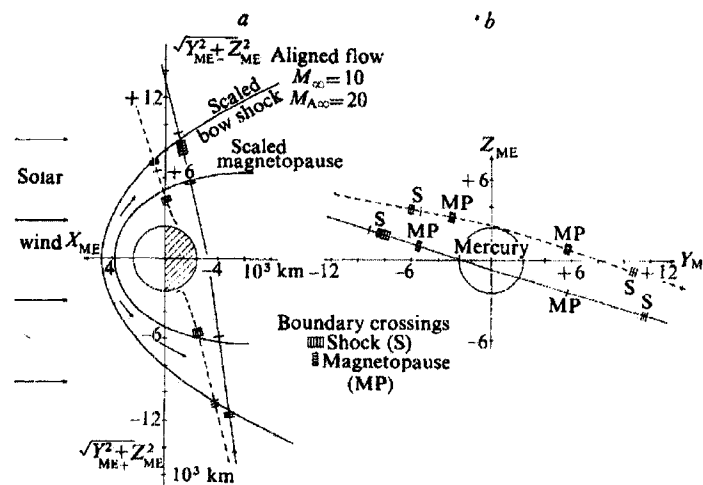


Figure 2.2: Schematics adopted from *Ness et al.* [1975b] showing two flybys of Mariner 10.

2.1.1 Instrumentation

Mariner 10 was a three-axis stabilized spacecraft loaded with instruments to try to answer questions about intrinsic magnetic field and particle populations at the environment of Mercury.

- two tri-axial fluxgate magnetometers
- a plasma science instruments
- an energetic particle detector

The overall summary of the on board instruments is presented in the Tab. 2.1.1 adopted from *Wurz and Blomberg* [2001].

Plasma science instrument

Two particle detectors were mounted on Mariner 10. First, a very sensitive sunward ion and electron sensor which unfortunately did not work properly. We do not know what happened because the sensor did not count particles above the X-ray background so we do not have any useful data. Second, antisunward electron observer which was not as sensitive as the first one. This hemispherical electrostatic analyzer was detecting particles from 13 to 688eV. The detector had 15 logarithmically spaced regions/channels with $\Delta E/E = 0.066$ width. It

Instrument	Range	Comments
Fluxgate mg. ^a	± 16 nT, ± 128 nT	Up to ± 3188 nT bias field
El. analyser ^b	13.4 – 688 eV	13 log. spaced channels
Energetic pcle. det. ^c	e^{-1} : 170 keV – 30 MeV p, α : 0.62 – 68 MeV	Range > 35 keV for e^{-1} in case of pulse pile-up
Energetic pcle. det. ^d	e^{-1} : 170 keV – 30 MeV p: 0.53 – 8.9 MeV	Range > 35 keV for e^{-1} in case of pulse pile-up

^a *Ness et al.* [1974a, b]

^b *Ogilvie et al.* [1977]

^c *Simpson et al.* [1974a]

^d *Christon et al.* [1979]

Table 2.1: Instruments on board of the Mariner 10 measuring field and particle properties. Original table adopted from *Wurz and Blomberg* [2001].

took 0.4 second to finish a measurement in one channel and 15 seconds to scan entire spectrum. Both detectors were mounted on a motor driven platform which was able to rotate 1 or 4° /sec.

Energetic particle detector

Those detectors consist of two parts, a main telescope (MT) and low energy telescope (LET). The experiments provided basic energy measurements like energy loss, total energy and range of particles that entered the telescope.

2.1.2 Flybys

Mariner 10 was launched on November 2, 1973 and encountered Mercury on: March 29, 1974 (MI), September 21, 1974 (MII) and March 16, 1975 (MIII). The first flyby (MI) on March 29, 1974 approached Mercury with the closest distance 723 km to the planet's surface on the night-side. During that time a maximal magnetic field $B_{max} = 98nT$ was measured. The low latitude nightside flyby crossed a substorm-like injection region leading to magnetic field dipolarization effects (A-D events) reported by *Luhmann et al.* [1998]. By comparing with terrestrial observations these events are supposed to be part of the substorm process. No later confirmations were published and only new measurements can provide necessary additional information. One such event was detected between 20:48 and 20:49 UT.

Because no one expected a magnetic field at Mercury, MII on September 21,

1974 was scheduled far on the dayside with the closest approach 5×10^4 km to the planet. No interaction with the solar wind and intrinsic field was detected.

On March 16, 1975, MIII took place again on the nightside but much closer to the surface with the closest approach 327 km to planet. During this passing in high latitude of 68°N the maximal magnetic field $B_{max} = 400nT$ was recorded and helped to estimate the magnetic dipole moment. This time no energetic particle events were detected.

2.2 MESSENGER

MESSENGER (short for MErcury Surface, Space ENvironment, GEochemistry, and Ranging) is a NASA project [Gold *et al.*, 2001; Andrews *et al.*, 2007] which visits Mercury after 30 years from the last *in situ* measurements by Mariner 10. The spacecraft was launched on August 3, 2004 and is scheduled to enter the orbit of Mercury in March 2011 before it circles the Sun 15 times and travels 7.9 billion kilometers. Before parking at the orbit, MESSENGER will undergo two flybys around Venus and three flybys around Mercury. The mission is managed by Mission Operation Center at the Johns Hopkins University Applied Physics Laboratory in Laurel, Md. Table 2.2 summarize important milestones of the MESSENGER mission.

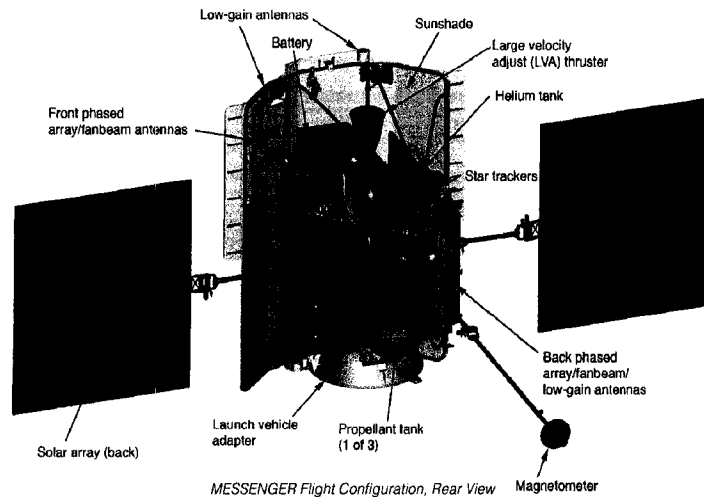


Figure 2.3: Schematic picture of MESSENGER with labels of its parts (courtesy: NASA).

Data	Event
August 3, 2004	Launch from Cape Canaveral
August 2, 2005	Earth flyby
October 24, 2006	Venus flyby 1
June 5, 2007	Venus flyby 2
January 14, 2008	Mercury flyby 1
October 6, 2008	Mercury flyby 2
September 29, 2009	Mercury flyby 3
March 18, 2011	Orbit of Mercury begins
March 18, 2012	Mercury orbit/data collection ends
March 2013	Final data analysis/archiving complete

Table 2.2: Approximate timeline for MESSENGER mission.

The spacecraft is powered by two solar panels, 1.5 m by 1.65 m, which are designed to provide 385-485 W for the payload during the cruise phase and 640 W during the orbit phase but theoretically can produce more than 2 kW on the Mercury's orbit. The propulsion system consists of a 660 N bipropellant thruster for large maneuvers and 16 hydrazine-propellant thrusters for adjustments in a trajectory. The communication system consists of several antennas. Those include two high gain phased array antennas; two medium gain fanbeam antennas and four low gain antennas. The downlink rate ranges from 9.9 b/s to 104 kb/s for data transmission and 7.8 to 500 b/s for operating commands. The rates vary according to spacecraft distance and size of the antennas on the ground. Once inserted on the orbit on March 18, 2011 MESSENGER will have a highly elliptical orbit around Mercury with the closest point 200 km above the surface and 15195 km at the farthest part of the trajectory. The plane of the orbit is inclined 80° to Mercury's equator with the low point in the orbit coming at 60° north latitude. The orbit period will be 12 h approximately.

The objectives of MESSENGER are to find the answer to the questions raised by the Mariner 10 mission. An iron core of Mercury plays a key role in the total density of the planet which is comparable with density of Earth. The core inside of the rocky crust takes approximately 60% of total mass which is twice as much as at Earth. The proximity of the Sun can be a factor but we are not sure for now. Those are six areas which should be addressed by the MESSENGER mission:

- the density of Mercury

- the geologic history
- the structure of the core
- the nature of the magnetic field
- the unusual materials at the poles
- the important volatiles

2.2.1 Scientific Payload

All instruments are designed to achieve critical conditions in the vicinity of the Sun and to minimize weight due to the budget restrictions. MESSENGER carries seven instruments and a radio equipment including radio experiments and imaging cameras to finish mapping of the surface. All instruments should help to understand geologic history, the origin of the magnetosphere as well as exosphere and explore materials near the pole regions. All instruments are summarized in Table 2.3. Together with indirect measurements, which we can perform from radio science observations, we should be able to answer questions which arise from Mariner 10 mission 30 years ago.

Mercury Dual Imaging System

MDIS are charge-coupled devices (CCDs) with narrow and wide angle objectives. Those cameras will map the Mercury's surface and spectral variations in monochrome, color and stereo. The imager are mounted on a pivot so can be used for tracking navigation points like stars or other optical navigation guides during its journey. The wide-angle camera has a 10.5 degree field of view and can distinguish wavelength range 400 to 1100 nanometers using 12 different filters. Its results will be used to investigate the diversity of rock types found on the surface. The narrow-angle camera has black and white CCD with high resolution through its 1.5 degree field of view. The images will be used to analyze small object and features up to 19 meters across.

Gamma-Ray and Neutron Spectrometer

GRNS is a set of two spectrometers (gamma-ray and neutron) to retrieve the informations about elements in the upper crust of Mercury. The Gamma-Ray spectrometer is planned to search for geologically important elements such as

Instrument	Mass [<i>kg</i>]	Power [<i>W</i>]	Name
MDIS	7.9	10	Mercury Dual Imaging System
GRNS	13.1	23.6	Gamma-Ray and Neutron Spectrometer
XRS	3.4	11.4	X-Ray Spectrometer
MAG	4.4	4.2	Magnetometer
MLA	7.4	38.6	Mercury Laser Altimeter
MASCS	3.1	8.2	Mercury Atm. and Surf. Composition Spect.
EPPS	3.1	7.8	Energetic Particle and Plasma Spectrometer

Table 2.3: MESSENGER payload summary.

hydrogen, magnesium, silicon, oxygen, iron, titanium, sodium and calcium with possibility to detect naturally radioactive elements such as potassium, thorium and uranium. The detector is made of high-purity germanium semiconductor crystal on a thin Kevlar string and must operate at cryogenic temperatures (-183° Celsius) ensured by small but powerful refrigerator. The Neutron Spectrometer will measure the abundance of various atoms by comparing thermal and epi-thermal populations of neutrons.

X-Ray Spectrometer

XRS detects emissions from elements in the 1-10 keV, namely magnesium, aluminum, silicon, sulfur, calcium, titanium and iron by measuring X-ray emissions coming from Mercury's surface as a reflection from solar X-ray radiation. XRS has a 12° field of view.

Magnetometer

MAG is a three axis, ring core fluxgate detector aiming to reveal true nature and strength of internal magnetic field measured by Mariner 10. The sensor is attached on a 3.6 meter boom to prevent own magnetic field of the spacecraft to interfere. The instrument will operate at 20 Hz at magnetosphere boundaries and 1 Hz otherwise.

Mercury Laser Altimeter

MLA is a infrared laser transmitter (operating at a wavelength of 1064 nm) and receiver which will map the features of the surface by measuring round trip

time of the beam. The results together with Radio Science Doppler ranging will be used to map the planet's gravitational field. MLA can measure with up to 30 cm precision from 1000 km. The instrument consist of four saphire lenses, a photon counting detector and electronics for the time measurements and signal processing.

Mercury Atmospheric and Surface Composition Spectrometer

MASCS will measure the abundance of atmospheric gases in Mercury's exosphere and detect minerals in surface materials.

Energetic Particle and Plasma Spectrometer

EPPS [Koehn *et al.*, 2002] consists of two instruments: Energetic Particle Spectrometer (EPS) and a Fast Imaging Plasma Spectrometer (FIPS). Both will measure energy and species of charged particles. EPS has 160 by 12° field of view to measure the energy spectra, atomic composition and pitch angle of particles accelerated in magnetosphere. FIPS, on the other hand, will measure low energy particles with surface origin forming ionized by solar wind and forming very thin exosphere.

2.3 BepiColombo

BepiColombo [Anselmi and Scoon, 2001] is a “corner stone” mission of European Space Agency (ESA) and Japan Aerospace Exploration Agency (JAXA) named after Italian mathematician and engineer Giuseppe (Bepi) Colombo (1920-1984) from the University of Padua, Italy. The BepiColombo mission is planned to launch in August 2013 and travel 6 years to Mercury. In August 2019 it should arrive on the orbit and start collecting data for one year with possible extension of another year up till September 2021.

The mission will consists of two satellites: Mercury Planetary Orbiter (MPO) and Mercury Magnetospheric Orbiter (MMO) which will travel to Mercury inside the sunshield of BepiColombo (see Fig. 2.4) and will be inserted into the low orbit during parking phase of the mission. Original proposal expected Mercury Surface Element (MSE) to be a part of the mission but was canceled later due to the budget constrains. The details of MPO and MMO are provided in Tab 2.4.

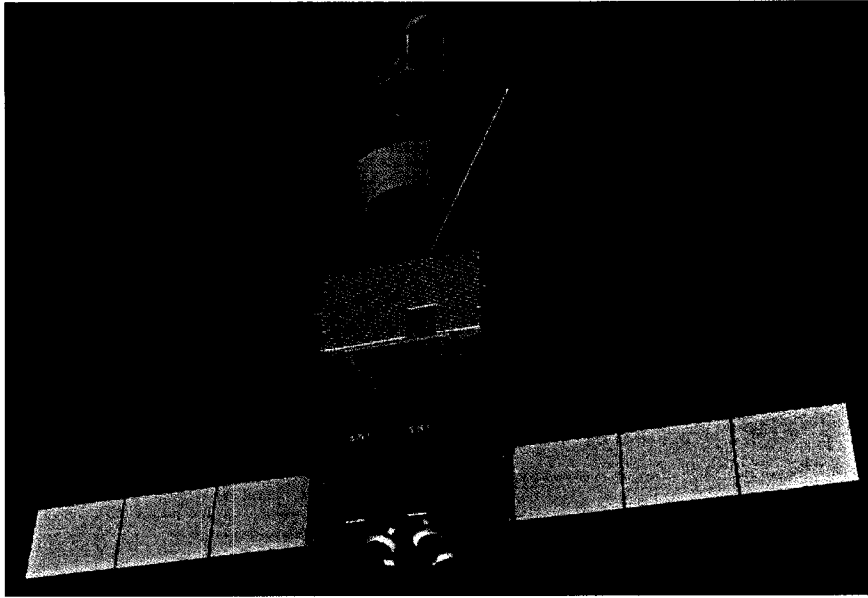


Figure 2.4: Illustration four parts of BepiColombo. Top to bottom: Mercury Magnetospheric Orbiter (MMO), Sunshield, Mercury Planetary Orbiter (MPO), Mercury Transfer Module. Courtesy ESA.

BepiColombo will be inserted into geostationary transfer orbit after the start. Then will be increased altitude of the orbit using chemical propulsion engine to 420 000 km. After the lunar flyby BepiColombo will reach the interplanetary trajectory. Then cruise trajectory by ion propulsion stage is scheduled using the Solar Electric Propulsion Module (SEPM) with 0.24 N thrust together with five gravity assists at Earth, two at Venus and finally another two using Mercury gravitational pull. On arrival to Mercury, ion propulsion stage will assist its Mercury arrival. Capture and insertion will be assisted by chemical propulsion engines within the MPO [Yarnoz *et al.*, 2006].

The objectives of the mission could be summarized into the several questions: 1) What can we learn about formation of our solar system from the structure of the planet Mercury? 2) Why only Mercury has different normalized density compared to all other terrestrial planets (including Moon)? 3) What can we say about the core? Is it liquid or solid?

	MPO	MMO
Stabilisation	3-axis stabilised	15-rpm spin-stabilised
Orientation	Nadir	Spin axis at 90 to Sun
Spacecraft Mass	500 kg	250 kg
Payload Mass	60 kg	40 kg
Power	450 W	300 W
TM band	X/Ka-band	X-band
Deployment	400 1508 km	400 11 824 km
Lifetime	> 1 year	> 1 year
Data volume	1550 Gb/year	160 Gb/year
Avg. data rate	50 kb/s	5 kb/s
Thrusters	Ion thrusters	
Other equipment	high temperature resistant thermal protection, solar arrays	

Table 2.4: Spacecraft summary adopted from official BepiColombo website.

Mercury Planetary Orbiter (MPO):	
BELA	BepiColombo Laser Altimeter
ISA	Italian Spring Accelerometer
MERMAG	Mercury Magnetometer
MERTIS-TIS	Mercury Thermal Infrared Spectrometer
MGNS	Mercury Gamma ray and Neutron Spectrometer
MIXS	Mercury Imaging X-ray Spectrometer
MORE	Mercury Orbiter Radio science Experiment
PHEBUS	Probing of Hermean Exosphere by Ultraviolet Spectroscopy
SERENA	Search for Exosphere Refilling and Emitted Neutral Abundances
SIMBIO-SYS	Spectrometers and Imagers for MPO BepiColombo Integrated Observatory System
SIXS	Solar Intensity X-ray Spectrometer
Mercury Magnetospheric Orbiter (MMO):	
MERMAG-M/MGF	Mercury Magnetometer
MPPE	Mercury Plasma Particle Experiment
PWI	Plasma Wave Instrument
MSASI	Mercury Sodium Atmospheric Spectral Imager
MDM	Mercury Dust Monitor

Table 2.5: BepiColombo payload summary.

2.3.1 Scientific Payload

In Table 2.5 are summarized technical details for selected instruments in preparation for BepiColombo mission with more details provided for some of the instruments below.

BepiColombo Laser Altimeter

The BepiColombo Laser Altimeter (BELA) will measure topography and surface morphology of Mercury as well as local surface roughness and the albedo. From the data we will be able to construct digital terrain model which allows to invert Hermean gravity data from MORE experiment. The instrument will have 2 ns timer resolution and will acquire data every 250 m on ground-tracks separated 25 km at the equator and crossing at the poles.

Mercury Radiometer and Thermal Infrared Spectrometer

High resolution spectral analysis for detailed mineralogical composition survey of Mercury's surface together with surface temperature and thermal inertia will be conducted. MERTIS will cover a wavelength range from 7 to 14 μm with resolution up to 90 nm by using IR-imaging spectrometer. The spatial resolution is 500 m and can be adopted to optimize S/N ratio so 5-10 % of the surface will be scanned with higher resolution. The instrument will use micro-bolometer technology which allow to sustain high temperatures without using any external cooling mechanism. One of the objectives is to study bright spots in polar regions reported from the ground-based observations.

Ultraviolet Spectrometer

PHEBUS is a dual FUV-EUV spectrometer plus two-channel detector of potassium and calcium at 404 nm and 422 nm respectively. The spectrometer will measure wavelength in range from 55 to 315 nm having resolution 1 nm. The instrument is a cooperation between Japan, Russia and France. The main objectives should cover the detection of new species; measuring number density of constituents of exosphere and vertical structure for various configuration of Sun/Mercury; and local and temporal variation in terms of hours.

The Solar Intensity X-ray and particle Spectrometer

SIXS consists of X-Ray spectrometer with time resolution up to 1 s measuring energies 1-20 keV and other two spectrometers able to operate simultaneously are for protons 0.5-30 MeV and electrons with energies 0.1-3 MeV. Both channels are able to measure count-rates up to 20000 cps and Field-Of-View 180°. For spectral calibration of X-Ray detector, the instrument is equipped with Fe55 radioactive source. The objectives are to provide information about solar wind and couple the data with X-Ray observation of surface from MIXS instrument and to study X-Ray corona and solar flares of the Sun.

Search for Exosphere Refilling and Emitted Neutral Abundances

SERENA will consist of four spectrometers: 1) Emitted Low-Energy Neutral Atoms (ELENA) measure gasses escaping from surface by measuring both the velocity and distribution by reconstructing the data from 2D data array sensor. 2) STart from a ROTating Field mass spectrOmeter (STROFIO) is a neutral particle spectrometer which measure the composition of gasses escaping from the surface. The instrument uses a technique where particles are ionized first so trajectory can be adjusted by external electric field and focused on sensor which then measure charge to mass ratio. 3) Miniature Ion Precipitation Analyser (MIPA) monitor the ion flux angle; energy and then velocity. 4) Planetary Ion CAMera (PICAM) is an ion mass spectrometer in form of all-sky camera for charged particles. Its purpose is to study processes of neutral ions released from the surface and eventually ionized. SERENA should answer the question about how did thin exosphere produce by ionized atoms from solar wind and magnetosphere of Mercury.

Mercury Magnetometer

MERMAG consists of two sensors thermally isolated from a 1.5 m long boom. One sensor will be mounted at the end of the boom and a second at distance 1 m from spacecraft. This configuration reduces local magnetic field caused by the spacecraft itself. The instrument support several scientific operation modes with different bit-rates. The scientific objectives for MERMAG are to find the source of the magnetic field and to understand the evolution of the field. The mission should determine the strength of the field up to octopole with high accuracy. The measurements will be performed on both spacecrafts (MPO and

MMO). Another objective is to describe and to help understand dynamic effects of solar wind interacting with Hermean magnetic field.

Mercury Imaging X-ray Spectrometer

MIXS will measure the spectrum of light from the Sun reflected from the surface of the planet. For the calibration output from related instrument SIXS will be used. The instrument consist of two channels: i) MIXS-C with wide Field-Of-View and broad range of energies for overall scanning. ii) MIXS-T is an imaging telescope with a narrow Field-Of-View and high resolution. Instruments are cooled to -10° C and use GaAs common pixel arrays. Both day and night side of the planet will be scanned since it is expected that on the night side there is a large flux contribution from auroral arcs. The total abundances will be obtained due to the support from calibration instrument (SIXS). Few monolayers of the surface in the 0.5-7.5 keV energy range will be scanned for Mg, Al, Si, S, Ca, Ti, Fe, K, P to produce global elemental abundance maps.

Chapter 3

Remote measurements

The history of observations of Mercury started many years before the Mariner 10 mission in 1974 and 1975. In this chapter we summarize some of the known facts about Mercury with focus on the remote measurements. Because the ground based observations measure only on the neutral exosphere, the results are not significant from the particle tracing point view.

3.1 Observations

The summary from observations, modeling and in situ measurements can be found in Table 3.1 [e.g., *Killen and Ip, 1999*] in a form of surface and total column abundances. The ground based observations become a very common tool for discovering high column abundances of sodium by *Potter and Morgan [1985]* and later on potassium [*Potter and Morgan, 1986*]. By further investigation of the sodium atmosphere, *Killen et al. [1990]* showed high-latitude abundances of Na and K which vary on timescales less than 1 day which are poorly understood up till now.

Two elements, K and Na, are the most studied elements in the Hermean exosphere because they are easily observed from Earth by analyzing spectra of the light. Because K is sputtered at 4000 - 12000 K and Na at 2000 - 6000 K we can observe big differences in Na/K ratio due to the energy [*Madey et al., 1998*] of observed particles. Other effect responsible for the observed Na/K ratio is different radiation pressure [*Smyth and Marconi, 1995*] (when neglecting gravitation force) acting on the atoms. Once atoms are ionized, the different gyroradii leads to the higher effective loss of K compared to Na ions. Those effects

Specie	Surface Abundance [cm^{-3}]	Total Zenith Column [cm^{-2}]
H	23; 230 ^a	3×10^9 ^b
He	6×10^3 ^a	3×10^{11} ^b
O	4.4×10^4 ^a	3×10^{11} ^b
Na	$1.7 - 3.8 \times 10^4$ ^a	2×10^{11} ^d
K	3.3×10^2 ^c	1×10^9 ^c
⁴⁰ Ar	$< 6.6 \times 10^6$ ^a	$< 2 \times 10^{13}$ ^b
²⁰ Ne	6×10^3 ^e (day) 7×10^5 ^e (night)	3.7×10^{10} ^b
H ₂	$< 2.6 \times 10^7$ ^a	$< 8.7 \times 10^{14}$ ^b
O ₂	$< 2.5 \times 10^7$ ^a	$< 9.6 \times 10^{13}$ ^b
N ₂	$< 2.3 \times 10^7$ ^a	$< 1 \times 10^{10}$ ^b
CO ₂	$< 1.6 \times 10^7$ ^a	$< 4.5 \times 10^{13}$ ^b
H ₂ O	$< 1.5 \times 10^7$ ^a	$< 1 \times 10^{12}$ ^f $< 1 \times 10^{14}$ ^b
OH		$> 1 \times 10^{10}$ ^{f,g}
Mg	7.5×10^3	3.9×10^{10} ^g
Ca	387 ^g	1.2×10^9 ^g
	< 239 ^h	$< 7.4 \times 10^8$ ^f
Fe	340 ^g	7.5×10^8 ^g
Si	2.7×10^3 ^g	1.2×10^{10} ^g
S	5×10^3 ^g	2×10^{10} ^g
	6×10^5 ⁱ	2×10^{13} ⁱ
Al	654 ^e	3×10^9 ^g

^a *Hunten et al.* [1988], measurements of upper limits

^b *Shemansky* [1988], Mariner 10 measurements

^c *Potter and Morgan* [1988]

^d *Killen et al.* [1990], measured abundance, subsolar

^e *Hodges* [1974], model abundance

^f *Killen et al.* [1990], model abundance

^g *Morgan and Killen* [1997], model abundances, “preferred” composition

^h *Sprague et al.* [1993], measured upper limit

ⁱ *Sprague et al.* [1995], predictions

Table 3.1: Atmospheric abundances for Mercury’s mean orbit; quiet Sun

could explain highly varying Na/K ratio reported to be from 80 to 250. The column abundances can vary due to the error in measurements in the case of K because of the weak spectral line and thus very noisy data. Compared to Moon distribution of Na has unexplained enhancements especially in high-latitudes attributed to the magnetospheric effect [Potter and Morgan, 1990, 1997b; Killen et al., 1998] or nonuniform distribution of material in regolith [Sprague, 1990; Sprague et al., 1997].

Due to the predicted lack of magnetic field, first publications overestimated content of He in Mercury exosphere. This element was observed by Mariner 10 at 584 Å by UVS spectrometer. It is generally believed that the main source of He comes from implantation of solar wind. The 1216 Å channel of Mariner 10 UVS spectrometer measured H above subsolar point. During two flybys two characteristic temperatures appeared in the observations. Thermal population of particles with temperature of 420 K and the cold one with temperature of 110 K. The possible cause of this difference may be particle transport from the dark side of the planet or particle population is simply released by non-thermal processes like surface chemistry reported by Potter [1995]. From the latest reports [Killen et al., 1997, 1998; Potter and Morgan, 1997b] the surface-like thermal corona (550 K) contain even suprathermal component [Potter and Morgan, 1997b].

3.1.1 Sodium and Potassium

Sodium and potassium discovery in the Hermean exosphere was one of the biggest surprises. First single-slit spectrogram was used which revealed sodium atmosphere [Potter and Morgan, 1985] summarized by Sprague et al. [1997] and one year later weaker potassium [Potter and Morgan, 1986] atmosphere was detected. Few years later followed by Potter and Morgan [1990], image slicer technique was used to reach better picture of the distribution by measuring column (or line-of-sight) abundances. These measurements assessed the total column abundances to be $1-3 \times 10^{11} \text{ cm}^{-2}$ atoms which would require supply of Na in order of $10^{23} \text{ atoms s}^{-1}$ to balance all loss processes by photo-ionization on the dayside and losses of the neutral atoms on the nightside.

Sodium and potassium species have almost the same column density distribution over the surface as reported by Potter and Morgan [1997a]. This could suggest that both Na and K have the common source of the particle genera-

	D ₁	D ₂
sodium	5896 Å	5890 Å
potassium	7699 Å	7664 Å

Table 3.2: Sodium and Potassium spectral line

tion and even the same loss process. The particles are most likely sputtering from the surface due to the collisions with solar wind protons penetrating the magnetosphere through the open field lines thus mainly in the north and south cusps regions. This is in agreement with images taken by using spectral line analysis of the light reflected from the surface of Mercury. Spectral line is a frequency with more resp. less (lighter resp. darker) photons compared to nearby frequencies depending on the emission direction of the photons. We can see spectral lines in entire electromagnetic spectrum from radio waves to gamma rays.

Sodium can be detected by sunlight scattered at the D₁ and D₂ spectral line summarized in Table 3.2. It was suggested by *Potter* [1995] that sodium in the atmosphere is produced by chemical reaction on the surface by precipitation of solar wind protons creating sodium vapor and water.

Potassium, on the other hand, is hard to measure. The D₁ spectral line is clear without atmospheric interaction but is very weak to observe. The D₂ spectral line is approximately twice as strong as D₁ emission but is masked by oxygen emission line in the Earth's atmosphere. Under the certain circumstances, *Potter and Morgan* [1997a] reported that those lines are separated (due to the Doppler effect) so we can image potassium in D₂ line. This happens only few times in a year. Potter demonstrated that both elements have the same distribution (Figure 3.2) with higher density at southern hemisphere and lesser at norther hemisphere. *Potter and Morgan* [1997a] suggested that some other factors than solar wind may have been involved in Na⁺, K⁺ generation since during their observation the solar wind radiation intensity increased by 15% but the abundance of the metal atom increased by 50%. Photoionization is supposed to be major reason of loss process of both atoms but potassium seems to be more rapidly removed from atmosphere than sodium.

In Figure 3.2 by *Potter and Morgan* [1997a] we can see distribution of potassium with density peak at subsolar point. Such distribution can be attributed to the photo-stimulated desorption with density falling with $\cos(\chi)$ where χ

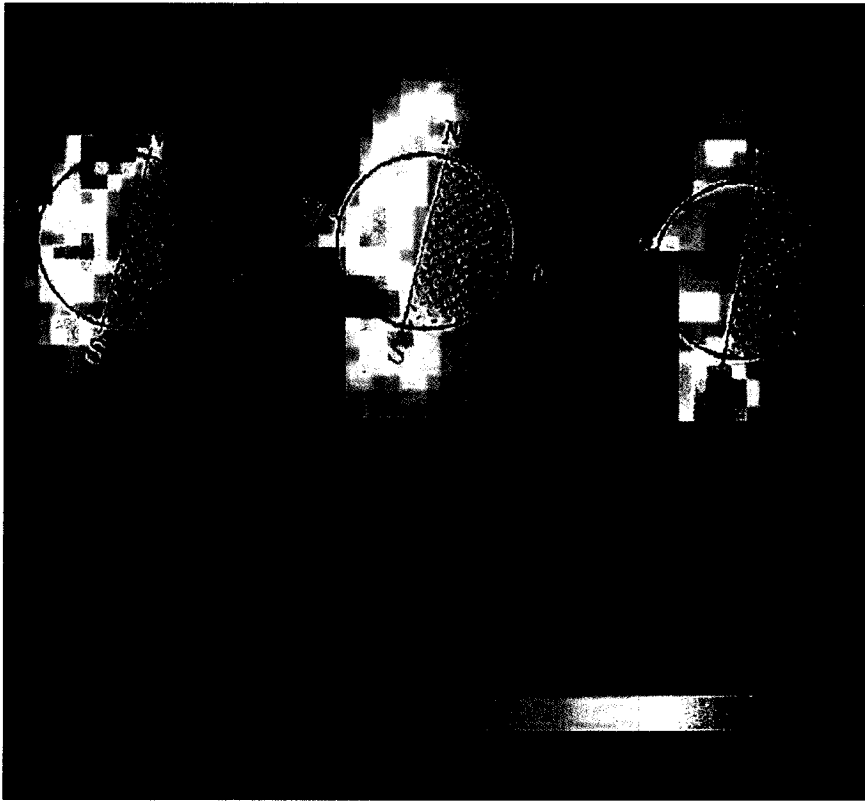


Figure 3.1: High latitude enhancements of Na measured by *Potter and Morgan* [1997b] on July, 1994 for three consequent days 20 - 22 July, indicating rapid changes of distribution in time, in this case on scales of one day. The color bar represents rayleighs intensity.

is a zenith angle. Other observation, on the other hand, reveal down-dusk asymmetries summarized in *Sprague* [1992a] and *Sprague et al.* [1997] which conclude that those asymmetries come from storing of the gas on the dark side of the planet in the atmosphere and degassing when photoionization effects take place on the morning terminator. This explanation was later rejected by *Killen and Morgan* [1993b] since we are not able to measure such effects at reported enhancements.

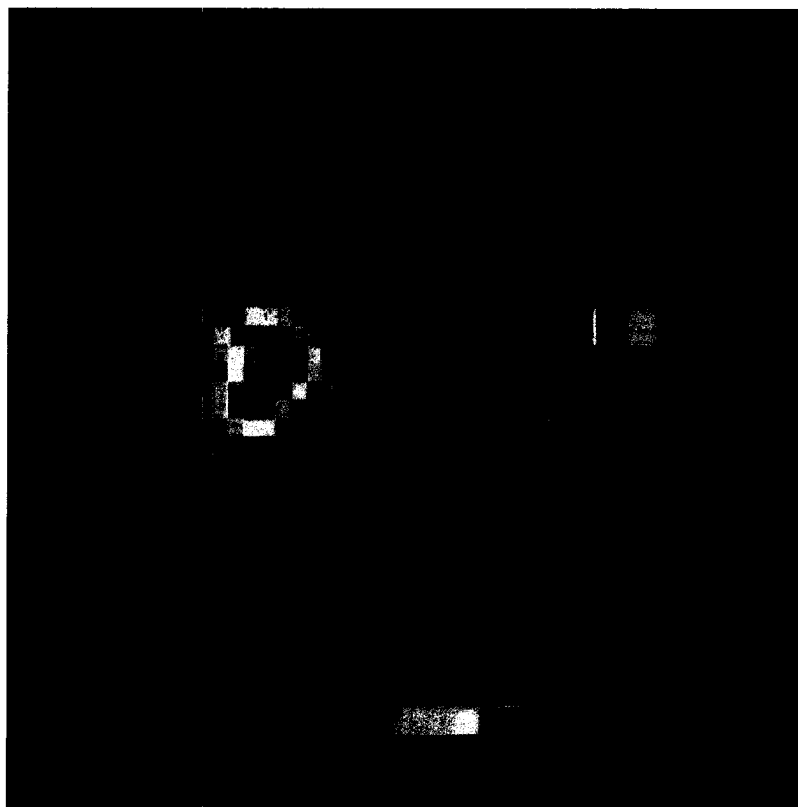


Figure 3.2: Distribution of potassium measured on December 7, 1990 by *Potter and Morgan* [1997a, Figure 2] reflected from the surface (left) and Mercury's corona scattered at 7664 Å. The color bar represents rayleighs intensity.

Chapter 4

Exosphere

The first surface-bounded lunar exosphere was detected by Apollo spacecraft by detecting He and Ar. From that time other bodies were confirmed to possess exosphere, namely at the Mercury and Europa. The exosphere is dynamical system coupling surface, magnetosphere and interaction with the solar wind. In this part of thesis we will describe sources and sinks of the particles with focus on the sodium together and with up to date knowledge of involved processes. We describe observations made by Mariner 10 (Section 2.1) as well ground based observations.

4.1 Introduction

From the time of the Mariner 10 mission, the exosphere was predicted to be only a very thin layer formed by diffusion, solar wind implantation with secondary thermal vaporization or sputtering. In that case Mercury would be very similar to other objects like the Moon. Using ground-based observations, high concentrations of Na and K was discovered by *Potter and Morgan* [1985, 1986]. After this discovery many ground-based observations were performed as well as radar imaging. In 1992 imaging of the polar regions the bright spots were discovered [*Harmon and Slade*, 1992] and they were attributed to iced water. The basic properties of Mercury and Moon (for comparison) are summarized in Tab. 4.1.

The review on Mercury and Moon by *Killen and Ip* [1999] defines an exosphere as “ensemble of atoms or molecules above a planet’s surface or atmosphere for which the mean free path is greater than the scale height (the e-folding

Property	Mercury	Moon
Radius [<i>km</i>]	2439	1738
Mass [<i>Earth mass</i>]	0.0554	0.0123
Subsolar temperature [<i>K</i>]	550-750	396-407
Minimal temperature [<i>K</i>]	40	40
Polar temperature [<i>K</i>]	174	159
Escape velocity [<i>km s⁻¹</i>]	4.25	2.38
Meteoroid impact velocity [<i>km s⁻¹</i>]	25	15
Surface gravity (equator) [<i>cm s⁻²</i>]	382	162.2
Mean density [<i>g cm⁻³</i>]	5.517	3.34
Orbital eccentricity	0.2056	0.0545
Obliquity	1.7-2.6'	1°32'
Inclination of equator to orbit	7.00487°	6°41'
Magnetic dipole moment	≈300 nT - R _M ³	0
Heat flow [<i>mW m⁻²</i>]	20	29
Sidereal rotation period [<i>days</i>]	58.6462	27.322
Diurnal period [<i>Earth days</i>]	176	29.5
Distance from Sun [<i>AU</i>]	0.306 - 0.46	1

Table 4.1: Physical Properties of Mercury and the Moon (for comparison)

height for density)". In the case of Mercury, the exosphere is directly connected to the surface and thus all interaction processes play an important role in forming the exosphere and particle distributions observed primarily defined by Jeans' escape, photo-dissociation, ionization and surface interactions.

4.2 Releasing processes

The exosphere is a closed system (see Figure 4.1) with its sources, mainly from lower layers of the planet, and sinks in the form of releasing of the material from the upper surface. The main sources of new material are diffusion of the material from non depleted layers of the planet or new regolith creation from outer source (i.e. micrometeorite precipitation). On the other hand five major release processes of atoms take place in Mercury's environment which deplete the surface layer (≈ 10 m)

- Photon stimulated desorption
- Solar wind sputtering

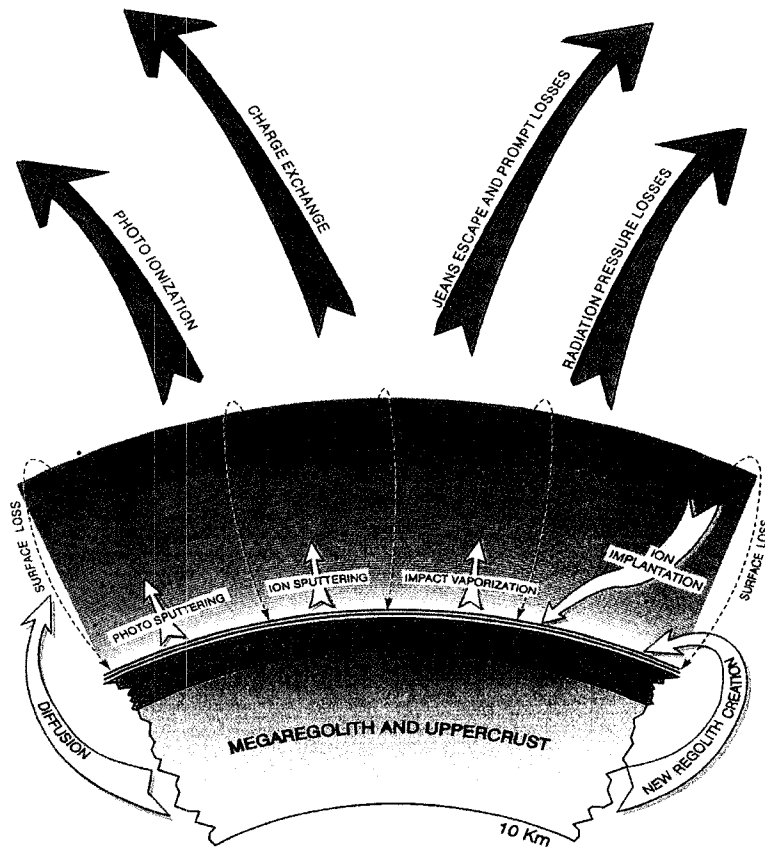


Figure 4.1: Cartoon representing sources and sinks of atoms in the environment of the Mercury. Adopted from *Morgan and Killen* [1997, Figure 1].

- Micro-meteoroid vaporization
- Thermal desorption
- Chemical sputtering

We do not consider chemical sputtering as one of the possible ejecting mechanisms as described by *Potter* [1995] because of the low energy of the ejected atoms. In this section we describe only first 4 processes using the probability function and energy distribution function. We are using *Leblanc and Johnson* [2003] as a main reference.

4.2.1 Surface temperature

Because of the eccentricity ($e \approx 0.2$) the Sun-Mercury distance varies significantly. The proximity from the Sun is directly related to the surface temperature by solar photon flux intensity and the zenith angle defining the effectiveness of the heating process. Assuming that temperature is constant ($T_S = 100$ K) on the night side of the planet, which means that the surface cool down almost immediately after reaching terminator, we only need to describe dayside of the planet.

Letting both latitude (θ) and longitude (ϕ) vary from -90° to 90° that means subsolar point is at longitude and latitude equal to zero we may describe temperature [Leblanc and Johnson, 2003] as

$$T_S = T_0 + T_1 \times (\cos \theta \times \cos \phi)^{1/4} \quad (4.1)$$

where $T_1 = 100$ K and T_0 is 600 K at perihelion and 475 K at aphelion.

4.2.2 Photon stimulated desorption (PSD)

Photon stimulated desorption is a dominant mechanism caused by the flux of UV photons exciting atoms from the surface. The PSD processes is selective releasing mechanism favoring mainly Na and K as described by *Yakshinskiy and Madey* [1999]. The most effective is for surfaces with temperature 250 K bombarded by UV photons with wavelength less than 300 nm. The yield of released particles is proportional to the flux of photons which is in turn proportional to the inverse of the squared heliospheric distance $1/R_{Hel}^2$ and cos function of zenith angle. Thus maximum is at subsolar point and no particles are released from the night side of the planet. Note that high particle flux on the dayside may lead to depletion of the material [Leblanc and Johnson, 2003] which would lower the efficiency of the PSD mechanism. Ejection rate of atoms from the surface of Mercury can be described by the following equation

$$\tau_{psd} = \Phi_{UV} \cos(\Theta) \times Q c_{Na} \quad (4.2)$$

where Φ_{UV} is UV flux of photons with energies greater then 5 eV [Yakshinskiy and Madey, 1999; Killen et al., 2001]; Θ is the zenith angle and Q is PSD cross section (typically 1×10^{-20} cm²). Sodium concentration c_{Na} is approximately 0.0053 so for atoms surface density $n_S = 7.5 \times 10^{14}$ cm⁻² we obtain sodium

surface density $n_{\text{Na}} = 3.98 \times 10^{12} \text{ cm}^{-2}$. The UV flux was estimated to be approximately $10^{14} A/R_{\text{orb}}^2$ by *Killen et al.* [2001] where A is scaling factor (≈ 1.5). The flux was estimated for events studied by *Killen et al.* [2001] to be $\approx (1.5 - 2) \times 10^{10} \text{ cm}^{-2} \text{ s}^{-1}$ photons [*Leblanc and Johnson*, 2003]. The energy E of released particles and angle between initial velocity and surface normal can be described by Maxwell-Boltzmann flux distribution function

$$f(E, \Theta) = 2 \cos(\Theta) \times \frac{E}{(k_{\text{B}}T)^2} \exp\left[-\frac{E}{k_{\text{B}}T}\right] \quad (4.3)$$

where k_{B} is Boltzmann constant and T is assumed to be 1500 K by *Leblanc and Johnson* [2003].

Several estimates of particle flux were available in the literature. *Shemansky and Morgan* [1991] estimated flux to be $410^8 \text{ m}^{-2} \text{ s}^{-1}$. *Wurz and Lammer* [2003] estimated surface average flux of Na atoms due to the PSD process to be $\approx 410^{12} \text{ m}^{-2} \text{ s}^{-1}$ with average release velocity of $v = 890 \text{ m/s}$ corresponding to 1100 K and surface density $n = 7.7 \times 10^9 \text{ m}^{-3}$ particles. Another estimates were made by *Killen and Morgan* [1993a] to be $2 \times 10^9 \text{ m}^{-2} \text{ s}^{-1}$; on the other hand *McGrath et al.* [1986] estimated flux $2 \times 10^{11} - 2 \times 10^{12} \text{ m}^{-2} \text{ s}^{-1}$ and *Lammer et al.* [2003] estimated $1 - 5 \times 10^{10} \text{ m}^{-2} \text{ s}^{-1}$.

4.2.3 Solar wind sputtering (SWS)

Depending on the solar wind conditions part of the planet surface can be directly exposed to solar wind particles. This region strongly depends on the orientation of the B_z component of the IMF and under the extreme conditions, as suggested by *Kabin et al.* [1999], the entire magnetosphere can be pressed towards the surface of planet. In this scenario the solar wind particles would have direct access to the surface on the dayside. Under the normal conditions energetic ions sputter neutral atoms and ions only in the cusp regions. The secondary source of sputtering by magnetospheric particles may play an important role in generation of exosphere as well. The amount of ions depends on composition of the material and is between 0.001 and 0.1 of neutral atoms with increasing values in case of oxidized surfaces.

Wiens et al. [1997] measured distribution of velocity on Na_2SO_4 in laboratory and concluded that distribution function is similar to a Thompson-Sigmund

energy distribution:

$$f(E, \Theta) = 2 \cos(\Theta) \times 2EU/(E + U)^3 \quad (4.4)$$

with speed peaking at 1.5 km/s in case of sodium, where U is a binding energy, approximately 0.57 eV. Note that we are using value of 0.27 eV assumed by *Leblanc and Johnson* [2003]. The yield of 0.15 atoms/ion was estimated by *Killen et al.* [2001], not considering porosity of the material. Another study by *Johnson and Baragiola* [1991] estimated yield to be 0.06 atoms/ion considering properties of the material. The ejection rate of sodium atoms in case of solar wind sputtering is then a product of yield, the flux of solar wind ions and the sodium concentration c_{Na}

$$\tau_{sws} = yield \times \Phi_{sw} c_{\text{Na}} \quad (4.5)$$

To initialize neutral atom flux from the surface due to the SWS process we need to identify the regions of increased flux of solar protons which penetrated magnetosphere and scattered on the planet. We use SW protons flux distribution map from self consistent hybrid simulation mentioned above with maximum flux concentrated in two narrow bands in mid latitude of 35-60°.

4.2.4 Micro-meteoroid vaporization (MMV)

Micro-meteoroids continuously bombard the surface of Mercury and this process provides another physical mechanism for particle ejection. A large meteoroid may weight up to 1-100 kg and may have velocities more than 30 km/s with respect to the planet. In this case, the ejected particles have Maxwellian distribution with temperature 4500 K and mean velocity of 2 km/s. Impacts of such magnitude are, however, relatively infrequent, so in the thesis we consider only light material ejecting particles with the same temperature $T = 3000$ K as suggested by *Leblanc and Johnson* [2003] with the most probable speed of 1.5 km/s and the average speed of 2.1 km/s. Because Mercury has a very eccentric trajectory we need to consider a change of the flux of micro-meteoroids with distance from Sun. *Killen et al.* [2001] suggested to add a power law factor of heliospheric distance R_{Hel} to the flux of space material per unit area as $R_{\text{Hel}}^{-1.9}$. Expecting the same situation as at the Earth [*Killen and Ip*, 1999] we assume that the flux of space material bombarding surface on the dawn side is two

times larger than that on the the dusk side. MMV vaporization is belived to produce from 25 % [Killen *et al.*, 2001] to 30 % [Leblanc and Johnson, 2003] of the entire sodium exosphere. Together with ion sputtering it is the only source of ejecta on the night side of the planet. The rate of sputtered particles by MMV was estimated as $0.15 - 14 \times 10^{23} \text{ s}^{-1}$ by Morgan *et al.* [1988] and $3.5 \times 10^{23} \text{ s}^{-1}$ by Leblanc and Johnson [2003].

4.2.5 Thermal desorption (THD)

To have the list of sources complete we have to mention process governed by temperature of atoms itself. The thermal desorption process and its importance in global view of the exosphere is described mainly in Sprague [1990, 1992a, b]; Hunten and Sprague [1997, 2002]. The nominal energy of released Na particles is between 0.03 and 0.05 eV which is not sufficient enough to escape from gravitational field and overcome solar wind radiation pressure acceleration. To overcome those forces requires energies around 2.07 eV (escape energy). Such particles reach maximally 60 km and then hit the surface again [Yakshinskiy *et al.*, 2000]. Other references on the other hand point out the importance of the process in terms of depleting the surface when temperature reach 400 K [Hunten and Sprague, 1997, 2002] on the morning side of the planet.

The paper by Yakshinskiy *et al.* [2000] study thermal desorption in laboratory on thin SiO₂ films. From experiments they concluded that number of sodium atoms per second can be expressed as

$$\tau_{\text{thd}} = \nu c_{\text{Na}} \exp \left[\frac{U}{k_{\text{B}} T_{\text{S}}} \right] \quad (4.6)$$

where ν is vibrational frequency, typically 10^{13} s^{-1} ; U is binding energy which for thermal desorption is between 1.4 and 2.7 eV but we can easily use average 1.85 eV; c_{Na} the sodium concentration in the surface; k_{B} is Boltzmann constant and T_{S} is surface temperature described in Section 4.2.1.

Energy distribution can be described by the Maxwell-Boltzmann flux distribution:

$$f(E, \Theta) = 2 \cos(\Theta) \times \frac{E}{(k_{\text{B}} T_{\text{S}})^2} \exp \left[-\frac{E}{k_{\text{B}} T_{\text{S}}} \right] \quad (4.7)$$

where E is energy of particle and Θ is angle between surface normal and velocity vector. As you can see temperature of the surface play important role in determining energies of released particles such as for $T_{\text{S}} < 350 \text{ K}$ energy is

almost zero.

4.3 Ionization

During the release process a small fraction of particles is already ionized at the time of release but major portion of ions in Mercury's exosphere comes from ionized neutral atoms through photoionization on the dayside of the planet. We can neglect other sources such as charge exchange and electronic impact since they are insignificant due to the low density of sodium specie. It takes approximately 3.3 hours to ionize atom by photoionization [*Smyth and Marconi, 1995*] at aphelion but this number can be up to 3 times smaller [*Milillo et al., 2005*] during high photon flux interaction from the Sun. In our model photoionization can happen only at the regions with direct access of photon flux (i.e. no photoionization on the nightside). Photoionization and loss rates of neutral atmosphere in general are summarized in Table 4.2.

Specie	Jeans' Flux ($T = 575$) $cm^{-2}s^{-1}$	Photoionization	Photoionization
		Lifetime ($R = 0.386$ AU) s	Loss Rate ($R = 0.386$ AU) $cm^{-2}s^{-1}$
H	8.6×10^5	2.0×10^6	1.5×10^3
He	51.4×10^7	2.8×10^6	1.1×10^5
O	1.8×10^{-3}	7.4×10^5	4.0×10^5
Na	2.3×10^{-9}	5780-13927	2.1×10^7 <i>a</i>
		5444-13118	2.3×10^7 <i>b</i>
		15817-38112	7.4×10^6 <i>c</i>
		14361-34605	8.7×10^6 <i>d</i>
K		9.0×10^4	1.5×10^5
Ar		4.8×10^5	4.2×10^7
H ₂		2.3×10^6	8.8×10^8
O ₂		2.6×10^5	2.7×10^9
N ₂		4.1×10^5	4.5×10^4
CO ₂		1.9×10^5	2.0×10^8
H ₂ O		3.7×10^5	2.0×10^8
OH		6.2×10^5	2.7×10^6
S		1.3×10^5	1.5×10^5
			1.5×10^8

Table 4.2: Atmospheric loss rates for quiet Sun (a,c) and active Sun (b,d) experimentally (a,b) and theoretically (c,d) determined.

Chapter 5

Numerical simulations

The numerical simulations is the tool commonly used to confirm theoretical hypothesis or observations done by various satellite missions. As performance and resource available to researchers grows very rapidly we are now able to simulate almost the entire magnetosphere of the planet with certain limitations. For our purposes we carried out two kind of the simulations: i) Hybrid; ii) Particle tracing; which will be described below.

5.1 Hybrid simulations

Two major approaches are used in today code development for the purpose of studying plasma phenomena. Because the plasma is behaving, on large scales, as a fluid we can use simple fluid equations and close the set of equations with an equation of state (EOS) to get a rough description of the plasma (see *Baumjohann and Treumann [1996]* for the introduction). The numerical solution of such set of equations is called magneto-hydrodynamic (MHD) codes. This approach is simple but has a few drawbacks. Because we neglect the gyration motion of particles (the fluid velocity represents bulk velocity of the guiding centers of the particles) all particle-wave interaction physics of gyration related processes is neglected. Consequently we can not observe any physical processes with typical length below the length of the particle gyroradius.

Another approach which solves the given problem from a different point of view are the particle-in-cell (PIC) codes. In this case we load macro-particles, each representing a cloud of real particles, with similar characteristic (position, velocity) into the simulation box and advance them in time by applying

Lorentz force. Then moments of the distribution function are collected and used to compute new EM fields which are again used to advance particles and so on. This kind of codes are able to describe even physical micro-scale processes in exchange of finer timestep (usually below gyroperiod of electrons) and increased level of noise. That means that PIC is not suitable for simulating a magnetosphere even for today's computers.

Fortunately we can use advantages of both and combine those two approaches into the hybrid code. In this case protons which play important role in forming of plasma envelope around the planet can be treated as macro-particles and electrons as a charge neutralising fluid can be described using MHD equations.

$$r_L = \frac{mv_{\perp}}{|q|B} \quad (5.1)$$

In the weak magnetic field, especially when we are talking about heavy ions, the gyroradius of the particles (Eq. 5.1) can reach lengths comparable to the radius of the planet. In our specific case we need to follow full particle motion and thus we are not able to employ magneto-hydrodynamic (MHD) codes which approximate motion of the plasma by hydrodynamic equations. The code we are using is described in article by *Matthews* [1994]. Another implementations can be found in *Harned* [1982] using a predictor-corrector scheme; *Winske and Quest* [1988] using a moment method or *Horowitz et al.* [1989] substepping magnetic field. It is a hybrid code treating ion species as macroparticles and electrons as a massless fluid which balances forces acting on electrons. CAM-CL is used to advance the solution and it stands for *Current advance method and cyclic leapfrog*. There are few differences when compared to other hybrid codes: i) Multiple ion species are treated in a single computational pass through data arrays; ii) CAM advances ionic current density instead of fluid velocity in other codes; iii) velocity is collected a half time step ahead, before equation of motion is applied; iv) magnetic field is sub-stepped using modified midpoint method [*Press et al.*, 1992] for better time resolution and to prevent dispersion.

5.1.1 Numerical Scheme

The system is governed by Vlasov-fluid equations:

$$\frac{d\mathbf{x}_s}{dt} = \mathbf{v}_s \quad (5.2)$$

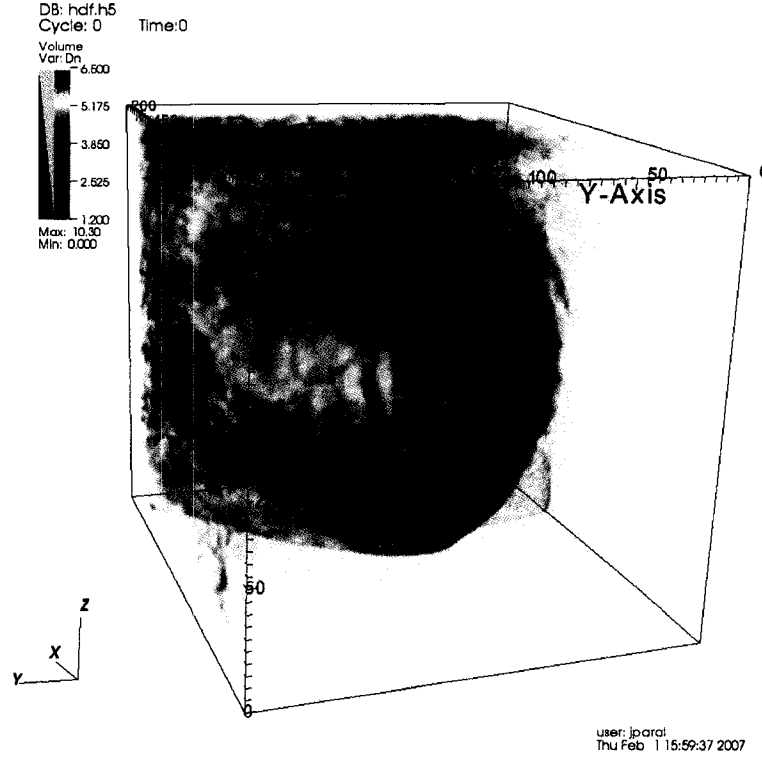


Figure 5.1: Example of the proton density output from the 3D hybrid simulation visualized by volume rendering technique. The boundary represents the bow shock of the planet for the fast solar wind ($v_{sw} = 5v_A$).

$$\frac{d\mathbf{v}_s}{dt} = \frac{q_s}{m_s}(\mathbf{E} + \mathbf{v}_s \times \mathbf{B}) \quad (5.3)$$

$$\frac{\partial \mathbf{B}}{\partial t} = -\nabla \times \mathbf{E} \quad (5.4)$$

$$\nabla \times \mathbf{B} = \mu_0 \mathbf{J} \quad (5.5)$$

$$n_e m_e \frac{d\mathbf{u}_e}{dt} = -n_e e \mathbf{E} + \mathbf{J}_e \times \mathbf{B} - \nabla p_e \quad (5.6)$$

$$p_e = n_e k_B T_e \quad (5.7)$$

where the symbols mean: ion position \mathbf{x}_s ; ion velocity \mathbf{v}_s ; ion mass m_s ; ion charge q_s ; electric field \mathbf{E} ; magnetic field \mathbf{B} ; magnetic permeability μ_0 ; current density \mathbf{J} ; electron number density n_e ; electron mass m_e ; electron fluid velocity \mathbf{u}_e ; magnitude of electronic charge e ; electronic current density $\mathbf{J}_e = -n_e e \mathbf{u}_e$; electron fluid pressure p_e ; Boltzmann's constant k_B ; and electron temperature T_e . The subscript s refers to ion specie. We are using Darwin's approximation so the displacement current is neglected in Maxwell's equation 5.5 and we are assuming massless electron fluid so lefthand term of equation 5.6 can be neglected. By adding a term $\eta \mathbf{J}_e$ on the right-side of equation 5.6, where η is resistivity of plasma, we can introduce an artificial resistivity into the system which cause the damping of high frequency waves. In the real situation, Eq. 5.7 describing isotropic and isothermal plasma is not valid and we have to use rather adiabatic approximation where we substitute electron temperature T_e by $T_e = T_{e0} (n_e/n_{e0})^{\gamma-1}$, where γ is an adiabatic index.

In this case the electric field is not time dependent and can be evaluated as a function of current density, magnetic field, charge density and electron pressure when we combine 5.6, 5.5, and substitute electron current density by $\mathbf{J} = \mathbf{J}_e + \mathbf{J}_i$ and charge density $\rho_c = n_s q_s$

$$\mathbf{E} = -\frac{\mathbf{J}_i \times \mathbf{B}}{\rho_c} + \frac{(\nabla \times \mathbf{B}) \times \mathbf{B}}{\mu_0 \rho_c} - \frac{\nabla p_e}{\rho_c} \quad (5.8)$$

substituting into equation 5.4 we obtain relation for advancing of magnetic field given by

$$\frac{\partial \mathbf{B}}{\partial t} = \nabla \times \frac{\mathbf{J}_i \times \mathbf{B}}{\rho_c} - \nabla \times \frac{(\nabla \times \mathbf{B}) \times \mathbf{B}}{\mu_0 \rho_c} \quad (5.9)$$

For advancing ionic current density we use momentum conservation equation while neglecting quadratic terms:

$$\frac{d\mathbf{J}_i}{dt} = n\mathbf{E} + \mathbf{J}_i \times \mathbf{B} \quad (5.10)$$

5.1.2 Model Scaling

For better scaling of the physical problems we use a scaling called *hybrid units*. We usually take protons of the solar wind as a reference to express other species and variables so hybrid units are dimensionless. If we mark all simulation hybrid units by index H and physical units by SI then each variable x can be expressed $[x]_H = [x]_{SI}/u$ where u is physical unit. Then when we adopt

variable	case I	case II
B_{sw} [nT]	46	21
v_{sw} [km/s]	600 ($5 v_{Asw}$)	250 ($3 v_{Asw}$)
n_{sw} [cm^{-3}]	73	32
$\rho_{sw,m0}$ [$kg\ m^{-3}$]	1.22×10^{-19}	5.34×10^{-20}

Table 5.1: Solar wind parameter of the study cases

mass of the proton m_p as unit of mass and charge e then we can define *hybrid units*: unit of magnetic field B_{SW} (magnetic field of solar wind); unit of speed v_A Alfvén speed; unit of time Ω_{pSW} (solar wind proton cyclotron time); unit of length $\Lambda_{pSW} = c/\omega_{pi} = v_A/\Omega_{pSW}$ (inertial length); unit of charge density n_{pSwe} ; unit of electric field $v_A B_{SW}$; unit of energy $\rho_m (c/\omega_{pSW})^3 v_A^2$ where c is the speed of light, $\Omega_{pSW} = eB_{SW}/m_p$ is solar wind proton gyrofrequency, and $\omega_{pi}^2 = n_0 e^2 / \epsilon_0 m_p$ is ion plasma frequency. Note that in hybrid units we keep magnetic permeability $\mu_0 = 1$, ion beta $\beta_i = \rho_m v_{th}^2$, electron beta $\beta_e = 2\tau_e$, and speed of sound $c_s^2 = (\beta_i + \beta_e)^2$ where $\tau_e = k_B T_e / e$ is a measure of the electron temperature.

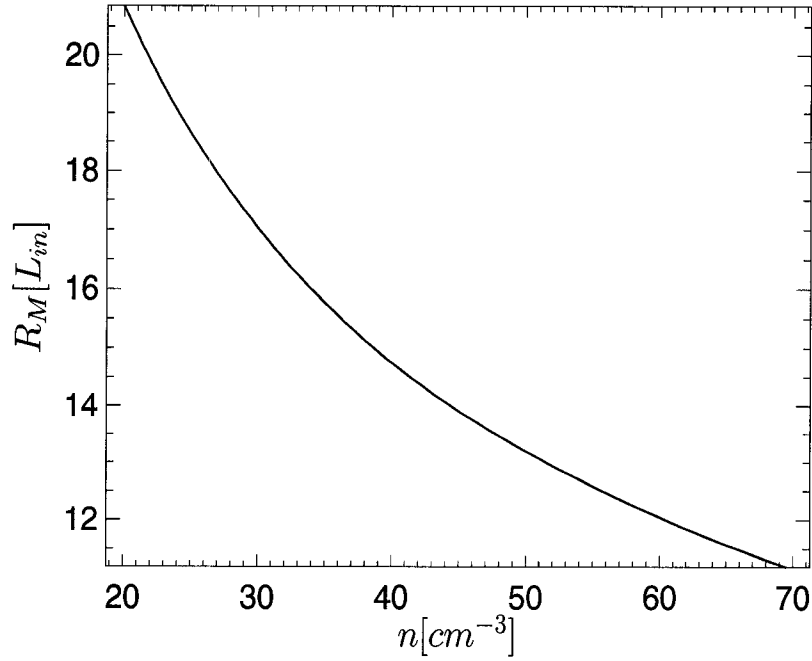


Figure 5.2: The radius of the planet Mercury in hybrid units as a function of solar wind density.

variable	sim. units	case I	case II	SI units
time	Ω_{pSW}^{-1}	0.23	0.50	s
length	c/ω_{pi0}	26.7	40	km
speed	v_{A0}	118	82	km/s
mass density	ρ_{m0}	1.22×10^{-19}	5.34×10^{-20}	$kg\ m^{-3}$
energy	$\rho_{m0}(c/\omega_{pi0})^3 v_{A0}^2$	3.23×10^4	2.30×10^4	J

Table 5.2: Conversion of simulation units to SI units for two study cases

As a consequence we need to change the size of an obstacle as we change the parameters of the solar wind. For example the length which is a function of solar wind density $\Lambda_{pSW} = c/\omega_{pi} \approx 1/\sqrt{n_0}$ require us to change the radius of the obstacle as we set up the initial conditions of the solar wind protons. On Fig. 5.2 we can see how to scale the radius of Mercury in terms of solar wind density.

5.1.3 Initialization

As a first step in our approach, we perform global hybrid simulations to obtain a steady state picture of the magnetosphere of Mercury. Our global hybrid model which is based on *Matthews* [1994] has been modified and applied to Mercury's magnetosphere by *Trávníček et al.* [2007]. In our model, ions are treated as macroparticles and electrons are a massless fluid which obeys charge neutrality condition. The model advances electric current in time using the cyclic leapfrog method of *Matthews* [1994] which has been extended to three dimensions by *Trávníček et al.* [2007]. Our simulations were performed on a structured computational grid encompassing $N_x \times N_y \times N_z = 560 \times 200 \times 200$ points and had a spatial resolution of $(\Delta x, \Delta y, \Delta z) = (0.4, 1, 1) \Lambda_{pSW}$ where Λ_{pSW} is proton inertial length $\Lambda_{pSW} = c/\omega_{pi}$. Macro particles were advanced with the time step of $\Delta t = 0.02 \Omega_{pSW}^{-1}$ and magnetic field was sub-stepped with a step of $\Delta t_B = \Delta t/10$. This improves time resolution of field solver and allows us to resolve high-frequency behaviour of the fields. Our simulations were initialized with a linear superposition of constant uniform interplanetary magnetic field (IMF) superimposed on the dipole magnetic field of the planet. The intrinsic dipole moment of Mercury was set to $M = 25,000 B_{SW} \Lambda_{pSW}^3 / \mu_0$. At the beginning of the simulation every cell was initialized with 70 particles having Maxwellian isotropic distribution with $\beta_p = n_{sw} T_p / B_{sw}^2 = 0.5$ where

n_{sw} is number density of solar wind protons, T_P temperature of protons and B_{sw} is interplanetary magnetic field. Electron fluid had $\beta_e = 0.5$. The plasma was continuously injected at the left boundary while open boundary conditions were applied on all other sides of the simulation box. All particles which hit the surface of the planet were removed from the simulation. In the interior of the planet we imposed $\partial\mathbf{B}/\partial t = 0$ and $\mathbf{E} = 0$.

5.1.4 Electric and Magnetic fields

Electric and magnetic fields together with mathematical description of the releasing processes are the only inputs into particle tracing simulation. For both study cases (Tab. 5.1.2) the electric and magnetic fields are presented in Figures 5.4 and 5.3, respectively. Color scale represents amplitude and arrows projection of orientation of a given variable into the plane of cut. The three Cartesian axis are scaled in radius of the planet R_M for convenience and positive X axis points towards the source of solar wind. As mentioned earlier B_Z is set to zero and vector \mathbf{B} forms angle 30° with negative X-axis. This configuration prevents the reconnection process to occur on the dayside of the planet, on the other hand we can clearly observe parallel and perpendicular bow shock in equatorial plane cut.

5.2 Particle tracing

Our goal is to trace heavy ions in a snapshot of static electric and magnetic fields evolved by hybrid code. No time dependency of the fields is assumed and thus no particle-wave interaction is captured. Throughout the motion of particles we expect very small changes of the fields. Also, low density of sodium specie allow us to assume that interaction with the fields is negligible. When those conditions are satisfied we can use particle tracing technique instead of adding particles self-consistently into the global simulation.

To move the particles in time we need to solve a Lorentz force equation 5.12 to advance the velocity coupled with Equation 5.11 for positions advancing.

$$\frac{d\mathbf{x}}{dt} = \mathbf{v} \quad (5.11)$$

$$\frac{d\mathbf{v}}{dt} = \frac{q}{M}(\mathbf{E} + \mathbf{v} \times \mathbf{B}) \quad (5.12)$$

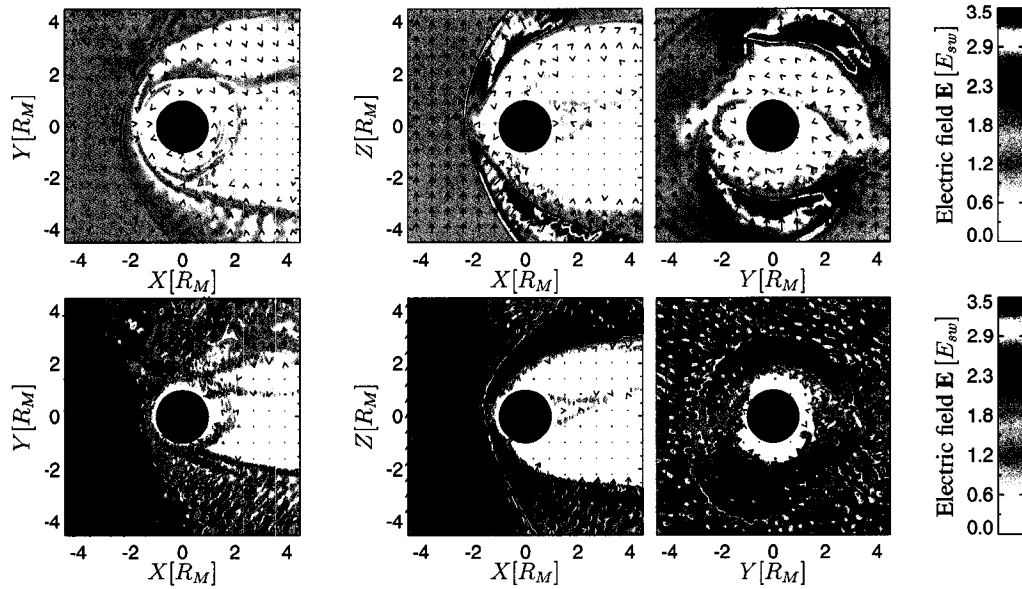


Figure 5.3: Electric field in (from left to right) equatorial, noon-midnight, dawn-dusk plane for slow (upper) and fast (lower) solar wind conditions. Color scale represents magnitude in the units of SW electric field E_{sw} and arrows represent projection of the field in the plane of cut.

where \mathbf{x}, \mathbf{v} are position and velocity of the particle; \mathbf{E}, \mathbf{B} are electric and magnetic field; and q, M are the charge and mass of the particle respectively. In Section 5.2.1 we explain the Leap-frog algorithm we used for pushing the particles. We adopted the same scaling of variables as hybrid code described in Section 5.1.2 so we avoided rescaling the fields into the SI units.

5.2.1 Algorithm

To advance particle positions in time we use a simple explicit Leap-frog algorithm successively applied CAM-CL hybrid simulation code by *Matthews* [1994] described in previous Section 5.1. This method advances velocity alternatively by leap-frogging position and velocity vectors at different time levels. We adopt commonly used notation where time levels are expressed as a superscript where 0 represents current time level and 1 is the next time level into which we are advancing the simulation.

Velocity is first half advanced in time using positions at time level zero $d\mathbf{v}^{1/2}/dt = q/M[\mathbf{E} + \mathbf{v}^0 \times \mathbf{B}]$ and then full step is done using previously com-

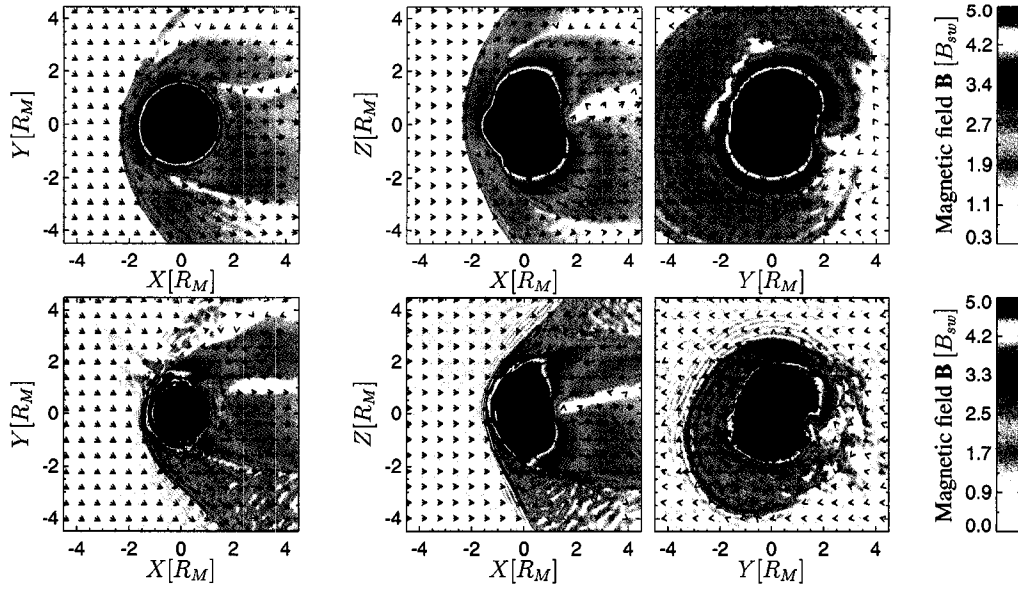


Figure 5.4: Magnetic field in (from left to right) equatorial, noon-midnight, dawn-dusk plane for slow (upper) and fast (lower) solar wind conditions. Color scale represents magnitude in the units of SW magnetic field B_{sw} and arrows represents projection of the field in the plane of cut.

puted value $d\mathbf{v}^1/dt = q/M[\mathbf{E} + \mathbf{v}^{1/2} \times \mathbf{B}]$. In the end, positions are updated using equation of motion $d\mathbf{x}^1/dt = d\mathbf{v}^1$.

$$\mathbf{v}^{n+1/2} = \mathbf{v}^n + \frac{\Delta t}{2} \frac{q}{M} [\mathbf{E}(\mathbf{x}^n) + \mathbf{v}^n \times \mathbf{B}(\mathbf{x}^n)] \quad (5.13)$$

$$\mathbf{v}^{n+1} = \mathbf{v}^n + \Delta t \frac{q}{M} [\mathbf{E}(\mathbf{x}^n) + \mathbf{v}^{n+1/2} \times \mathbf{B}(\mathbf{x}^n)] \quad (5.14)$$

$$\mathbf{x}^{n+1} = \mathbf{x}^n + \Delta t \mathbf{v}^{n+1} \quad (5.15)$$

To obtain the vector of the fields at the positions of the particles we use a bilinear interpolation. This algorithm uses tabulated values at the grid points (in our case fields) to estimate untabulated values inside of the grid cell. Disadvantage of bilinear interpolation is that the gradients are not smooth at the boundaries of the cells. This problem can be avoided by more sophisticated algorithm (i.e. bicubic interpolation or spline) in exchange of defining gradients and cross derivations at the grid points (for details see *Press et al.* [1992]).

Provided scheme is precise up to second order and to prove that the algorithm performs correctly and to asses optimal time step we run several testing

simulations with uniform magnetic field and no electric field to check if gyro-radius $r_g = mv_{\perp}/qB$ is conserved on the time scales of the simulations. The optimal time step was chosen to be $\Delta t = 0.01\Omega_{psw}^{-1}$ which is sufficiently smaller than gyro-period of sodium ions. We use output snapshot of magnetic and electric fields at simulation time $t = 40\Omega_{psw}^{-1}$ from hybrid simulation described above and we employ previously defined scaling from CAM-CL hybrid simulation.

We run all simulations to the time $1000\Omega_{psw}^{-1}$ which is already a steady state because typical transition time is several hundreds of Ω_{psw}^{-1} due to the acceleration in magnetosphere after ionization. In our case we use two times higher resolution $(\Delta x, \Delta y, \Delta z) = (0.2, 0.5, 0.5) \Lambda_{psw}$ with grid $N_x \times N_y \times N_z = 560 \times 200 \times 200$ compared to hybrid simulation.

5.2.2 Particle loading

Having the distribution function of energies and angle we need to find the transformation from a uniform distribution of random numbers ξ , $0 < \xi < 1$ to our nonuniform distribution of variable as discussed in [Lipatov, 2002]

$$\xi = D(x) = \frac{\int_a^x d(x')dx'}{\int_a^b d(x')dx'} \quad (5.16)$$

where $d(x)$ is a given distribution function and a and b are lower and upper boundaries respectively where function $d(x)$ is defined.

For Thomson-Sigmund distribution used for solar wind sputtering energy distribution defined as $f(E) = 2EU/(E+U)^3$ we obtain after applying previous procedure:

$$E = U \frac{-\xi_E - \sqrt{\xi_E}}{\xi_E - 1} \quad (5.17)$$

again for $0 < \xi_E < 1$

$$\Theta = \arcsin(2\xi_{\Theta} - 1) \quad (5.18)$$

$$\phi = 2\pi\xi_{\phi} \quad (5.19)$$

Gaussian random number generator is using Polar (Box-Muller) method; [Knuth, 1973, v2, 3rd ed, p122] where we generate two uniformly distributed numbers x and y from interval $[-1,1]$ and set $s = x^2 + y^2$ we repeat this process until $s \leq 1$

and then generate velocity with mean value μ and variance σ

$$v = \sigma \times y \sqrt{\frac{-2 \log s}{s}} + \mu \quad (5.20)$$

5.2.3 Output quantities

Through out the simulation we measure the first three moments of particle distribution and stored into the file. Particle number density weighted on the Cartesian computational grid. The interpolation function weight each particle i on grid point j by function

$$n = \sum_i \phi(\mathbf{x}_i) \quad (5.21)$$

where ϕ is a bilinear weighting function [Matthews, 1994]. Particle bulk velocity is similarly defined as:

$$\mathbf{u} = \frac{1}{n} \sum_i \phi(\mathbf{x}_i) \mathbf{v}_i \quad (5.22)$$

parallel and perpendicular temperature from pressure tensor

$$T_{\parallel} = \frac{m}{3k_B n} \sum_i \phi(\mathbf{x}_i) (\mathbf{v}_{i\parallel} - \mathbf{u}_{\parallel})^2 \quad (5.23)$$

$$T_{\perp} = \frac{m}{3k_B n} \sum_i \phi(\mathbf{x}_i) (\mathbf{v}_{i\perp} - \mathbf{u}_{\perp})^2 \quad (5.24)$$

On the planet surface we measure particle surface density $n_S = N/S$, number of particles N which hit the surface S in units of Λ_{psw}^2 . To have information about energy distribution we measure mean energy density per surface by $E_S = 1/n_S \sum_i v^2$.

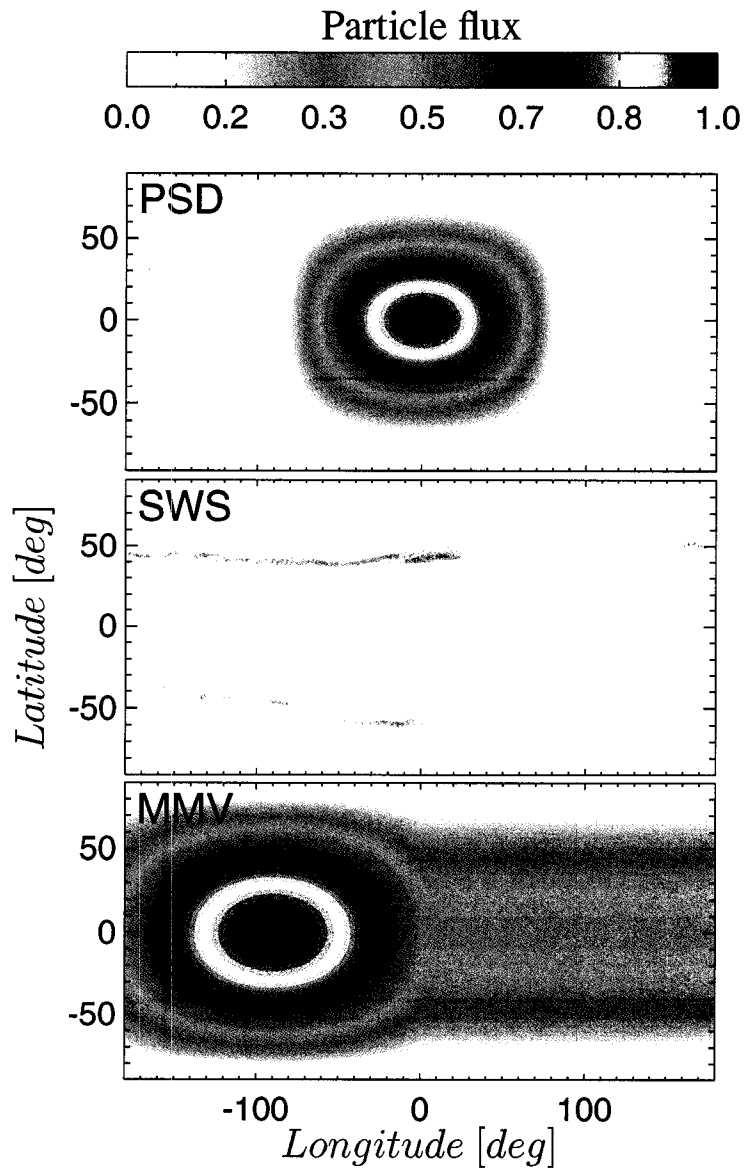


Figure 5.5: Macro-particle flux distribution of sodium neutral atoms from the surface of the planet. On x-axis is longitude and y-axis represents latitude with subsolar point in the center. Three process are presented here from top to bottom: PSD, MMV and SWS.

Chapter 6

Results

In this chapter we present results from several simulations. Two study cases of solar wind are first considered (described in Section 5.1) and analysed in terms of drift forces. For both cases, three major releasing processes of heavy sodium atoms from the Mercury's surface are simulated and traced forward in time. Next we study basic characteristics of sodium exosphere in terms of space missions of MESSENGER and BepiColombo.

6.1 Electric and magnetic drifts

In electric and magnetic field, several forces are acting on the charged particles in electromagnetic field. From the given fields we can directly compute drifts which allow us to detect and analyze cause of particle distribution in test particle simulations we performed. Because of static nature of EM fields we can neglect polarization drift defined as:

$$\mathbf{v}_p = \frac{1}{\omega_g B} \frac{d\mathbf{E}_\perp}{dt} \quad (6.1)$$

where change of electric field in time is zero and thus $\mathbf{v}_p = 0$. The rest of the drifts:

- Electric drift ($\mathbf{E} \times \mathbf{B}$)
- Gradient B drift (∇B)
- Magnetic field curvature drift (R_c)

will define the trajectory of the particles in simulation box. Here we present all three drifts (Figures 6.1, 6.2 and 6.3) for comparison in form of plots representing magnitude and direction in three major planes of cut through the planet.

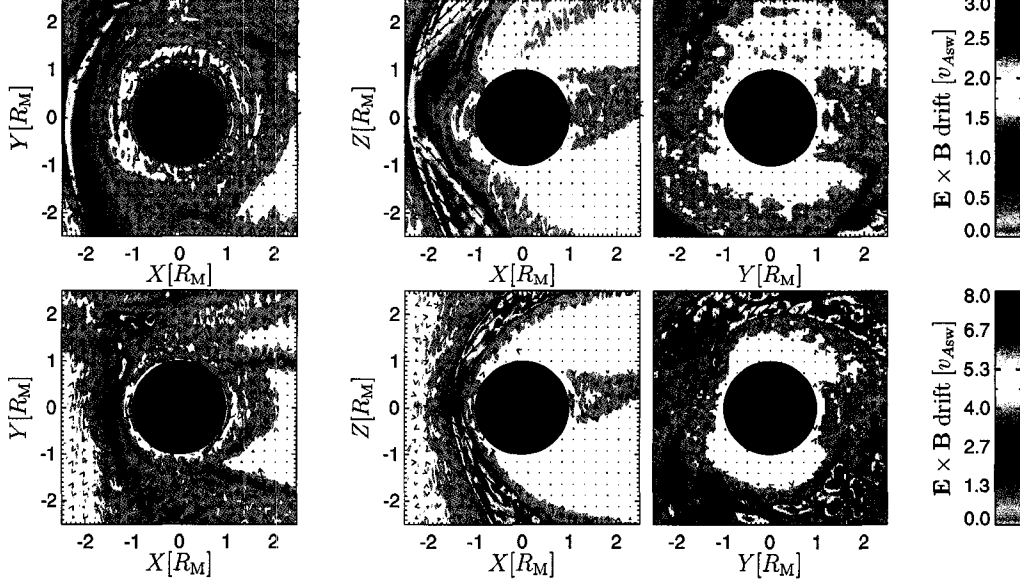


Figure 6.1: $\mathbf{E} \times \mathbf{B}$ drift in the vicinity of the planet for slow (top) and fast (bottom) solar wind conditions.

$\mathbf{E} \times \mathbf{B}$ drift

$\mathbf{E} \times \mathbf{B}$ drift is defined as

$$\mathbf{v}_E = \frac{\mathbf{E} \times \mathbf{B}}{B^2} \quad (6.2)$$

where \mathbf{E} and \mathbf{B} are electric and magnetic field respectively. We have to perform Lorentz transformation from observer's coordinate system, where planet is in the rest, to the *local rest coordinate system of plasma*. Electric and magnetic fields in the frame of reference moving with the velocity \mathbf{u} are defined as

$$\mathbf{E}' = \frac{\mathbf{E} + \mathbf{u} \times \mathbf{B}}{[1 - \frac{\mathbf{u}^2}{c^2}]^{1/2}} \quad (6.3)$$

and magnetic field is

$$\mathbf{B}' = \frac{\mathbf{B} + (\mathbf{u} \times \mathbf{E})/c^2}{[1 - \frac{\mathbf{u}^2}{c^2}]^{1/2}} \quad (6.4)$$

for small velocity $\mathbf{u} \ll c$ where c is speed of light we can transform fields into

$$\mathbf{E}' = \mathbf{E} + \mathbf{u} \times \mathbf{B} \quad (6.5)$$

and

$$\mathbf{B}' = \mathbf{B} \quad (6.6)$$

due to the Lorentz transformation (see *Baumjohann and Treumann* [1996, p. 16] for more details), where \mathbf{E}' is electric field experienced by particles, \mathbf{E} is electric field measured in hybrid simulation and \mathbf{u} is bulk flow velocity of the plasma at the given point.

In Figure 6.1 we can see the magnitude of $\mathbf{E} \times \mathbf{B}$ drift represented by color scale for slow (top) and fast (bottom) configuration of the solar wind. The arrows represent the orientation of the drift in the given plane of cut. The drift reach its maximum in the magnetosheath with values up to $3.5 v_{Asw}$ in the slow solar wind case and up to $8 v_{Asw}$ in the case of the fast solar wind. In both cases the orientation is predominantly from the polar to equatorial regions. This orientation cause the particle to populate two narrow bands of the surface in the midlatitude regions observed in Section 6.4 where particles, already accelerated, with usually very complicated trajectory in the simulation box return back on the dayside of the planet and hit the surface.

Gradient B drift

In inhomogeneous magnetic field, particles experience additional drift related to the different magnitude of the magnetic field during its gyro-period. Using Taylor expansion around guiding center of the particle

$$\mathbf{B} = \mathbf{B}_0 + (\mathbf{r} \cdot \nabla) \mathbf{B}_0 \quad (6.7)$$

where \mathbf{B}_0 is magnetic field and \mathbf{r} is distance from guiding center we can find by averaging over one period [*Baumjohann and Treumann*, 1996] that particle undergo magnetic ∇B drift defined as

$$\mathbf{v}_\nabla = \frac{mv_\perp^2}{2qB^3} (\mathbf{B} \times \nabla B) \quad (6.8)$$

Gradient B drift is presented in Figure 6.2. Color represents magnitude of the drift in units of v_{Asw}/v_\perp^2 where v_\perp is the velocity of the particle in per-

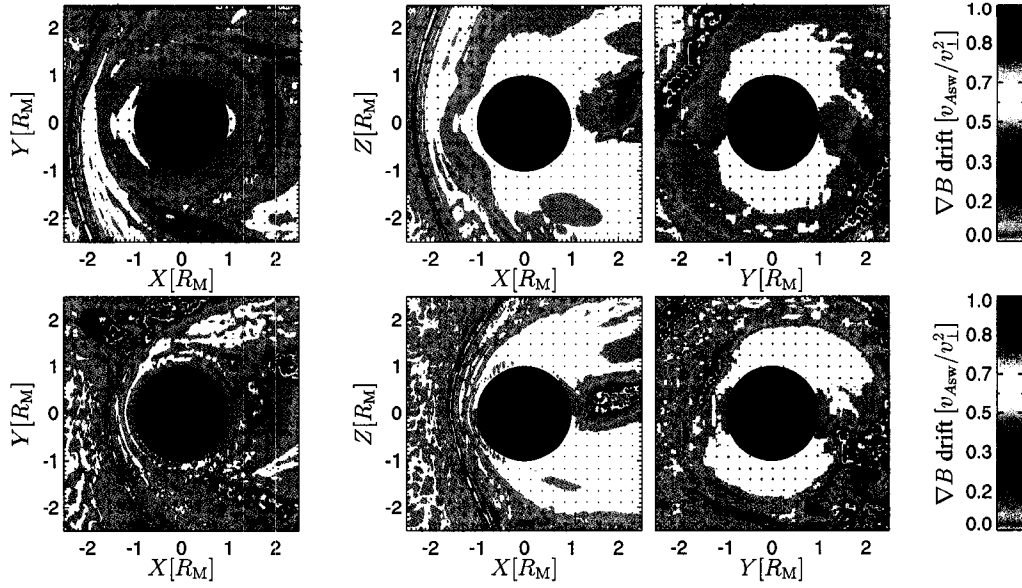


Figure 6.2: ∇B drift in vicinity of the planet. Color represents magnitude with maximum at the bow shock of the planet and arrows represent a direction in given the plane of cut. Top and bottom panel represent slow respective fast solar wind study case. Note, that units are in v_{Asw}/v_{\perp}^2 .

pendicular direction to the background magnetic field. Arrows then represent direction of the drift in the plane of cut. Two cases of solar wind are presented: fast (top) and slow (bottom) solar wind summarized in Section 5.1.3. As expected, gradient B drift support the partial ring current in vicinity of the planet and reach its maximum in bow shock of the planet (left and center panels) in both cases of solar wind. Gradient B drift has relatively small contribution into overall drift forces because of a small dipole moment of the planet compared to the strength of Earth.

Curvature drift

The curvature drift is defined as

$$\mathbf{v}_R = \frac{mv_{\parallel}^2}{qR_c^2 B^2} (\mathbf{R}_c \times \mathbf{B}) \quad (6.9)$$

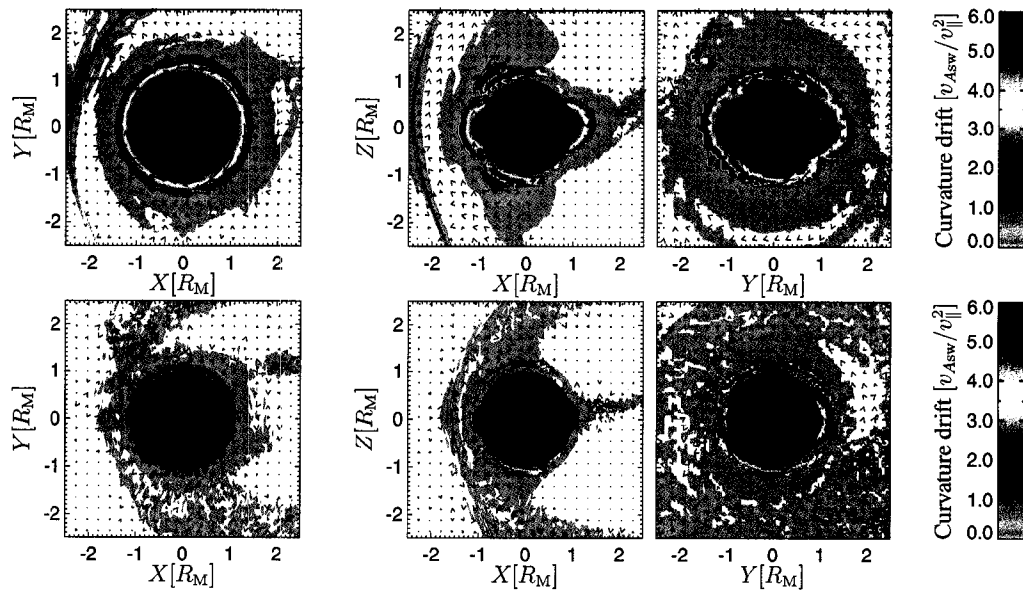


Figure 6.3: Curvature drift in vicinity of the planet. Color represents magnitude with maximum at the bow shock of the planet and arrows represent a direction in given the plane of cut. Top and bottom panel represent slow respective fast solar wind study case. Note, that units are in v_{Asw}/v_{\parallel}^2 .

where \mathbf{R}_c is vector of local curvature of magnetic field. To determine \mathbf{R}_c on the Cartesian grid we have to find local curvature vector $\boldsymbol{\kappa}$ which can be defined as

$$\boldsymbol{\kappa} = \nabla_{\perp} \ln B + \frac{\mu_0(\nabla \times \mathbf{B}) \times \mathbf{B}}{B^2} \quad (6.10)$$

where gradient in perpendicular direction ∇_{\perp} is

$$\nabla_{\perp} = \nabla - \frac{\mathbf{B}}{B} \left(\frac{\mathbf{B}}{B} \cdot \nabla \right) \quad (6.11)$$

Then local curvature radius \mathbf{R}_c points in the opposite direction then local curvature vector $\boldsymbol{\kappa}$ is defined as

$$\mathbf{R}_c = -\frac{\boldsymbol{\kappa}}{|\boldsymbol{\kappa}|^2} \quad (6.12)$$

thus local curvature of magnetic field is

$$\mathbf{R}_c = \left| \nabla \ln B - \frac{\mathbf{B}}{B} \left(\frac{\mathbf{B}}{B} \cdot \nabla \right) \ln B + \frac{\mu_0(\nabla \times \mathbf{B}) \times \mathbf{B}}{B^2} \right|^{-1} \quad (6.13)$$

where $\mu_0 = 1$ in hybrid units [Matthews, 1994].

In Figure 6.3 is the curvature drift. Magnitude is represented by color scale and arrows represent direction of the curvature drift in the given plane of cut. The units of all figures are in v_{Asw}/v_{\parallel}^2 . Small size of the planet supports relatively high curvature drifts, especially in the vicinity of the surface with maximum at the equator. Note that in slow solar wind when magnetic field is not completely compressed towards the surface, maximum of curvature drift forms ring with the peak at 1.3 - 1.4 R_M visible at upper left figure. For already accelerated particles with velocities more then 1 v_{Asw} in parallel direction is resulting drift the strongest one among all of the analysed drifts. Orientation of R_c drift supports ring current clearly as we can clearly see in bulk velocity presented in Section 6.5.

6.2 Particle statistics

From the running simulation we can perform several statistics based on the number of particles which cross the boundary N_{bnd} , hit the surface of the planet N_{pl} after the release or total number of emitted neutral atoms N_{emit} .

Rel. process	Slow SW		Fast SW	
	N_{bnd}/N_{pl} [%]	N_{pl}/N_{emit} [%]	N_{bnd}/N_{pl} [%]	N_{pl}/N_{emit} [%]
PSD	5.9	35.2	24.4	48.1
SWS	58.4	30.5	77.7	31.5
MMV	6.6	23.9	26.0	35.2
All	25.5	30.6	39.5	38.3

Table 6.1: Particle statistics. N_{bnd} , N_{pl} and N_{emit} are number of particles which left the simulation box through the boundary, hit back the surface and total number emitted into the system respectively.

Ip [1987] estimated the ratio N_{bnd}/N_{pl} to be 0.5 by comparing Mercury with the situation at Earth and he attributed this loss to the intercepting of the heavy ions by the magnetopause. This value is in agreement ($\approx 40\%$) with our result for the fast solar wind. In case of the slow SW the ratio drops to the $\approx 26\%$ which is considerably lower. Note that we considered all processes to release the same amount of particles. In the real situation we can expect the ratio to be different depending on which process is dominant. If the SWS would be the major releasing process then the ratio N_{bnd}/N_{pl} would be even higher since SWS is very effective in releasing particles in latitudes of open/closed field line boundary and thus most of the particles escape from the system.

The ratio N_{pl}/N_{emit} is very close for the both cases of the solar wind. For the slow SW it is $\approx 31\%$ whereas for the fast SW it is $\approx 38\%$. Again, this ratio can change dramatically in case different particle fluxes from the surface, especially when we can expect that SWS will be very effective releasing mechanism during events like coronal mass ejection. In case of the photon stimulated desorption, during the fast solar wind, almost 50% of the released neutral atoms precipitated back to the surface.

6.3 Single Particle

Several approaches are possible when particle tracing technique is used. When neglecting the option of particles tracing backward in time, we can trace enormous amount of particles to obtain statistics in a single computational cell (i.e. bulk velocity) or we can trace only a single particle and focus on the trajectory. From a history of such single particle we can identify a pattern of the typical particle trajectory at various regions.

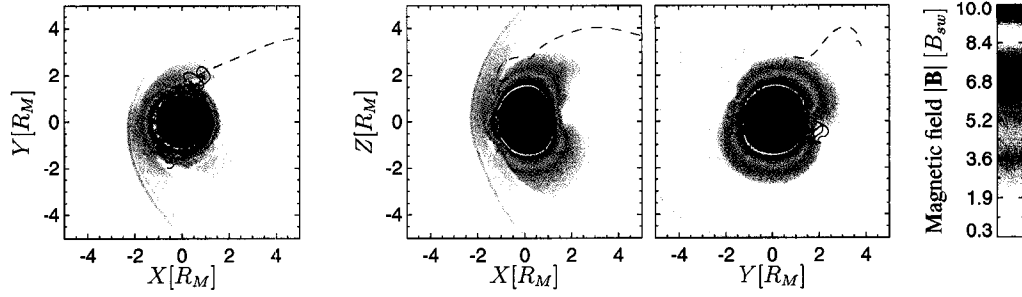


Figure 6.4: Projection of a single test particle trajectories released from the latitude of 40°S and for three longitudes: -90° (solid line), -30° (dotted line) and 50° (dashed line), measured from the subsolar point. The initial velocity of test particles is $|\mathbf{u}| = 0.01$. In the background is magnitude of magnetic field in units of solar wind magnetic field B_{SW}

In Fig. 6.4 is a cut through magnitude of magnetic field in (from left to right): equatorial plane; noon-midnight meridian plane and dawn-dusk plane. The X, Y and Z spatial axis are in units of Mercury planetary radius R_M . Color scale represents magnitude of magnetic field $|\mathbf{B}|$ in units of solar wind magnetic field B_{SW} . Besides of all characteristics of the well formed magnetosphere, namely bow shock, cusps regions or current sheet with reconnection X-line, three particle trajectories were picked up to represent common scenarios in the simulation. All three particles were released from the latitude of 40°S and from three different longitudes: -90° (solid line), -30° (dashed line) and 50° (dotted line), measured from the subsolar point. The initial velocity of all three particles is $|\mathbf{u}| = 0.01$ in radial direction. This configuration is typical for solar wind sputtering because of the initial latitude was chosen in open/closed field line boundary at about $35 - 55^\circ$ of latitude (see Sec. 6.4 for more details).

The first particle (solid line), after the release from the dawn side of the planet in mid-latitude region, is trapped in the dipole magnetic field of Mercury. Compared to the case at Earth, the dipole moment of Mercury is relatively small. Because of the high mass of sodium ions particle usually undergo only several periods before escape from the system or scatter to the surface again. During this motion particles participate into the ring current observed in bulk velocity in Section 6.5.

The second scenario (dotted line) where particles was released from the day-side sector on the south hemisphere. The particle follow the field line at L-shell 1.5 and then hit the surface at the north hemisphere at the same latitude with-

out any contribution to the ring current. Up to 50% of particles in case of PSD releasing mechanism, under the fast solar wind conditions, scatter back to the surface. Other mechanisms are not so effective and number of particles which return back to the surface is between 24% and 35% from the total number of released atoms. For details see Section 6.2 where statistics of released particles were presented.

The third particle (dashed line) simply escape from the tail of the magnetosphere after being energized by crossing of magnetopause. The particle can be captured in the current sheet where gain even more energy and can be injected back to the dayside. Such particles can then easily hit the surface of the planet. This usually happen in the mid-latitude region from two energetic bands of the increased particle flux from the surface as observed in the Section 6.4.

6.4 Surface of the Planet

An important view on the history of particle can reveal a deposit map of the particles and energy fluxes through the surface of Mercury. Using Table 5.1.2 for conversion of the units from hybrid into the SI units, we can transform an energy flux as follow

$$[\Phi_E]_{SI} = \Phi_E [\rho_{m0}(c/\omega_{pi0})^3 v_{A0}^2]_{SI} [c/\omega_{pi0}]_{SI}^{-2} [\Omega_{pSW}^{-1}]_{SI}^{-1} \quad (6.14)$$

where index H and SI represent hybrid and SI units respectively. Φ_E is flux of the mean energy through the surface of the planet and ρ_{m0} , c/ω_{pi0} , v_{A0} and Ω_{pSW} are hybrid unit of mass density, length, speed, and time respectively.

Particles, after released as neutral atoms, are ionized due to the photo ionization. Large number of particles (between 24% and 48%) then scatter on the surface of planet where cause secondary particle sputtering. This amount is strongly dependant on the releasing process involved and on the magnetosphere configuration as well as solar wind conditions as described in Section 6.2. Because of unknown initial particle number density we can only measure the macro-particle flux distribution through the surface of the planet as seen on Figure 6.5 and 6.7 for slow and fast solar wind respectively. As we can see, the distribution of the flux vary significantly depending on the releasing mechanism considered. The PSD process has almost zero particle flux through the surface on the night side of the planet as well as in a low latitude region

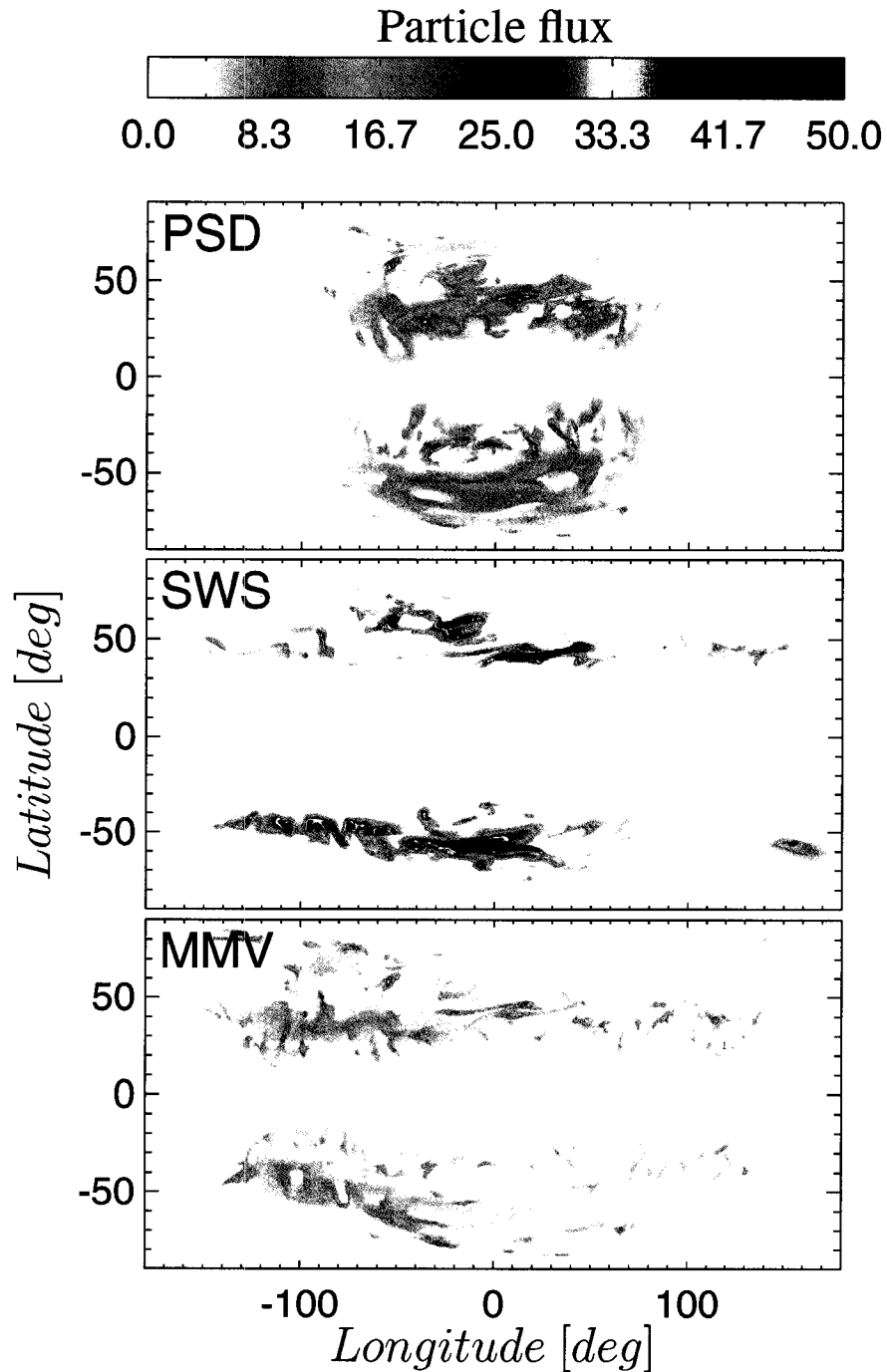


Figure 6.5: A planetary deposit map, under the slow solar wind conditions, of the super-particle flux (color scale) through the surface for three major releasing processes: PSD, SWS and MMV (from top to bottom). On x-axis and y-axis is longitude respectively latitude in Miller cylindrical projection of the surface. The subsolar point is in the middle of projection.

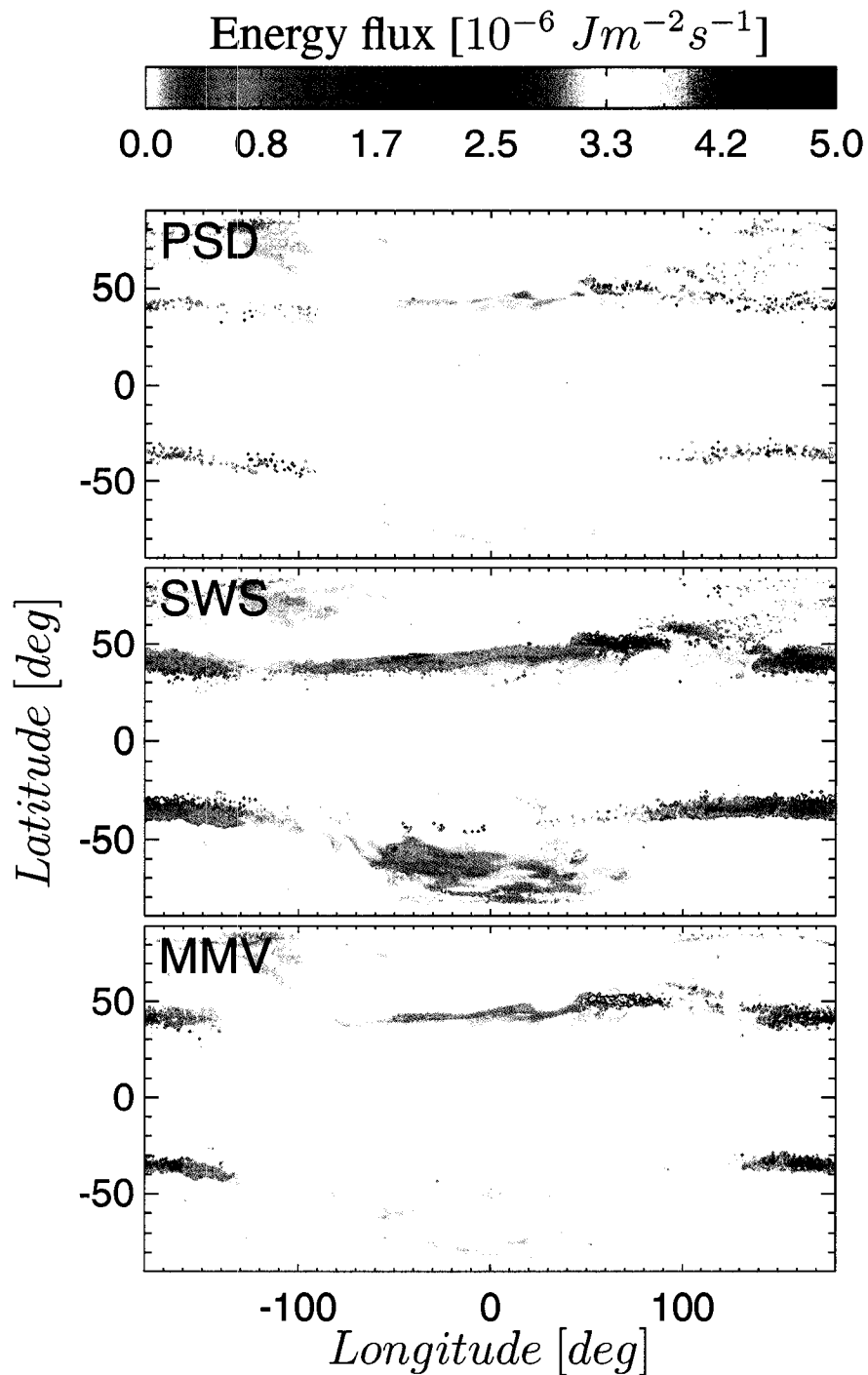


Figure 6.6: Mean energy flux (color scale) of sodium ions through the surface of the planet under the slow solar wind conditions for three major releasing processes: PSD, SWS and MMV (from top to bottom). On x-axis and y-axis is longitude respectively latitude in Miller cylindrical projection of the surface. The subsolar point is in the middle of projection.

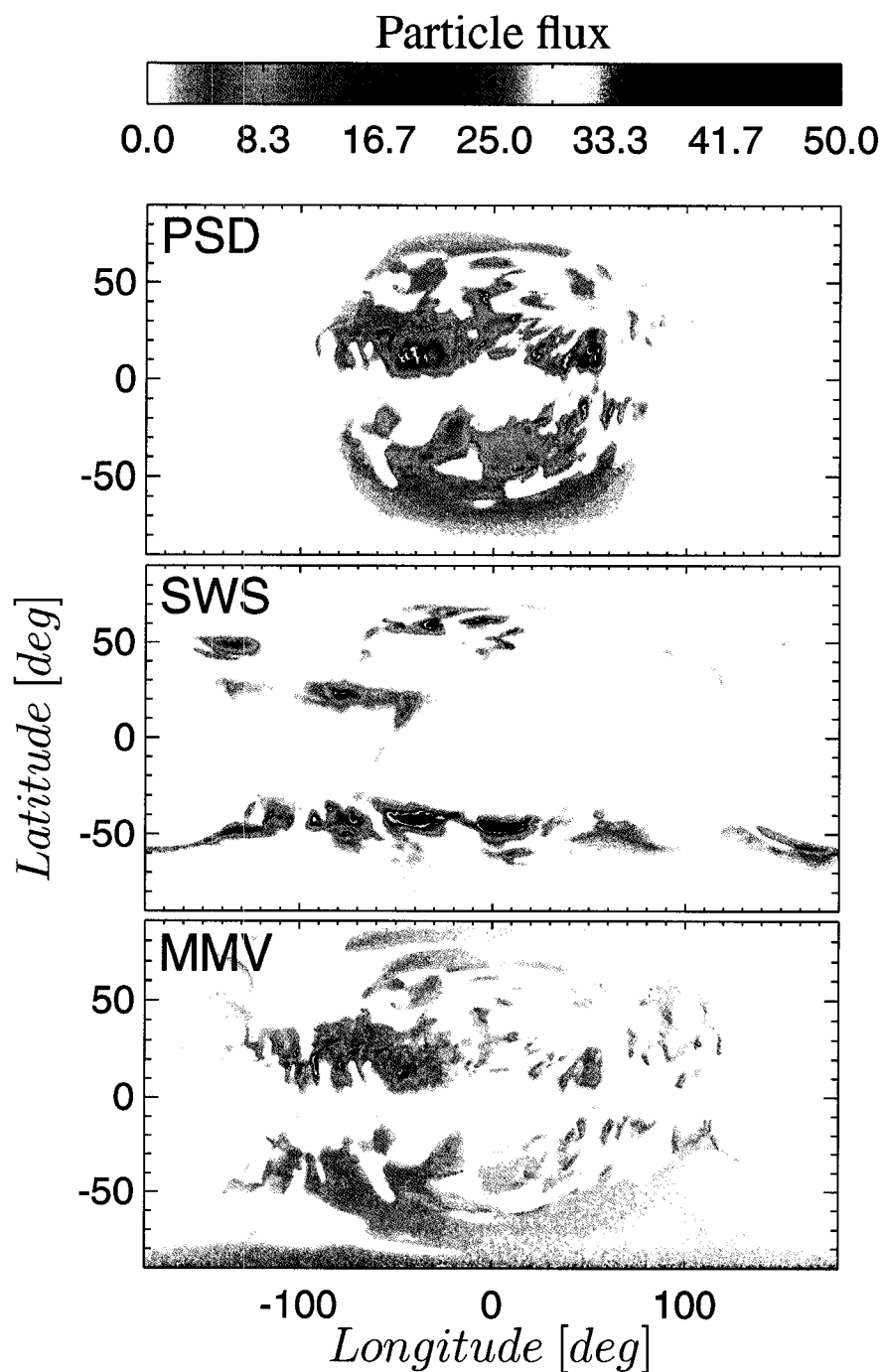


Figure 6.7: A planetary deposit map, under the fast solar wind conditions, of the super-particle flux (color scale) through the surface for three major releasing processes: PSD, SWS and MMV (from top to bottom). On x-axis and y-axis is longitude respectively latitude in Miller cylindrical projection of the surface. The subsolar point is in the middle of projection.

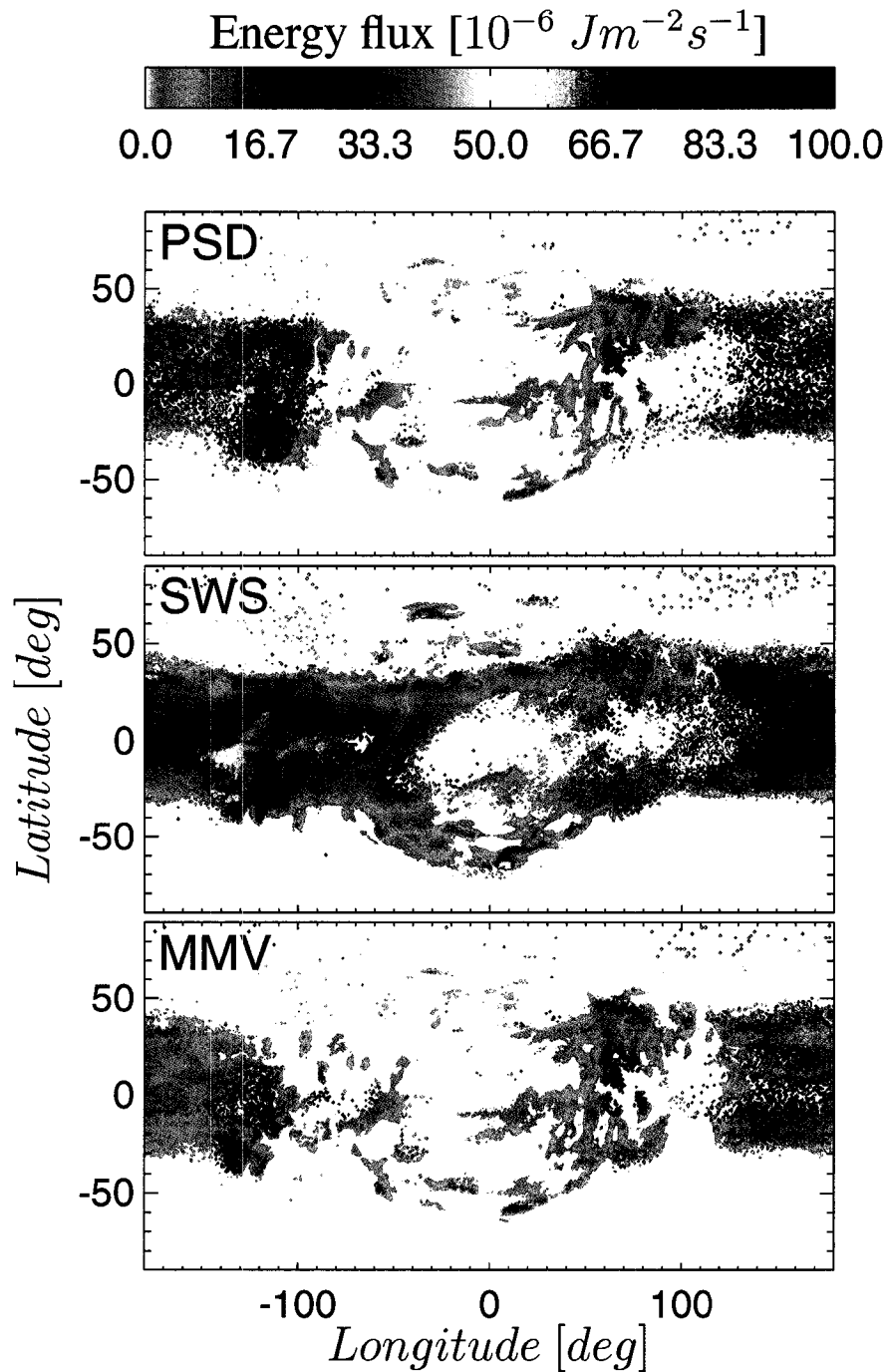


Figure 6.8: Mean energy flux (color scale) of sodium ions through the surface of the planet under the fast solar wind conditions for three major releasing processes: PSD, SWS and MMV (from top to bottom). On x-axis and y-axis is longitude respectively latitude in Miller cylindrical projection of the surface. The subsolar point is in the middle of projection.

around equatorial plane on the day side. The maximal particle flux forms two narrow bands in midlatitude which are shifted towards equator in fast solar wind case. The zero flux which is observed in the equatorial region then may be connected with very strong curvature drift as seen in Fig. 6.3. In the case of solar wind sputtering (SWS) process the flux distribution is strongly localized at the same latitude ($\approx 50^\circ$) for both hemispheres and practically all longitudes. Note also that the distributions are almost the same for slow and fast solar wind with higher flux on the dawn side than on the dusk side. The micro meteorite vaporization (MMV) scatter particles on the most of surface, except for the small part of the planet's night side, for latitudes less than 50° and for the low latitude region on the day side. This scattering is due to the particle initial flux distribution map of the MMV process which sputter neutral atoms from the entire surface of Mercury as seen in Fig. 5.5 representing the neutral atom flux distribution map.

Figures 6.6 and 6.8 represent particle mean energy flux distribution for slow and fast solar wind respectively. Units are converted using Equation 6.14 into SI units $Jm^{-2}s^{-1}$. Figures follow the same notation as super-particle flux for X, Y axis. Three panels represent different releasing mechanism. As seen from direct comparison of both figures, the maximal energy flux through the surface increased approximately 20 times in fast solar wind compared to the slow SW. This increase is due to the higher gradients in the compressed magnetosphere caused the stronger solar wind pressure. Surprisingly the same energy flux distribution in Figure 6.6 formed for all releasing processes. Two parallel symmetric bands formed in $\pm 40^\circ$ of latitude. Two major mechanisms can scatter particles at those specific latitudes. Firstly, when the pitch angle α (Equation 6.15) of bouncing particle is small

$$\alpha = \tan^{-1}(v_{\perp}/v_{\parallel}) \quad (6.15)$$

the mirror force is not sufficient enough to reflect the sodium ion at the mirror point and thus particle hit the surface. Secondly, the injection of energized particles from high altitude, above the polar region. We can see those particles in the bulk velocity plots (i.e. Fig. 6.9) as enhanced velocity above the magnetopause boundary layer in the azimuthal direction. Although this enhancement is in the north to south direction, in the case of SWS we can identify the higher velocity even in south to north direction. This could explain why the narrow

band in the mean energy flux is interrupted on the dayside of the south hemisphere for PSD and MMV processes but are not visible in case of SWS. The situation in case of fast solar wind is even more complicated. We can still identify the two narrow bands at latitudes $\approx 40^\circ$ but the energy flux is enhanced for all latitudes between those bands, especially on the night side of the planet. Even if particle flux on the dayside of PSD and MMV processes is large the energy flux of such particles is small. This is probably because the particles are quickly scattered on the surface before energizing.

6.5 Bulk velocity

On Figures 6.9-6.14 you can see the bulk velocity of the sodium ions Na^+ represented by color scale in units of Alfvén velocity v_{Asw} . particles were originally released from the surface of the planet by PSD, SWS, MMV processes. The bulk velocity is converted into spherical coordinate system so each row represents one component of the velocity in (from top to bottom) radial; longitudinal; and azimuthal direction. All Figures 6.9 - 6.14 of bulk velocity follow the same layout. The velocity converted into spherical coordinates allow us clearly identify the regions of particle injection into the surface (scattering), ring current, etc. Two cases of solar wind velocity are considered: i) slow solar wind $v_{sw} = 3 v_{Asw}$ (Fig. 6.9, 6.11, 6.13); and ii) fast solar wind $v_{sw} = 5 v_{Asw}$ (Fig. 6.10, 6.12, 6.14). The black line in all plates represents rough assessment of magnetopause. This assumption is based on the fact that on the magnetopause boundary is zero velocity of plasma in normal direction. We can see that so called magnetopause stagnation point is in the range of 1.2 - 1.7 R_M which is in agreement with theoretical expectations by *Baumjohann and Treumann* [1996] using Equation 6.16. Using typical parameters, we find out R_{mp} to be about 1.4 R_M .

$$R_{mp} = \left(\frac{K B_E^2}{2\mu_0 n_{sw} m_i v_{sw}^2} \right)^{1/6} \quad (6.16)$$

We considered various angles χ formed between the plane of cut and noon-midnight plane, namely $\chi = 0^\circ$ (noon-midnight plane in Fig. 6.9 and 6.10), $\chi = 60^\circ$ (Fig. 6.11 and 6.12), and $\chi = 90^\circ$ (dawn-dusk plane in Fig. 6.13 and 6.14).

All plates of bulk velocity show an increased velocity upstream of the magnetopause. Also note more than twice higher maximal velocities ($> 3 v_{Asw}$) in

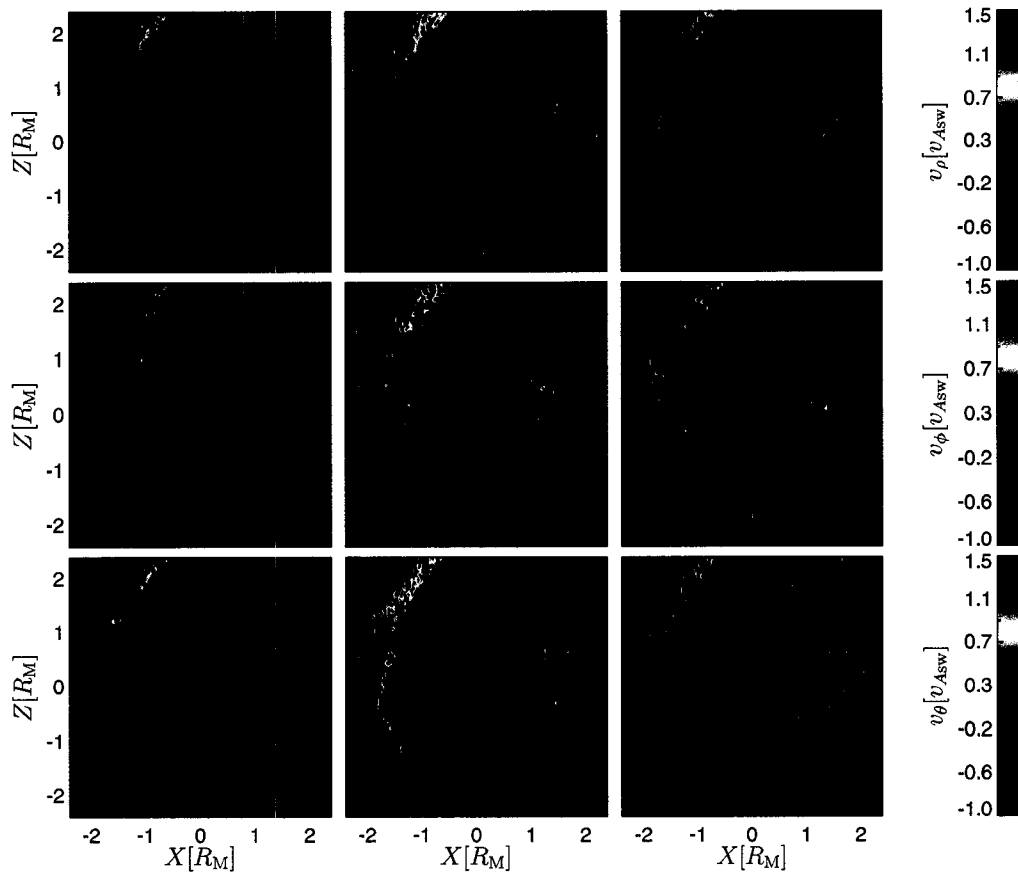


Figure 6.9: Bulk velocity in noon-midnight plane in units of Alfvén speed of solar wind v_{Asw} for slow solar wind $v_{sw} = 3 v_{Asw}$. Three major releasing processes are presented in each column: photon stimulated desorption (PSD), solar wind sputtering (SWS) and micro-meteorite vaporization (MMV). The velocity is transformed into spherical coordinate system: radial direction (top row); longitudinal direction (middle row); and azimuthal direction (bottom row). The black line represents an assessment of magnetopause.

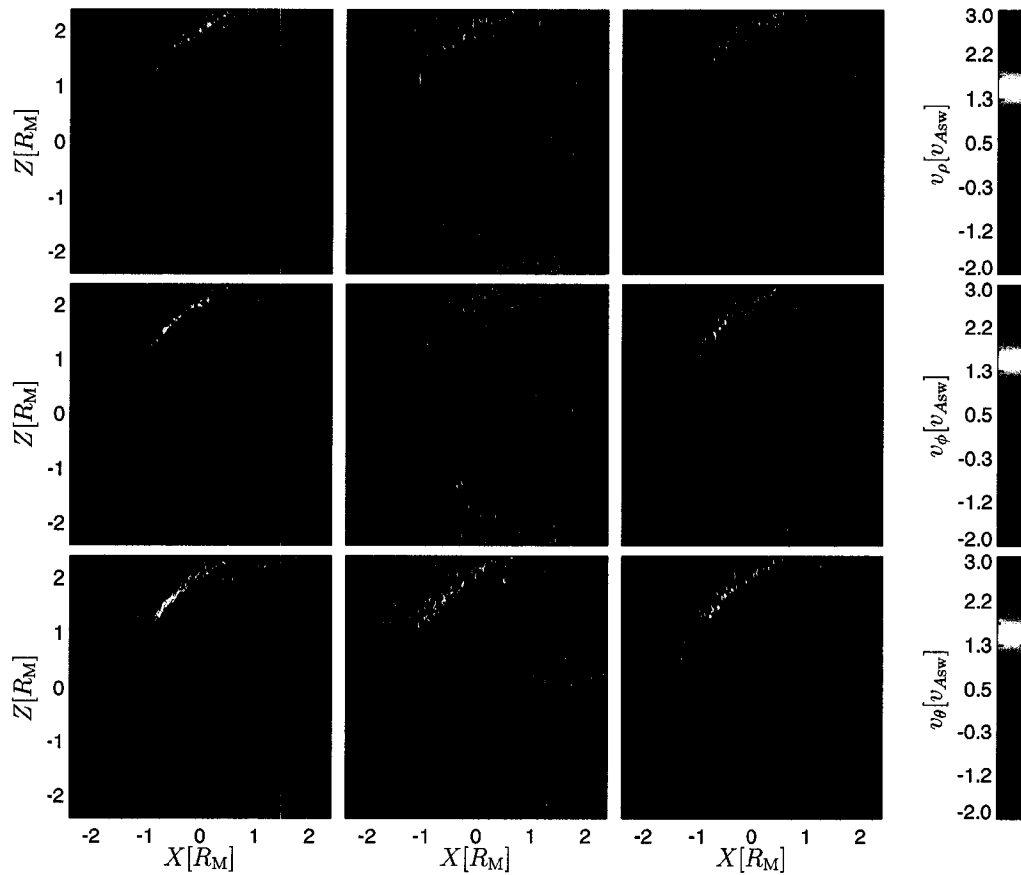


Figure 6.10: Bulk velocity in noon-midnight plane in units of Alfvén speed of solar wind v_{Asw} for fast solar wind $v_{sw} = 5 v_{Asw}$. Three major releasing processes are presented in each column: photon stimulated desorption (PSD), solar wind sputtering (SWS) and micro-meteorite vaporization (MMV). The velocity is transformed into spherical coordinate system: radial direction (top row); longitudinal direction (middle row); and azimuthal direction (bottom row). The black line represents an assessment of magnetopause.

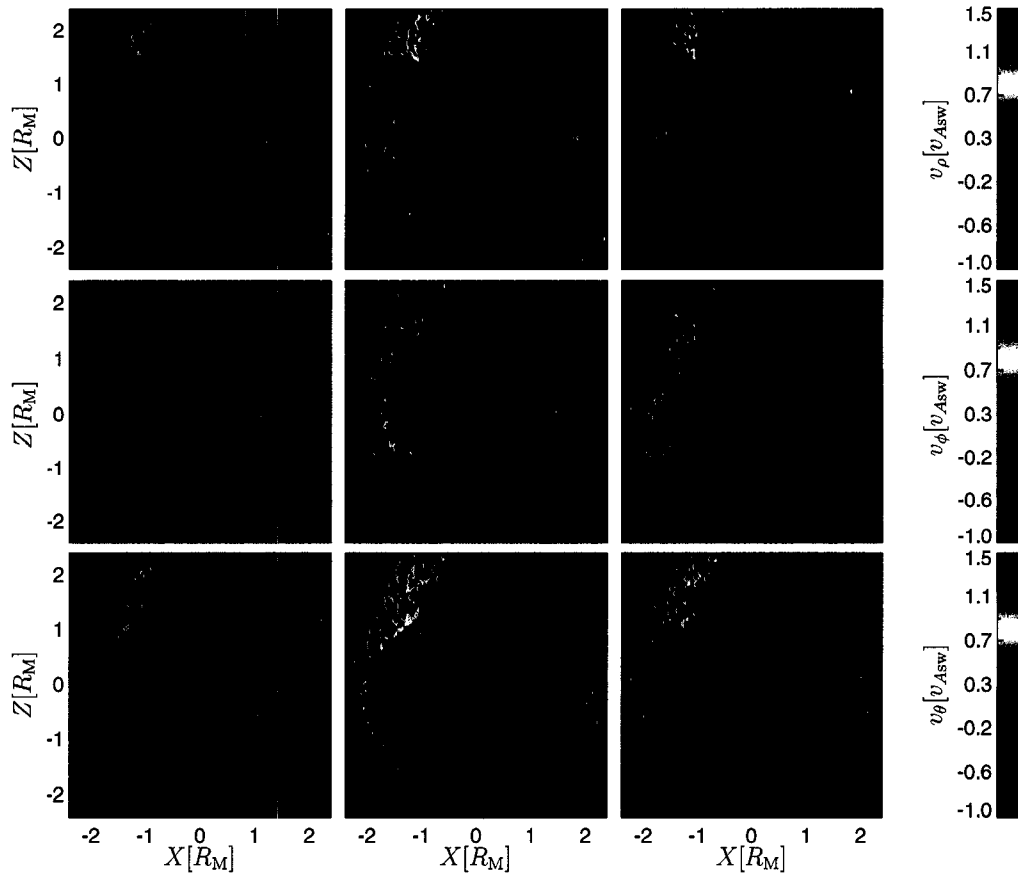


Figure 6.11: Bulk velocity, in plane forming an angle 60° with noon-midnight plane, in units of Alfvén speed of solar wind v_{Asw} for slow solar wind $v_{sw} = 3 v_{Asw}$. Three major releasing processes are presented in each column: photon stimulated desorption (PSD), solar wind sputtering (SWS) and micro-meteorite vaporization (MMV). The velocity is transformed into spherical coordinate system: radial direction (top row); longitudinal direction (middle row); and azimuthal direction (bottom row). The black line represents an assessment of magnetopause.

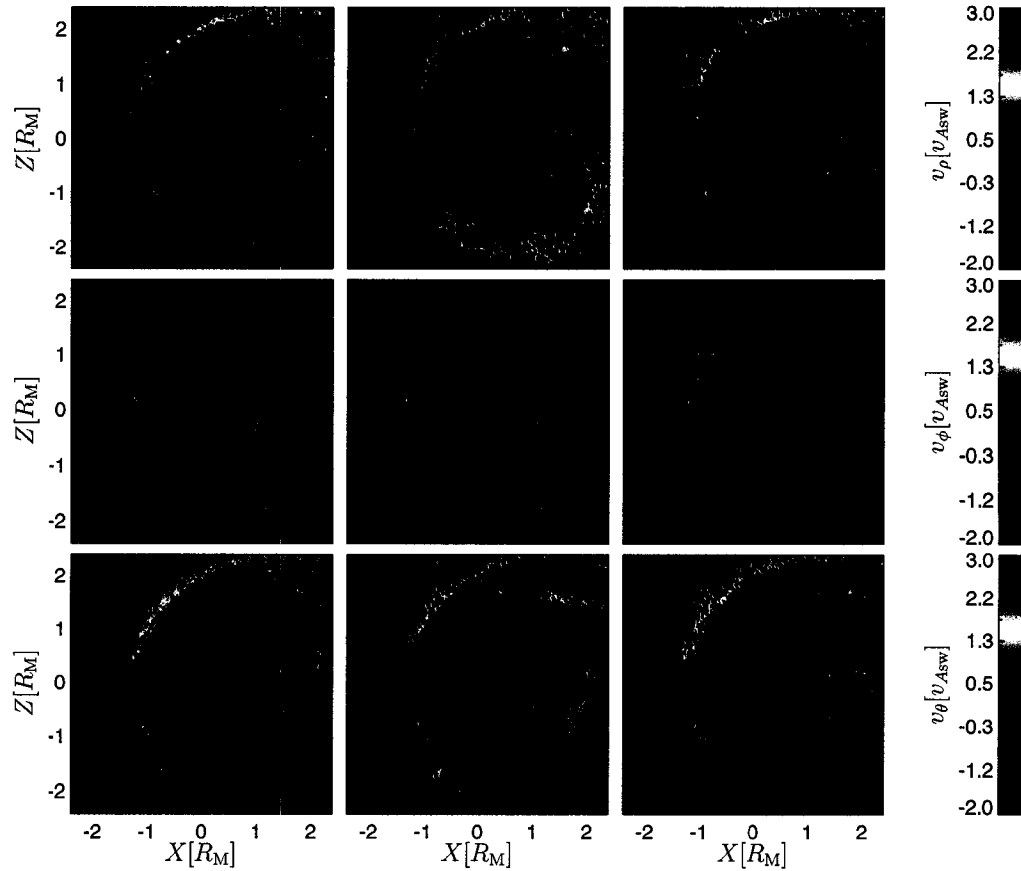


Figure 6.12: Bulk velocity, in plane forming an angle 60° with noon-midnight plane, in units of Alfvén speed of solar wind v_{Asw} for fast solar wind $v_{sw} = 5 v_{Asw}$. Three major releasing processes are presented in each column: photon stimulated desorption (PSD), solar wind sputtering (SWS) and micro-meteorite vaporization (MMV). The velocity is transformed into spherical coordinate system: radial direction (top row); longitudinal direction (middle row); and azimuthal direction (bottom row). The black line represents an assessment of magnetopause.

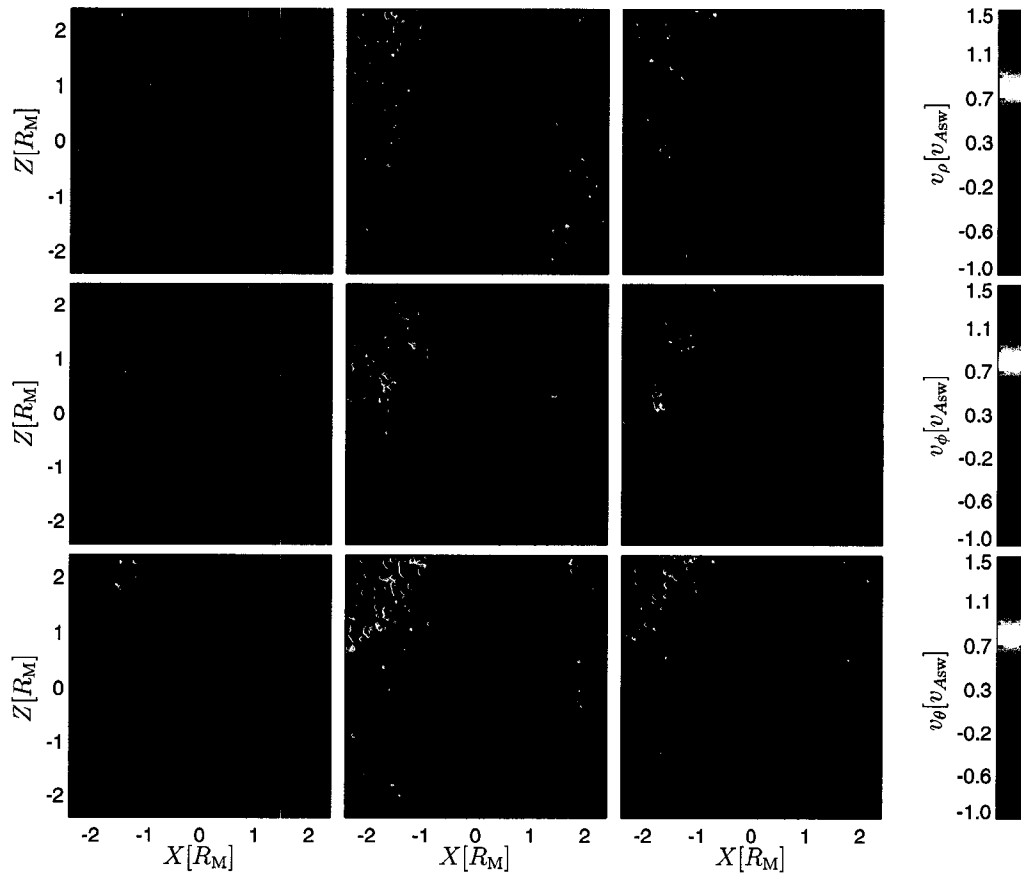


Figure 6.13: Bulk velocity in dawn-dusk plane in units of Alfvén speed of solar wind v_{Asw} for slow solar wind $v_{sw} = 3 v_{Asw}$. Three major releasing processes are presented in each column: photon stimulated desorption (PSD), solar wind sputtering (SWS) and micro-meteorite vaporization (MMV). The velocity is transformed into spherical coordinate system: radial direction (top row); longitudinal direction (middle row); and azimuthal direction (bottom row). The black line represents an assessment of magnetopause.

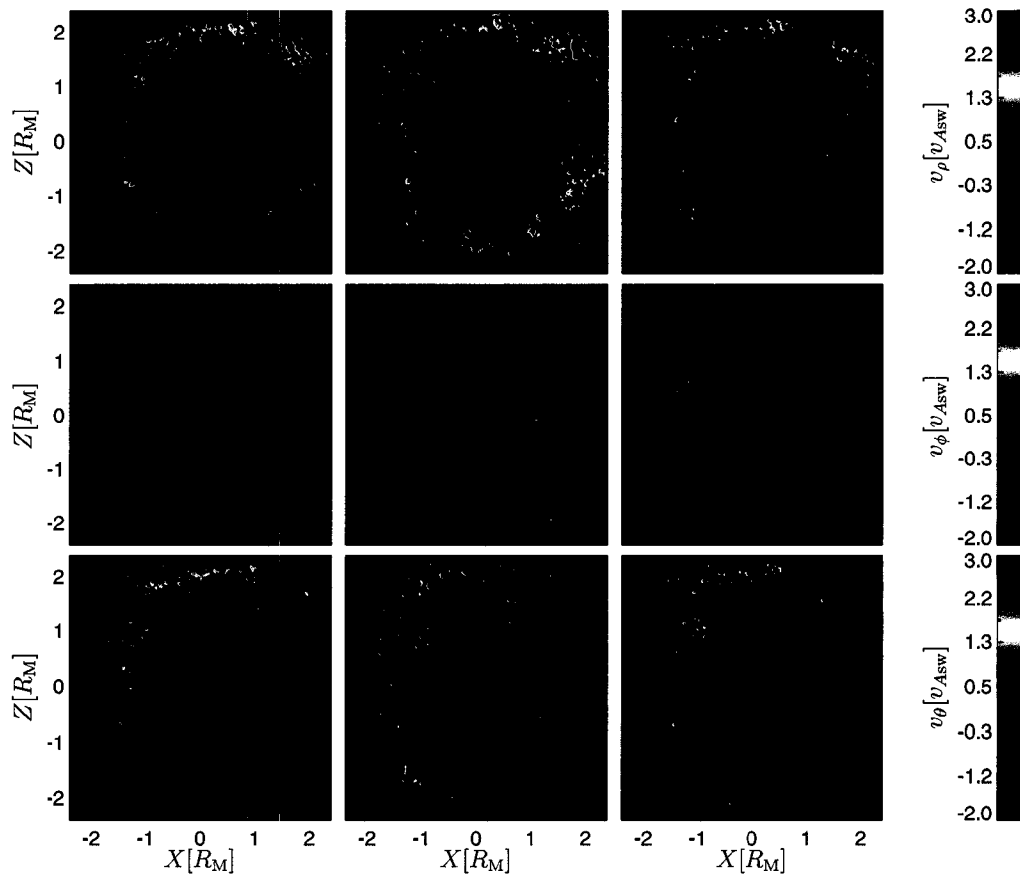


Figure 6.14: Bulk velocity in dawn-dusk plane in units of Alfvén speed of solar wind v_{Asw} for slow solar wind $v_{sw} = 5 v_{Asw}$. Three major releasing processes are presented in each column: photon stimulated desorption (PSD), solar wind sputtering (SWS) and micro-meteorite vaporization (MMV). The velocity is transformed into spherical coordinate system: radial direction (top row); longitudinal direction (middle row); and azimuthal direction (bottom row). The black line represents an assessment of magnetopause.

the fast solar wind case due to the strong gradients in magnetic field than that in slow solar wind where velocities reach about $1.5 v_{A\text{sw}}$. Comparing the radial direction of bulk velocity (top row) of the processes, we can note that only SWS mechanism shows an inward stream of ions towards the planet surface at south hemisphere in latitudes $50-70^\circ$, visible especially in Figure 6.9. We observed this feature in the mean energy flux through the surface in Section 6.4 as well. The inward flux is probably connected with increased velocity in negative azimuthal direction above the south pole, visible in Fig. 6.9 for SWS. In the real situation we will not be able to distinguish between the processes and thus we would see much higher flux of energetic particles in the north hemisphere compared to the south one where only the solar wind sputtering is contributing to the total flux from all processes.

In Sec. 6.3 we presented that one of the possible scenarios of ionized particle trajectory is to bounce between the north and south mirror points while undergo drifting motion causing the ring current. We can clearly identify a partial ring current especially in slow SW when magnetopause is sufficiently far from the surface. This increased bulk velocity is visible in longitudinal direction (middle row) of Figure 6.9.

The sodium plasma is almost stationary in both lobes and the only interesting regions are the high gradient structures in magnetic field. In the case of fast solar wind, sodium ions probably do not feel as strong magnetic field as in slow solar wind because spatial scales of EM field are much smaller than gyroradius of heavy sodium ions.

6.6 Temperature anisotropy

Figures 6.15 and 6.16 represent particle temperature anisotropy T_\perp/T_\parallel resulting from three major releasing processes, namely PSD, SWS and MMV (from top to bottom) in three planes of cut through the planet: Y-X, X-Z and Y-Z (from left to right). By future analyzing of parallel beta parameter $\beta_\parallel = 2\mu_0 p_\parallel / B^2$ defined as the ratio of thermal and magnetic pressure together with temperature anisotropy we can identify the sources of instabilities caused by sodium ion population. This analysis is out of scope of this thesis and will be done in future work.

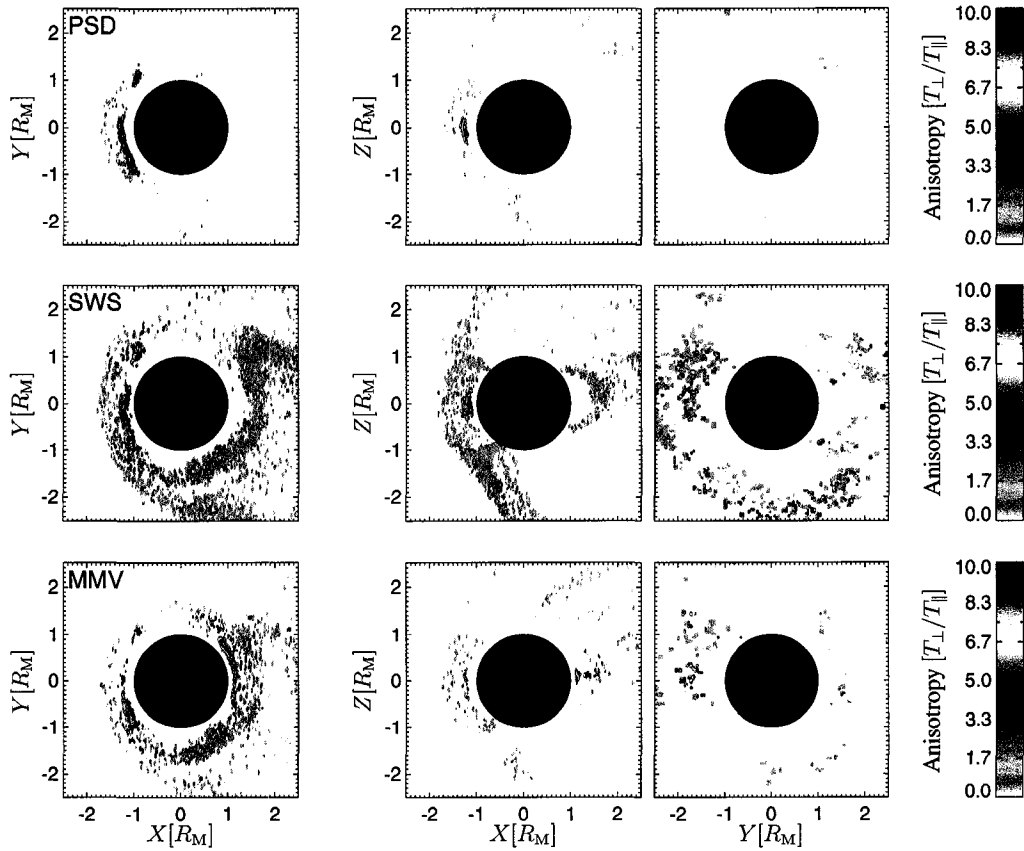


Figure 6.15: Temperature anisotropy T_{\perp}/T_{\parallel} in slow solar wind case from three major releasing processes: PSD, SWS, MMV (from top to bottom) in three different cuts through the center of the planet: X-Y, X-Z and Y-Z (from left to right).

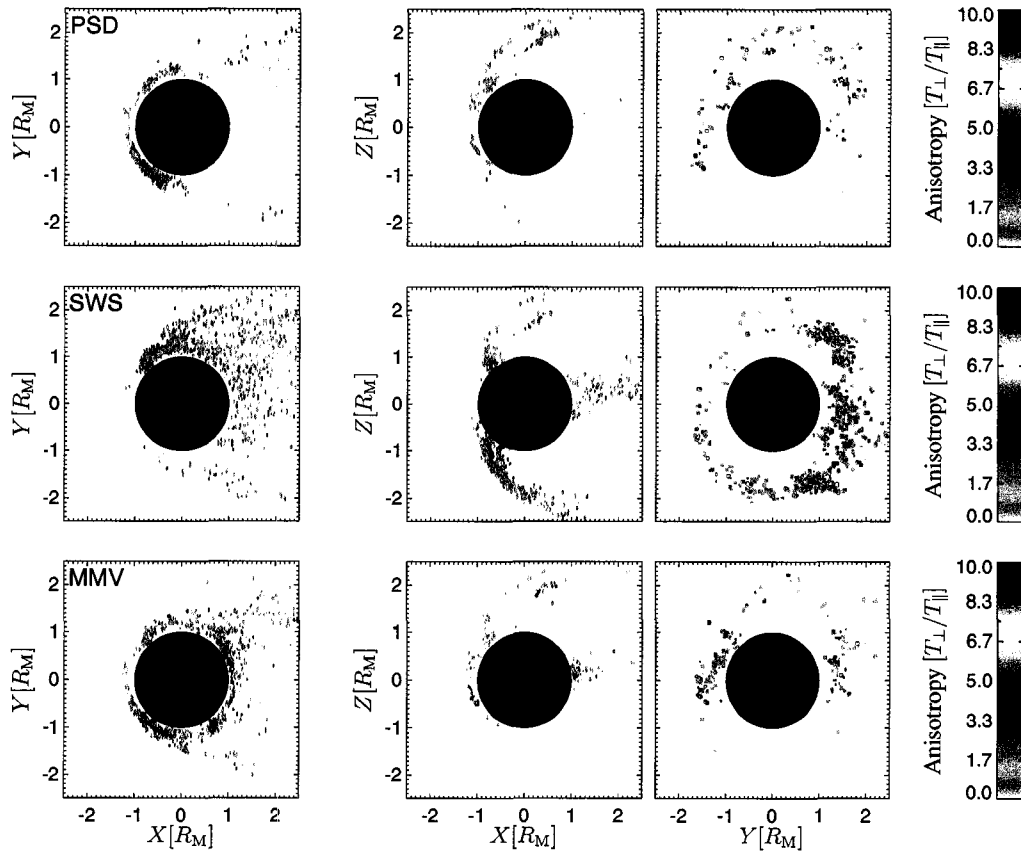


Figure 6.16: Temperature anisotropy T_{\perp}/T_{\parallel} in fast solar wind case from three major releasing processes: PSD, SWS, MMV (from top to bottom) in three different cuts through the center of the planet: X-Y, X-Z and Y-Z (from left to right).

6.7 Number density

In Figures 6.17 and 6.18 is non-thermal exosphere caused by particles which were ionized in very early time after the releasing. This envelope-like structure around the planet of non-accelerated particles is comparable with expectation and observations of *Killen et al.* [1998]. Both solar wind configuration possess a comet-like tail caused by photo-ionization process highlighted especially in SWS mechanism. This feature is due to the fact that photon flux can ionize neutral atoms only in the space with direct access of photons. Also note higher densities at high altitudes in subsolar point in case of SWS when compared with other releasing mechanisms. This enhancement is in an agreement with explanation of relationship between SWS and non-thermal exosphere at high altitudes by *Lammer and Bauer* [1997].

When a solar wind pressure is relatively small, as in the case of Figure 6.17, magnetosphere allow to sodium ions to develop exosphere with most of the aspects known from Earth. In the case of fast solar wind, presented in Figure 6.18, only the micro-meteorite vaporization and solar wind sputtering mechanisms had fully developed exosphere tails. Photo-stimulated desorption, on the other hand, had entire exosphere pressed towards the planet. This is mainly because of the spatial scales of magnetosheath between shock wave and magnetopause is much smaller that gyroradius of sodium ions. In this case particles hardly feel any forces at the boundaries and easily escape from the exosphere.

6.8 Mean energy

From the bulk velocity we can easily obtain the mean energy of the particle population. Two extreme cases of solar wind are considered: slow solar wind in Fig. 6.19 and fast solar wind in Fig. 6.20 separately for each of the releasing process. In top, middle and bottom row are PSD, SWS and MMV process respectively in three planes of cut: (from left to right) equatorial, noon-midnight and dawn-dusk plane. In all plates are three lines representing three flybys of MESSENGER mission (as of April 30, 2007) scheduled before parking the spacecraft on the orbit. As we can see from direct comparison of Fig. 6.19 and Fig. 6.20, fast solar wind ($5 v_{Asw}$) is able to energize the sodium population more then 10 times compared to the slow ($3 v_{Asw}$) SW. Only SWS and MMV

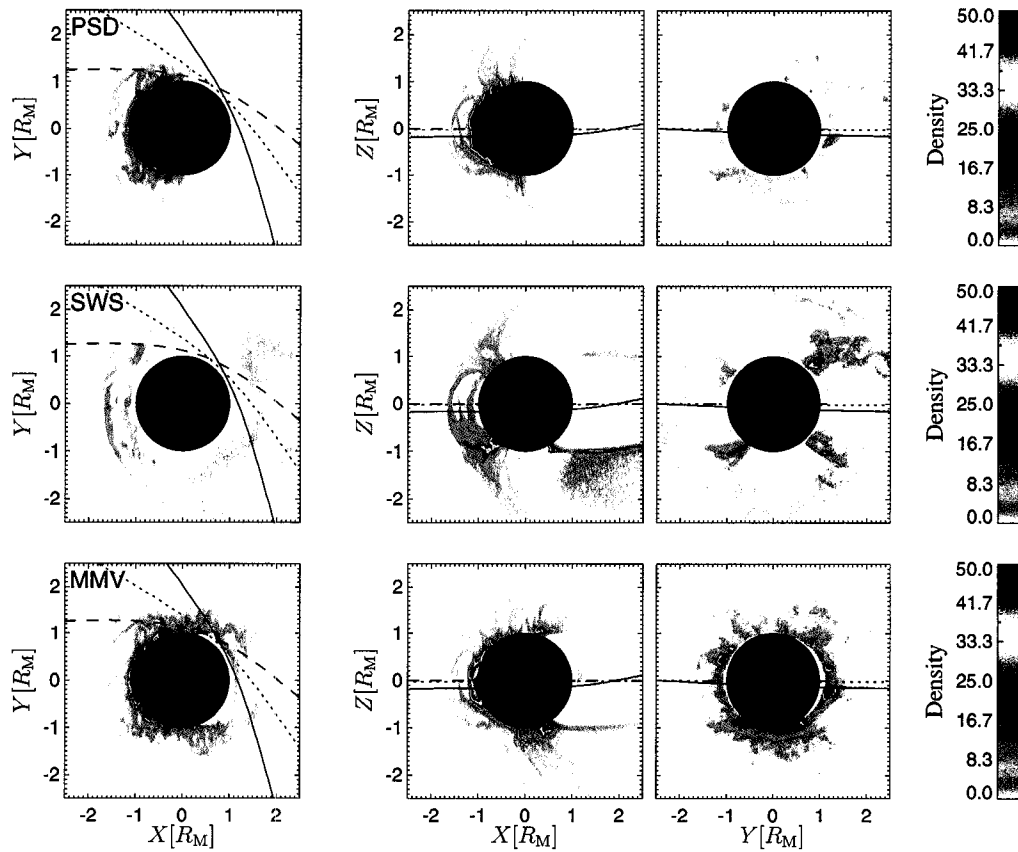


Figure 6.17: Super-particle number density in slow solar wind configuration of EM field of three major releasing processes: PSD, SWS, MMV (from top to bottom) in three different cuts through the center of the planet: X-Y, X-Z and Y-Z (from left to right). The three lines represents flybys of MESSENGER before parking on the orbit as of April 30, 2007.

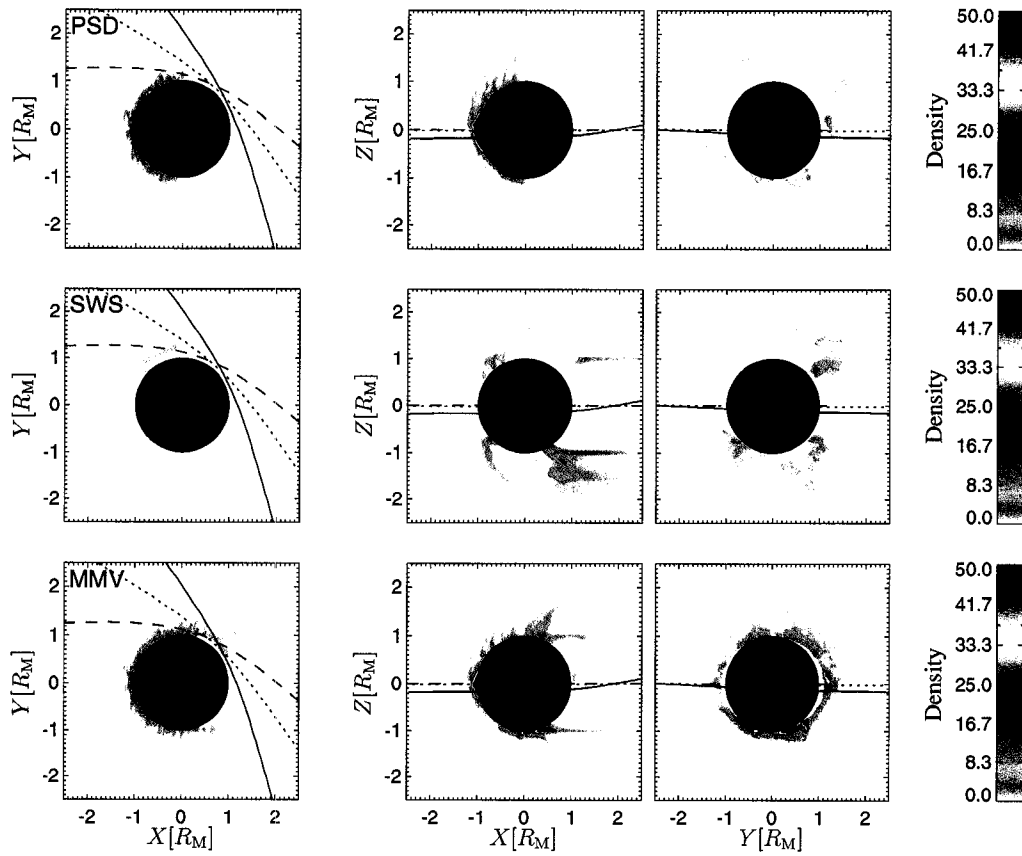


Figure 6.18: Super-particle number density in fast solar wind configuration of EM field of three major releasing processes: PSD, SWS, MMV (from top to bottom) in three different cuts through the center of the planet: X-Y, X-Z and Y-Z (from left to right). The three lines represents flybys of MESSENGER before parking on the orbit as of April 30, 2007.

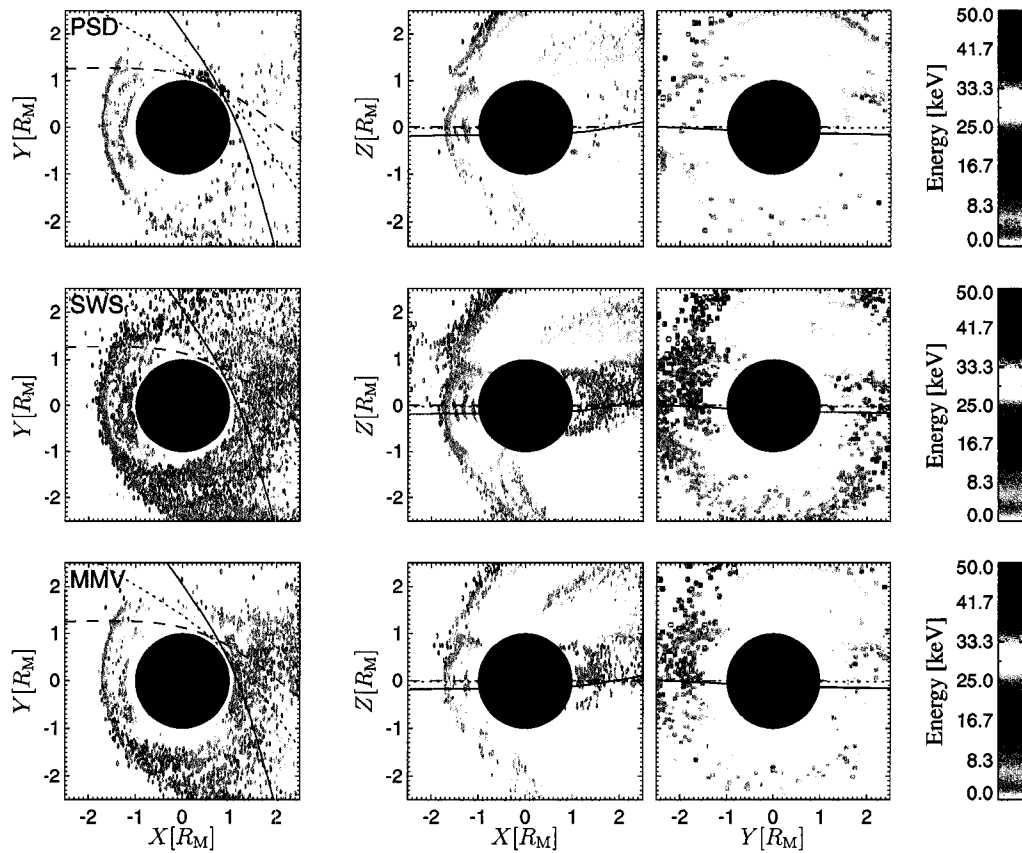


Figure 6.19: Mean energy of three major releasing processes: PSD, SWS, MMV (from top to bottom) in three different cuts through the center of the planet: X-Y, X-Z and Y-Z (from left to right). The three lines represents flybys of MESSENGER before parking on the orbit as of April 30, 2007.

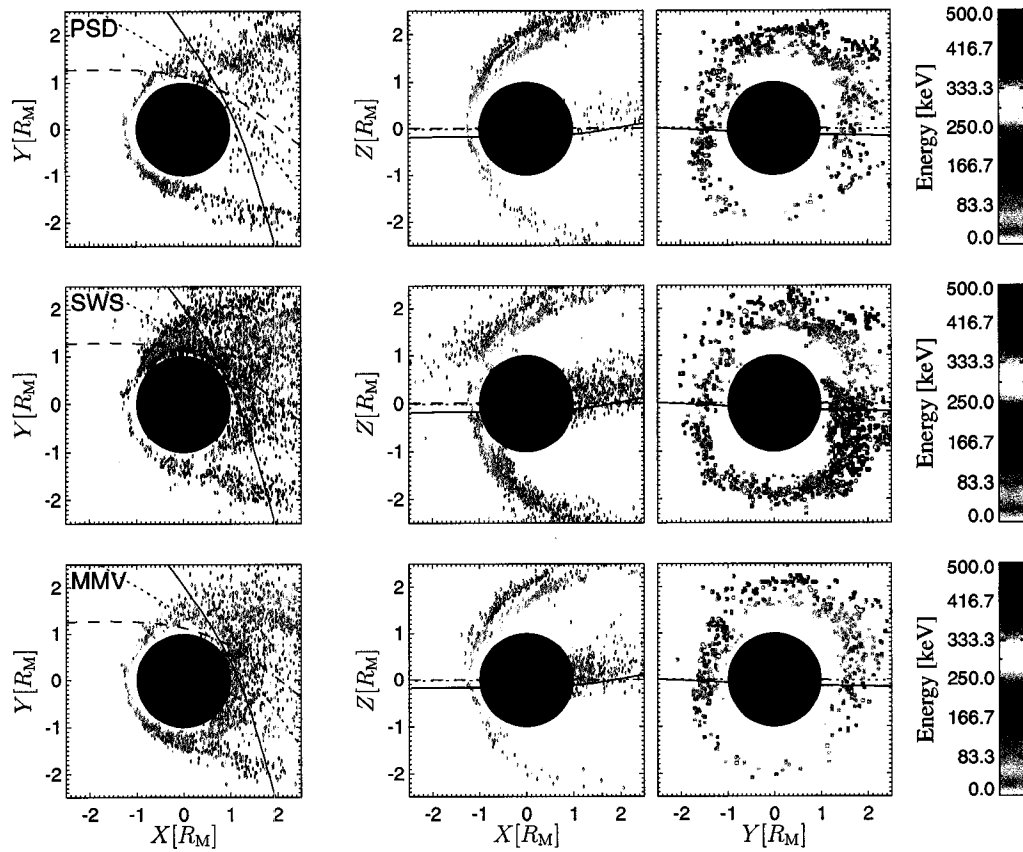


Figure 6.20: Mean energy of three major releasing processes: PSD, SWS, MMV (from top to bottom) in three different cuts through the center of the planet: X-Y, X-Z and Y-Z (from left to right). The three lines represents flybys of MESSENGER before parking on the orbit as of April 30, 2007.

processes are efficient enough to play an important role in populating current sheet region by energetic particles. Note the dusk-dawn asymmetry in energy population of MMV process especially visible in Fig. 6.19. This difference is due to the magnetosphere asymmetry and because of the transition time when particles from more dense dawn side move to the dusk side. During this transition particles gain energy in the interactions with fields. An energetic vacuum around the planet is visible only in case of slow solar wind (Fig. 6.19).

Two large structures formed in the distribution of high energy particles. Thick layer in equatorial plane continuing up to the tail around the current sheet and envelope-like structure upstream of magnetopause in magnetosheath. Particles in those regions gained energy from meandering motion in field with high gradient. Both structures are in agreement with *Delcourt et al.* [2003] who considered the same releasing processes as we did but used a simple empirical model of electromagnetic field. Using EM field from the hybrid simulation instead of empirical model leads to somewhat fuzzier distribution of energy but with still clearly visible structures.

6.9 Virtual flybys of MESSENGER

On Figure 6.21 is density distribution in units of solar wind density n_{psw} in three planes with scheduled flybys (as of April 30, 2007) of MESSENGER mission described in Section 2.2. The flybys are scheduled on FB1: 2008/01/14 (solid line), FB2: 2008/10/06 (dotted line) and FB3: 2009/09/29 (dashed line). Note that all three flybys are at the equatorial plane. One of the key component of the mission will be FIPS instrument developed by University of Michigan described in *Koehn et al.* [2002]. The objectives of the instrument are to measure energy and species of charged particles in both low and high energy spectrum. Low energy spectrum channel should map the exosphere formed from released particles from the surface and high energy channel should answer the questions about energizing processes taking place in Mercury's magnetosphere.

Since the initial particle number densities are unknown for all releasing process, not many conclusions can be made from the sodium number densities measured during the flybys. Fig. 6.22 represents macro-particle number density measured during three flybys of MESSENGER around Mercury before parking the spacecraft at the orbit of the planet. First three plates are under slow SW conditions and bottom three are during fast SW. Various lines represent

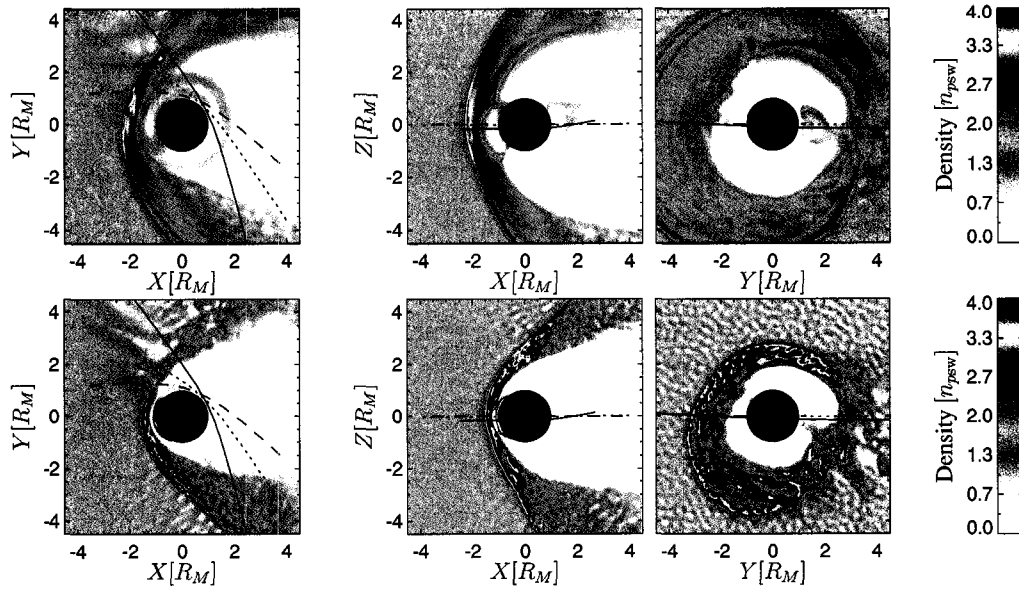


Figure 6.21: Virtual flybys of MESSENGER scheduled for 2008/01/14 (solid line) 2008/10/06 (dotted line) and 2009/09/29 (dashed line) on the background of solar wind proton number density for slow (top) and fast (bottom) case of solar wind

different processes: solid line - photon stimulated desorption, dotted line - solar wind sputtering and dashed line - micro-meteorite vaporization.

In Fig. 6.22 micro-meteorite vaporization process dominates (dashed line) except of the third flyby in slow solar wind (third plate) where trajectory of the spacecraft cross the thin layer of high density sodium ions on the dayside formed by photon stimulated desorption (solid line). In this case the peak at $t = 6$ min has the same structure and amplitude for both MMV and PSD. From Fig. 6.22 we can see that under the conditions when all releasing process would have the same particle flux from the entire surface, micro-meteorite vaporization would be the dominant process populating dawn side of the planet. This is because of the distribution flux of sodium atoms on the surface from MMV process is two times higher on the dawn than on the dusk side. Compared to the third flyby during the slow solar wind, the peak observed as well in the fast solar wind in PSD process (bottom plate) at $t = 3$ min is much smaller, compared to the peak in MMV, although still visible. Both cases, presented here, show the increased density in the interval between 3 and 5 minutes of the flyby which is connected with comet-like tail due to the photo-ionization process which acts only on the

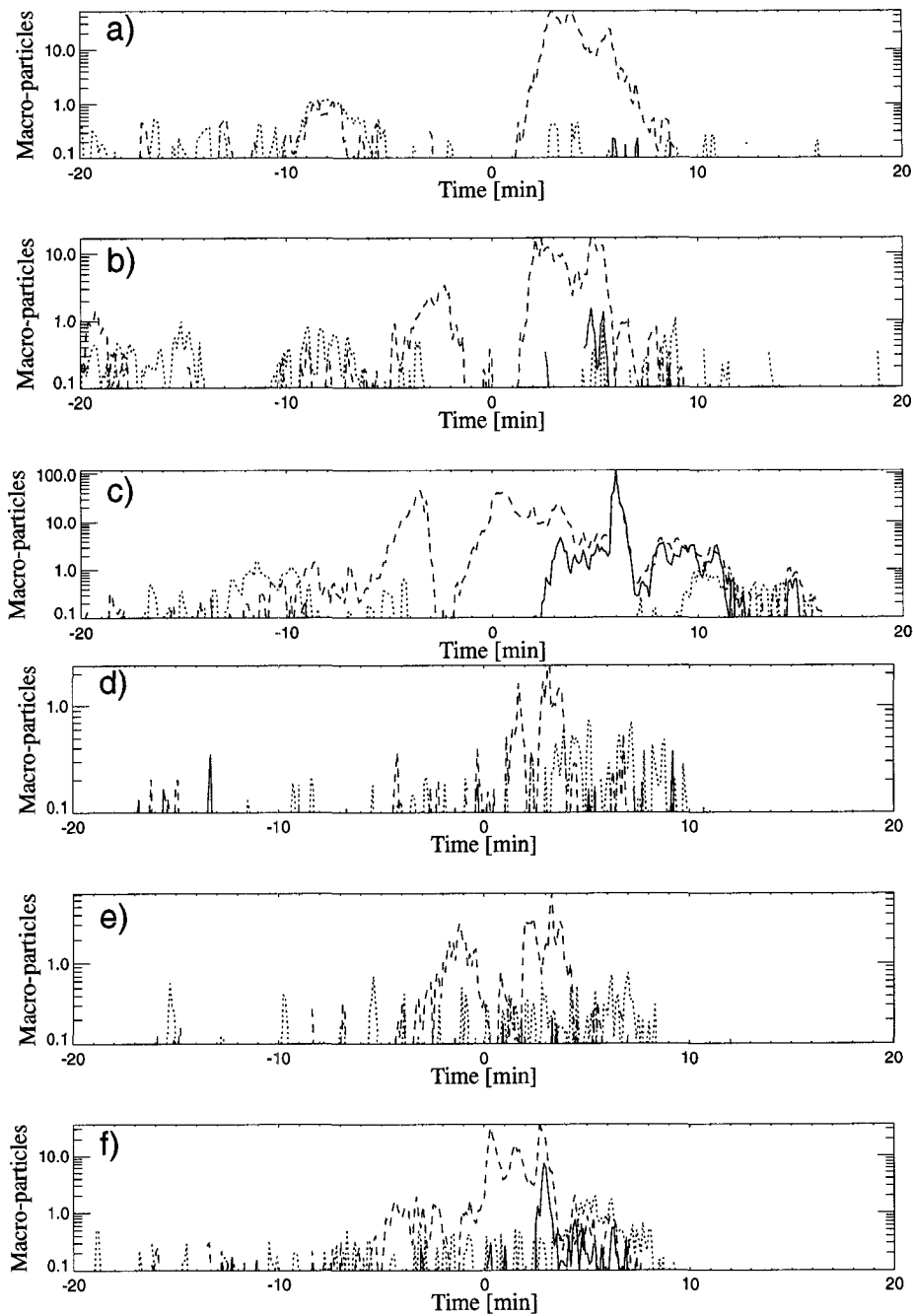


Figure 6.22: Macro-particle number density during three virtual flybys of MESSENGER in the vicinity of the planet for slow (top 3 panels) and fast (bottom 3 panels) solar wind. Solid line, dotted line and dashed line represents PSD, SWS and MMV processes respectively. Time $t = 0$ represents the closest approach.

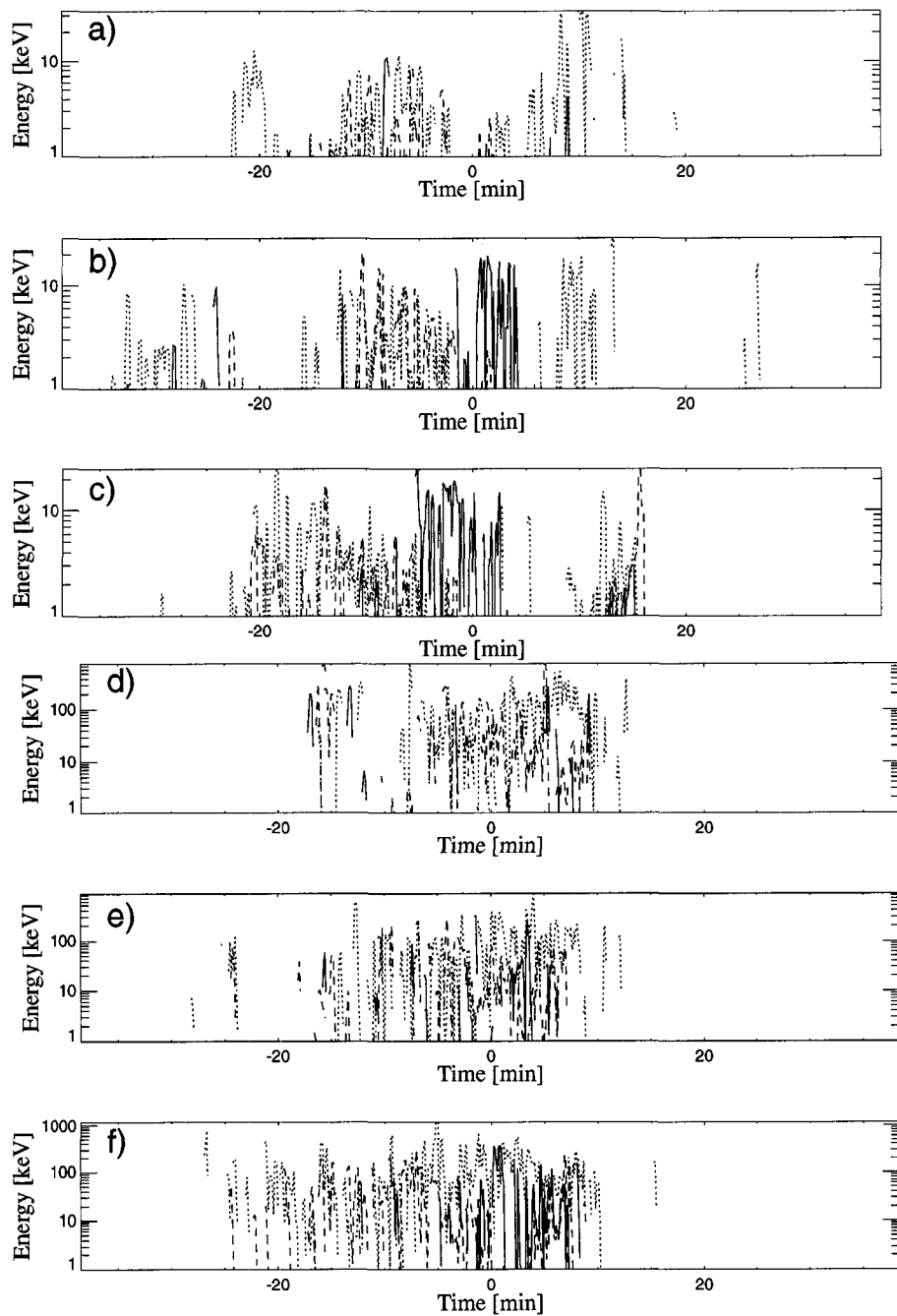


Figure 6.23: Sodium mean energy during three virtual flybys of MESSENGER in the vicinity of the planet for slow (top 3 panels) and fast (bottom 3 panels) solar wind. Solid line, dotted line and dashed line represents PSD, SWS and MMV processes respectively. Time $t = 0$ represents the closest approach.

dayside and in the regions with direct access of the photon flux.

From the bulk velocity we can easily obtain mean energy of the sodium ions. Compared to the number density, which is unknown because of the uncertain or unknown initial particle fluxes from the surface, mean energy of particle distribution is independent of the initial sodium number density. In the case of sufficiently high number density, when collisions are not negligible, we would need to take into account another process of energy distribution. Since almost no collisions take place in the sodium exosphere, this is not the case. In Figure 6.23 are several plots of the mean energy measured during the virtual flybys of MESSENGER under the various solar wind conditions. Top three plates represent slow SW and bottom three demonstrate fast SW conditions. Time $t = 0$ minutes represents the closest approach of the spacecraft from the planet's surface which is, from the last trajectory adjustments, supposed to be ≈ 200 km. From the measurement of super-particle density during the flybys we can estimate spatial regions where the distribution function of ion population is described sufficiently and where statistical error is large. In the regions where super-particle density is lower than the critical density we do not have enough information about the sodium plasma and the energy measurements are not convincing at the given region. To avoid this phenomenon we would need to increase the amount of super-particles or decrease the spatial resolution.

From energies of PSD process (solid line) we can see increasing importance the PSD plays in generation of energetic particles population (around $t = 0$ minutes) as the closest approach of the flyby shifts from night sector towards dawn. Although such feature is visible only for slow solar wind because when exosphere is compressed towards the surface most of the particles return back to the surface or simply escape from the system. Thus there is no energy increase from PSD process around $t = 0$ min for bottom three plates representing the fast solar wind study case. The MMV process (dashed line) acts as a background, middle range energy source except of the several events where energy increased up to maximal 8×10^5 in the plate 6.23d. Almost no long term enhance in energy is observed during the flybys caused by MMV. This process greatly is responsible in populating night side and tail regions. On the other hand SWS process (dotted line) is even more very effective in populating night sector. Especially for fast solar wind (bottom three panels) the SWS is dominating process for times < 5 min which represents sector from terminator down to the tail region in the equatorial plane. Considering that particles are released from

the midlatitude region of the planet, particles are easily trapped and participate in the ring current and thus are transported into the tail where escape.

We found that in our simulation the pick-up ions were accelerated to the energies of up to 10^6 eV, which is well within the range of measuring capabilities of the FIPS instrument on board the MESSENGER spacecraft *Koehn et al.* [2002]. Our simulations show that the energy spectrum of the heavy ions along the proposed MESSENGER flyby trajectories is strongly affected by the solar wind dynamic pressure. Depending on the assumed solar wind conditions, the typical ion energies may change by a factor of 10 or even more. Two major structures formed in distribution of relatively high energy sodium ions. First, thick layer at the current sheet region and second in the upstream of magnetopause. Both regions are connected with the increased magnetic field gradient causing the acceleration of particles. Note also the higher mean energy in the upstream of dawn sector. This enhancement is due to the Parker spiral orientation of IMF which forms the parallel bow shock easily penetrated by ions. These results are qualitatively similar to those of [*Delcourt et al.*, 2003] who used an empirical magnetic field model to describe Mercury's magnetosphere. Sharp peaks in the high-energy ion concentrations near the magnetospheric boundaries in our model is also reminiscent of the energetic particle peaks observed by Mariner 10 spacecraft [*Simpson et al.*, 1974b] (even if the details of the interpretation of observations are still open to debate). The locations of the high concentrations of the high-energy particles depend on the magnetic field topology. Therefore, FIPS measurements can be used to provide additional constrains on the magnetospheric magnetic field in the Hermean magnetosphere. Energy spectrum measured by FIPS will also provide answers with respect to the acceleration mechanism for the pick up ions in the magnetosphere of Mercury.

From analysis of gradient and local curvature of magnetic field we can see that curvature plays very important role in acceleration of particles, especially in very low latitude regions and within $1.3 R_M$ of radii. Whilst gradient of magnetic field is more important in a tail region and in bow shock crossing of ions. Analysing of energy distribution and the bulk velocity of heavy ions from MESSENGER spacecraft measurements it will be possible to locate those regions of interest and confirm our findings.

Chapter 7

Conclusions

Our work was focused on sodium ion exosphere generated from the surface of planet Mercury using various releasing processes of sodium neutral atoms. From the known processes we considered three major releasing mechanisms: photon stimulated desorption caused by flux of the energetic photons from the Sun (with energies > 5 eV); solar wind sputtering due to the high energetic protons which impacted the surface after penetrating magnetosphere; and micro-meteorite vaporization caused by space material bombarding surface. The other processes were not taken into account due to the small role they play in the forming of exosphere. Among those is, for example, thermal desorption which produces only low energy particle with insufficient velocity to overcome the gravitation and solar wind pressure forces. Because we neglected collisions in our system, all releasing processes behave independently and we were able to study distributions, temperatures and other characteristics separately for each of the releasing mechanisms. Due to the increasing interest in planet Mercury initiated by space mission Mariner 10 in 1974/1975 and followed by two new missions: i) MESSENGER in collaboration of National Aeronautics and Space Administration (NASA) and The John Hopkins University Applied Physics Laboratory (APL); ii) BepiColombo developed in collaboration of European Space Agency (ESA) and Japan Aerospace Exploration Agency (JAXA) we simulated sodium atoms ionized through photoionization process to obtain sodium exosphere which will be the subject of those missions.

We performed several statistics with number of particles in the system which leave the simulation box through the boundary (N_{bnd}), hit the surface of the planet (N_{pl}). In agreement with *Ip* [1987], who estimated the ratio N_{bnd}/N_{pl} to

be 0.5, we obtain $\approx 40\%$ in case of the fast solar wind. Although this ratio is uncertain because we expected that all releasing processes have the same flux of the particles through surface. In case when one of the process would dominate then this ratio could change dramatically. This can happen, for example, in the case of coronal mass ejection when solar wind protons are very energetic. The number of particles which scatter back to the surface is between 24% and 35% from total number of released atoms, except of PSD process under the fast solar wind condition where this number is $\approx 48\%$.

From the measurements of the energy flux through the planetary surface we can see that most of the energetic particles are scattered at latitude $< 50^\circ$ which is the open/closed field line boundary. For slow solar wind $3v_{Asw}$, only two narrow ($\approx 10^\circ$) energetic bands are formed and as the speed of the solar wind increase up to $5v_{Asw}$, energy flux increase even in the lower latitudes. In agreement with *Delcourt et al.* [2003] there is a shift of the bands on the day side of the planet towards the equator of about 5° . We identified two major scattering processes: i) when the pitch angle of particle is less then critical angle, the particle escape from the magnetic mirror and scatter on the surface; ii) neutral atoms which after ionization and usually have very complicated history in the simulation box are energized in the tail or from cross-polar centrifugal acceleration and then injected back into the upstream of the magnetopause. Such particles can enter the inner magnetosphere through open/closed field line boundary. Note also that for such accelerated population we can identify only above the north pole except of the solar wind sputtering process, for example in Figures 6.9 and 6.10, where we can identify the flux in azimuthal direction of energetic particles even in south hemisphere. This observation is in agreement with Figure 6.6 of the energy flux where only SWS has energetic bands at latitude $30 - 50^\circ$ on both hemispheres and all longitudes. Compared to the initial velocities of the particles being about $0.01v_{Asw}$ when released from the surface, we obtain bulk velocities up to $1.5v_{Asw}$ in slow solar wind and more then $3v_{Asw}$ in the case of fast SW.

From Figure 6.1 we can see that gradient pressure responsible for higher electric field in magnetosheath will cause higher $\mathbf{E} \times \mathbf{B}$ electric drift which supports injection of particles, already accelerated mainly in current sheet region, into the midlatitude regions of the planet observed in all figures of energy flux through planet's surface, namely Figure 6.6 and 6.8. Particles are easily injected into the inner magnetosphere in open/closed field boundary as seen in

solar wind protons flux through surface. Such accelerated particles will cause secondary sputtering in the case of sufficient amount of material in the upper crust of the planet. In the case of the fast material depletion, for example by thermal desorption as proposed by *Hunten and Sprague* [2002], this secondary sputtering would be inefficient due to the lack of the material in upper crust of the planet.

In agreement with the expectations for FIPS [*Koehn et al.*, 2002] installed on board of MESSENGER spacecraft, we obtained the same maximal energies with values up to 10^6 eV during the virtual flybys performed on obtained data from numerical simulations. No releasing processes dominates during the flyby but this fact could change when different trajectories (i.e. though dayside of the planet) would be considered. Note, that mean energies differ with change of the solar wind pressure and can be 10-20 times higher. Also, only two characteristic structures formed in the distribution of high energy particles. Firstly, thick layer ($\approx 1R_M$) formed around the current sheet. Secondly, envelope-like structure in the magnetosheath. Those two regions are in agreement with [*Delcourt et al.*, 2003] who considered the same releasing processes but mathematical model of magnetosphere.

As part of future work we would like to investigate different orientation of interplanetary magnetic field which may play an important role in forming topology of magnetosphere and this influence mainly solar wind sputtering process caused by energetic protons penetrating to the surface. Another part of the future work could focus on the neutral exosphere formed from the neutral atoms before ionization. For this purpose we would need to implement forces such as gravitation and solar wind acceleration pressure. Then we could employ the line of sight integration technique to compare the results with ground based observations. In future, various species (like K^+) can be considered when first result from MESSENGER mission will be available. Future analysis of beta parameter β_{\parallel} together with temperature anisotropy could reveal sources of instabilities caused by sodium ions.

Bibliography

Andrews, G. B., T. H. Zurbuchen, B. H. Mauk, H. Malcom, L. A. Fisk, G. Gloeckler, G. C. Ho, J. S. Kelley, P. L. Koehn, T. W. LeFevere, S. S. Livi, R. A. Lundgren, and J. M. Raines, The energetic particle and plasma spectrometer instrument on the MESSENGER spacecraft, *Space Sc. Rev.*, p. in press, 2007.

Anselmi, A., and G. E. N. Scoon, BepiColombo, ESA's Mercury Cornerstone mission, *Plan. Space Sci.*, *49*, 1409–1420, 2001.

Armstrong, T. P., S. M. Krimigis, and L. J. Lanzerotti, A reinterpretation of the reported energetic particle fluxes in the vicinity of Mercury, *J. Geophys. Res.*, *80*, 4015–4017, 1975.

Baumjohann, W., and R. A. Treumann, *Basic Space Plasma Physics*, Imperial College Press, London, 1996.

Bida, T. A., R. M. Killen, and T. H. Morgan, Discovery of calcium in Mercury's atmosphere, *Nature*, *404*, 159–161, 2000.

Broadfoot, A. L., D. E. Shemansky, and S. Kumar, Mariner 10: Mercury atmosphere, *Geophys. Res. Lett.*, *3*, 577–580, 1976a.

Broadfoot, A. L., D. E. Shemansky, and S. Kumar, Mariner 10: Mercury Atmosphere, *Geophys. Res. Lett.*, *3*, 577–580, 1976b, cameron Library: QC 801 G347 v.3 1976.

Christon, S., S. Daly, J. Eraker, M. Perkins, J. Simpson, and A. Tuzzolino, Electron calibration of instrumentation for low energy, high intensity particle measurements at Mercury, *J. Geophys. Res.*, *84*, 4277–4288, 1979.

Connerney, J. E. P., and N. F. Ness, *Mercury's magnetic field and its interior*, The University of Arizona press, 1988.

- Criston, S. P., S. F. Daly, J. H. Eraker, M. A. Perkins, J. A. Simpson, and A. J. Tuzolino, Electron calibration of instrumentation for Low Energy, High Intensity, Particle measurements at Mercury, *J. Geophys. Res.*, *84*, 4277–4288, 1979.
- Delcourt, D. C., S. Grimald, F. Leblanc, J.-J. Berthelier, A. Millilo, A. Mura, S. Orsini, and T. E. Moore, A quantitative model of the planetary Na⁺ contribution to Mercury's magnetosphere, *Ann. Geophys.*, *21*, 1723–1736, 2003.
- Eraker, J. H., and J. A. Simpson, Acceleration of charged particles in Mercury's magnetosphere, *J. Geophys. Res.*, *91*, 9973–9993, 1986.
- Gold, R. E., S. C. Solomon, R. L. McNutt, A. G. Santo, J. B. Abshire, M. H. Acuna, R. S. Afzal, B. J. Anderson, G. B. Andrews, P. D. Bedini, J. Cain, A. F. Cheng, L. G. Evans, W. C. Feldman, R. B. Follas, G. Gloeckler, J. O. Goldsten, S. E. Hawkins, N. R. Izenberg, S. E. Jaskulek, E. A. Ketchum, M. R. Lankton, D. A. Lohr, B. H. Mauk, W. E. McClintock, S. L. Murchie, C. E. Schlemm, D. E. Smith, R. D. Starr, and T. H. Zurbuchen, The MESSENGER mission to Mercury: scientific payload, *Plan. Space Sci.*, *49*, 1467–1479, 2001.
- Harmon, J., and M. Slade, Radar mapping of Mercury: full-disk images and polar anomalies, *Science*, *258*, 640–642, 1992.
- Harned, D. S., Quasineutral hybrid simulation of macroscopic plasma phenomena, *J. Comput. Phys.*, *47*, 452–462, 1982.
- Hodges, R. R. J., Model atmospheres for Mercury based on lunar analogy, *J. Geophys. Res.*, pp. 2881–2285, 1974.
- Horowitz, E. J., D. E. Shumaker, and D. V. Anderson, QN3D: A three-dimensional quasi-neutral hybrid particle-in-cell code with applications to the tilt mode instability in field reversed configurations, *J. Comput. Phys.*, *84*, 279–310, 1989.
- Hunten, D. M., The escape of light gases from planetary atmospheres, *jas*, *30*, 1481–1494, 1973.
- Hunten, D. M., and A. L. Sprague, Origin and character of the lunar and mercurian term atmospheres, *J. Geophys. Res.*, *19*, 1551–1560, 1997.

- Hunten, D. M., and A. L. Sprague, Diurnal variation of Na and K at Mercury, *Meteor. Planet. Sci.*, *37*, 1191–1195, 2002.
- Hunten, D. M., T. H. Morgan, and D. E. Shemansky, The Mercury atmosphere, pp. 562–612, 1988.
- Ip, W. H., Dynamics of electrons and heavy ions in Mercury's magnetosphere, *Icarus*, *71*, 441–447, 1987.
- Johnson, R. E., and R. Baragiola, Lunar surface: Sputtering and secondary ion mass spectrometry, *Geophys. Res. Lett.*, *18*, 2169–2172, 1991.
- Kabin, K., T. I. Gombosi, D. L. DeZeeuw, and K. G. Powell, Interaction of Mercury with Solar Wind, *Icarus*, *143*, 397–406, 1999.
- Kabin, K., M. H. Heimpel, R. Rankin, J. M. Aurnou, N. Gomez-Perez, J. Paral, T. I. Gombosi, T. H. Zurbuchen, P. L. Koehn, and D. L. DeZeeuw, Global MHD modeling of Mercury's magnetosphere with applications to the MESSENGER mission and dynamo theory, *Icarus*, 2007.
- Killen, R. M., and W. H. Ip, The surface-bounded atmospheres of Mercury and the Moon, *Rev. Geophys.*, *37*, 361–406, 1999.
- Killen, R. M., and T. H. Morgan, Maintaining the Na Atmosphere of Mercury, *Icarus*, *101*, 293–312, 1993a.
- Killen, R. M., and T. H. Morgan, Diffusion of Na and K in the uppermost regolith of Mercury, *J. Geophys. Res.*, *98*, 23, 589–23, 601, 1993b.
- Killen, R. M., A. E. Potter, and T. H. Morgan, Spatial distribution of sodium vapor in the atmosphere of Mercury, *Icarus*, *85*, 145–167, 1990.
- Killen, R. M., A. E. Potter, and T. H. Morgan, Velocity structure in Mercury's exosphere, *Bull. Am. Astron. Soc.*, *987*, 29(3), 1997.
- Killen, R. M., A. E. Potter, A. Fitzsimmons, and T. H. Morgan, Evidence for a non-thermal corona about Mercury, *Bull. Am. Astron. Soc.*, *30*, 1998.
- Killen, R. M., A. E. Potter, P. Reiff, M. Sarantos, B. V. Jackson, P. Hick, and B. Giles, Evidence for space weather at Mercury, *J. Geophys. Res.*, *106*, 20, 509–20, 526, 2001.

- Knuth, D. E., *The Art of Computer Programming*, Addison Wesley, 1973.
- Koehn, P. L., and A. L. Sprague, Solar oxygen and calcium in Mercury's exosphere, *Plan. Space Sci.*, p. in press, 2007.
- Koehn, P. L., T. H. Zurbuchen, G. Gloeckler, R. A. Lundgren, and L. A. Fisk, Measuring the plasma environment at Mercury: The fast imaging plasma spectrometer, *Meteor. Planet. Sci.*, *37*, 1173–1189, 2002.
- Lammer, H., and S. J. Bauer, Mercury's exosphere: origin of surface sputtering and implications, *Plan. Space Sci.*, *45*, 73–79, 1997.
- Lammer, H., P. Wurz, M. R. Patel, R. Killen, C. Kolb, S. Massetti, S. Orsini, and A. Milillo, The variability of mercury's exosphere by particle and radiation induced surface release processes, *Icarus*, *166*, 238–247, 2003.
- Leblanc, F., and R. E. Johnson, Mercury's sodium exosphere, *Icarus*, *164*, 261–281, 2003.
- Lipatov, A. S., *The Hybrid Multiscale Simulation Technology: an introduction with application to astrophysical and laboratory plasmas*, Springer, 2002.
- Luhmann, J. G., C. T. Russell, and N. A. Tsyganenko, Disturbances in Mercury's magnetosphere: Are the Mariner 10 substorms simply driven?, *J. Geophys. Res.*, *103*, 9113–9120, 1998.
- Lundin, R., S. Barabash, P. Brandt, L. Eliasson, C. M. C. Nairn, O. Norberg, and I. Sandahl, Ion acceleration processes in the Hermean and terrestrial magnetospheres, *Adv. Space Res.*, *19*, 1593–1607, 1997.
- Madey, T. E., B. V. Yakshinskiy, V. N. Ageev, and R. E. Johnson, Desorption of alkali atoms and ions from oxide surfaces: Relevance to origins of Na and K in atmospheres of Mercury and the Moon, *J. Geophys. Res.*, *103*, 5873–5888, 1998.
- Matthews, A., Current advance method and cyclic leapfrog for 2D multispecies hybrid plasma simulations, *J. Comput. Phys.*, *112*, 102–116, 1994.
- McGrath, M. A., R. E. Johnson, and L. J. Lanzerotti, Sputtering of sodium on the planet Mercury, *Nature*, *323*, 694–696, 1986.

- McKenna-Lawlor, S. M. P., Characteristic boundaries of the hermean magnetosphere and energetic particles close to the planet, *Plan. Space Sci.*, *45*, 167–180, 1997.
- Milillo, A., S. Orsini, D. Delcourt, E. Kallio, R. Killen, H. Lammer, F. Leblanc, S. Massetti, A. Mura, P. Wurz, S. Barabash, G. Cremonese, I. Daglis, E. D. Angelis, A. M. D. Lellis, S. Livi, and V. Mangano, Surface-exosphere-magnetosphere system of Mercury, *Space Sc. Rev.*, *117*, 397–443, 2005.
- Morgan, T. H., and R. M. Killen, A non-stoichiometric model of the composition of the atmospheres of Mercury and the Moon, *Plan. Space Sci.*, *45*, 81–83, 1997.
- Morgan, T. H., H. A. Zook, and A. E. Potter, Impact-driven supply of sodium and potassium to the atmosphere of Mercury, *Icarus*, *75*, 156–170, 1988.
- Ness, N., K. Behannon, R. Lepping, Y. Whang, and K. Schatten, Magnetic field observations near Venus: preliminary results from Mariner 10, *Science*, *183*, 1301–1306, 1974a.
- Ness, N., K. Behannon, R. Lepping, Y. Whang, and K. Schatten, Magnetic field observations near Mercury: preliminary results from Mariner 10, *Science*, *185*, 151–160, 1974b.
- Ness, N. F., K. W. Behannon, R. P. Lepping, and Y. C. Whang, The magnetic field of Mercury, *J. Geophys. Res.*, *80*, 2708–2716, 1975a.
- Ness, N. F., K. W. Behannon, R. P. Lepping, and Y. C. Whang, Magnetic field of mercury confirmed, *Nature*, *255*, 204 – 205, 1975b.
- Ogilvie, K., J. Scudder, V. Vasyliunas, R. Hartle, and G. Siscoe, Observations at the planet Mercury by the plasma electron experiment: Mariner 10, *J. Geophys. Res.*, *82*, 1807–1824, 1977.
- Potter, A., and T. Morgan, Evidence for magnetospheric effects on the sodium atmosphere of Mercury, *Science*, *248*, 835–838, 1990.
- Potter, A. E., Chemical sputtering could produce sodium vapor and ice on Mercury, *Geophys. Res. Lett.*, *22*, 3289–3292, 1995.
- Potter, A. E., and T. H. Morgan, Discovery of sodium in the atmosphere of Mercury, *Science*, *229*, 651–653, 1985.

- Potter, A. E., and T. H. Morgan, Potassium in the atmosphere of Mercury, *Icarus*, *67*, 336–340, 1986.
- Potter, A. E., and T. H. Morgan, Discovery of Sodium and Potassium Vapor in the Atmosphere of the Moon, *Science*, *241*, 675–680, 1988.
- Potter, A. E., and T. H. Morgan, Sodium and potassium atmospheres of Mercury, *Plan. Space Sci.*, *45*, 95–100, 1997a.
- Potter, A. E., and T. H. Morgan, Evidence for suprathreshold sodium on Mercury, *Adv. Space Res.*, *19*, 1571–1576, 1997b.
- Press, W. H., S. A. Teukolsky, W. T. Vetterling, and B. P. Flannery, *Numerical Recipes*, Cambridge Univ. Press, Oakleigh, 1992.
- Shemansky, D. E., Revised atmospheric species abundances at Mercury: The debacle of bad g values, *Lunar and Planet. Inst.*, p. 1, 1988.
- Shemansky, D. E., and T. H. Morgan, Source processes for the alkali metals in the atmosphere of Mercury, *Geophys. Res. Lett.*, *18*, 1659–1662, 1991.
- Simpson, J., J. Eraker, J. Lamport, and P. Walpole, Search by Mariner 10 for electrons and protons accelerated in association with Venus, *Science*, *183*, 1318–1321, 1974a.
- Simpson, J. A., J. H. Eraker, J. Lamport, and P. H. Walpole, Electrons and protons accelerated in Mercury's magnetic field, *Science*, *185*, 160–166, 1974b.
- Slavin, J. A., Mercury's magnetosphere, *Adv. Space Res.*, *33*, 1859–1874, 2004.
- Smyth, W. H., and M. L. Marconi, Theoretical overview and modeling of the sodium and potassium atmospheres of Mercury, *Astrophys. J.*, *441*, 839–864, 1995.
- Southwood, D. J., The magnetic field of Mercury, *Plan. Space Sci.*, *45*, 113–117, 1997.
- Sprague, A. L., A diffusion source for sodium and potassium in the atmospheres of Mercury and the Moon, *Icarus*, *84*, 93–105, 1990.
- Sprague, A. L., Mercury's atmospheric bright spots and potassium variations a possible cause, *J. Geophys. Res.*, *97*, 18, 257–18, 264, 1992a.

- Sprague, A. L., A correction to Mercury's atmospheric sodium bright spots and potassium variations: a possible cause, *J. Geophys. Res.*, *98*, 1231, 1992b.
- Sprague, A. L., R. W. H. Kozlowski, D. M. Hunten, and F. A. Grosse, An Upper Limit on Neutral Calcium in Mercury's Atmosphere, *Icarus*, *104*, 33–37, 1993.
- Sprague, A. L., D. M. Hunten, and K. Lodders, Sulfur at Mercury, Elemental at the Poles and Sulfides in the Regolith, *Icarus*, *118*, 211–215, 1995.
- Sprague, A. L., R. W. H. Kozlowski, D. M. Hunten, N. M. Schneider, D. L. Domingue, W. K. Wells, W. Schmitt, and U. Fink, Distribution and Abundance of Sodium in Mercury's Atmosphere, 1985–1988, *Icarus*, *129*, 506–527, 1997.
- Trávníček, P., P. Hellinger, and D. Schriver, Structure of Mercury's magnetosphere for different pressure of the solar wind: three dimensional hybrid simulations, *Geophys. Res. Lett.*, *34*, L05,104, 2007.
- Wiens, R. C., D. S. Burnett, W. F. Calaway, C. S. Hansen, K. R. Lykke, and M. J. Pellin, Sputtering Products of Sodium Sulfate: Implications for Io's Surface and for Sodium-Bearing Molecules in the Io Torus, *Icarus*, *128*, 386–397, 1997.
- Winske, D., and K. Quest, Magnetic field and density fluctuations at perpendicular supercritical collisionless shocks, *J. Geophys. Res.*, *93*, 9681–9693, 1988.
- Wurz, P., and L. G. Blomberg, Particle populations in Mercury's magnetosphere, *Plan. Space Sci.*, *49*, 1643–1653, 2001.
- Wurz, P., and H. Lammer, Monte-Carlo simulation of Mercury's exosphere, *Icarus*, *164*, 1–13, 2003.
- Yakshinskiy, B. V., and T. E. Madey, Photon-stimulated desorption as a substantial source of sodium in the lunar atmosphere, *Nature*, *400*, 642–644, 1999.
- Yakshinskiy, B. V., T. E. Madey, and V. N. Ageev, Thermal desorption of sodium atoms from thin SiO₂ films, *Surface Rev. Lett.*, *7*, 75–87, 2000.
- Yarnoz, D. G., R. Jehn, and M. Croon, Interplanetary navigation along the low-thrust trajectory of BepiColombo, *Acta Astronautica*, *59*, 284–293, 2006.